UNIVERSITÀ
DEGLI STUDI
FIRENZE

PhD in
Atomic and Molecular Photonics

CYCLE XXXIV

COORDINATOR
Prof. Diederik Wiersma

# Combining optical manipulation and FRET-based Molecular Tension Microscopy to study mechanotransduction in living cells

Academic Discipline (SSD) FIS/03


**Doctoral Candidate**
Dr.ssa Perego Laura

_____
*(signature)*

**Supervisor**
Dr. Capitanio Marco

_____
*(signature)*

**Coordinator**
Prof. Diederik Wiersma

_____
*(signature)*


Years 2018/2021

*"If we knew what it was we were doing, it would not be called research, would it?"*

*- Albert Einstein*

# Table of contents

**Table of contents** ..... **4**

**List of figures** ..... **8**

**List of relevant publications** ..... **10**

**Abstract** ..... **12**

**1 Introduction** ..... **18**

***1.1 Mechano-transduction*** ..... 20

*1.1.1 Focal adhesions and adherens junctions* ..... 21

*1.1.2 The LINC complex* ..... 23

*1.1.3 The actin cytoskeleton* ..... 25

***1.2 Application of forces on biological systems*** ..... 28

*1.2.1 Optical tweezers* ..... 28

1.2.1.1 Trapping mechanisms ..... 29

1.2.1.2 Dynamics of a trapped bead ..... 31

1.2.1.3 Thermal fluctuations of a trapped bead ..... 34

1.2.1.4 Measuring forces and displacements with optical tweezers ..... 36

*1.2.2 An indirect method: changing the substrate stiffness* ..... 38

***1.3 FRET (Forster Resonance Energy Transfer) MICROSCOPY*** ..... 40

*1.3.1 Fluorescence microscopy and advantages of fluorescent probes* ..... 40

1.3.1.1 Fluorescence and Stokes shift ..... 40

1.3.1.2 Spatial resolution ..... 42

1.3.1.3 Different fluorescent markers ..... 45
*1.3.2 FRET: a molecular ruler* ..... 48
*1.3.3 Methods to measure FRET efficiency* ..... 51
*1.3.4 FRET force sensors* ..... 52
1.3.4.1 Distance-based FRET sensors ..... 53
1.3.4.2 Orientation-based FRET sensors ..... 55
1.3.4.3 Insertion of FRET sensors into proteins ..... 56
**2 Setup implementation: combining optical manipulation and fluorescence microscopy ..... 58**
***2.1 Optical tweezers implementation*** ..... 62
*2.1.1 Optical trapping* ..... 62
*2.1.2 Calibration of the trap stiffness* ..... 65
*2.1.3 Cell membrane stimulation* ..... 66
***2.2 Fluorescence microscopy implementation*** ..... 68
*2.2.1 Excitation and detection of fluorescence* ..... 68
*2.2.2 Characterization of localization accuracy through FIONA* ..... 71
**3 Methods and procedures ..... 74**
***3.1 Scaling and cross-correlation of the acquired images*** ..... 76
***3.2 Calculation of FRET efficiency through the PixFRET plugin*** ..... 78
***3.3 FRET index calibration*** ..... 82
***3.4 Measuring tension on specific proteins with different FRET-force sensors*** ..... 84
*3.4.1 The actin sensor* ..... 84
*3.4.2 The alpha-actinin sensor* ..... 85
*3.4.3 The nesprin sensor* ..... 86
**4 Results ..... 88**
***4.1 Tension on actin and alpha-actinin increases with the stiffness of the substrate*** ..... 90
*4.1.1 Characterization of the actin-FRET sensor in cells adhered to a glass coverslip* ..... 90

*4.1.2 Actin tension in cells grown on hydrogels with different stiffnesses changes with substrate's rigidity* ..... 92

*4.1.3 Characterization of the alpha-actinin-FRET sensor in cells adhered to a glass coverslip* ..... 94

*4.1.4 Alpha-actinin tension in cells grown on hydrogels with different stiffnesses changes with substrates' rigidity* ..... 96

***4.2 The role of forces on the actin cytoskeleton during differentiation of hiPS cells into cardiomyocytes*** ..... 98

***4.3 The role of MLL4 protein in defining tension on nesprin in mesenchymal cells*** ..... 101

**5 Conclusions and future perspectives ..... 106**

***5.1 Construction and characterization of a novel setup for the investigation of mechanotransduction processes*** ..... 108

***5.2 The stiffness of the substrate determines tension on the cell's cytoskeleton*** ..... 109

***5.3 Mechanical tension plays a fundamental role in cell's differentiation and development*** ..... 110

***5.4 Chromatin compartmentation tunes mechanical tension at the nucleus-cytoskeleton interface*** ..... 111

**6 Appendixes ..... 114**

***6.1 Creation of a PDMS chamber for experiments on hydrogels*** ..... 116

***6.2 Preparation of samples and measurement parameters*** ..... 117

*6.2.1 HEK cell lines* ..... 117

*6.2.2 Human Induced Pluripotent Stem cells* ..... 119

*6.2.3 hiPSCs - derived cardiomyocytes* ..... 121

*6.2.4 Mesenchymal cells for measurement on nesprin* ..... 122

***6.3 FuGENE® transfection protocol for hiPSCs*** ..... 124

***6.4 FuGENE® transfection protocol for cardiomyocytes*** ..... 124

***6.5 FuGENE® transfection protocol for MSCs*** ..... 125

**7 References ..... 126**

**8 Acknowledgements ..... 136**

# List of figures

**Figure 1| Schematic of the experimental approach used in mechanotransduction experiments.** ....15
**Figure 1.1 | Scheme of molecular connectivity from the ECM to the nucleus**. ....20
**Figure 1.2|Schematic model of focal adhesion molecular architecture.** ....22
**Figure 1.3|Schematic model of adherens junction molecular architecture.** ....23
**Figure 1.4| Schematic model of the LINC complex molecular architecture.** ....24
**Figure 1.5|Actin different architecture regulates shape changes and cellular motility**. .25
**Figure 1.6| Force transduction by the actin cytoskeleton.** ....27
**Figure 1.7| Schematic of optical tweezers' trapping mechanisms.** ....30
**Figure 1.8|Dynamic of a trapped bead.** ....32
**Figure 1.9|Thermal fluctuations of a trapped bead.**. ....35
**Figure 1.10|Example of fitting of a power spectrum.** ....37
**Figure 1.11|Substrate's stiffness influences the extension of the cell and the assembly of the cytoskeleton.** ....38
**Figure 1.12|Typical stiffnesses of human tissues.**. ....39
**Figure 1.13|Jablonski's diagram.** ....41
**Figure 1.14| Franck-Condon Principle and Stokes Shift representations.** ....42
**Figure 1.15|Airy disk.** ....43
**Figure 1.16| The Rayleigh and Abbe diffraction limits and their definitions.** ....44
**Figure 1.17| Green Fluorescent Protein from Aequorea Victoria.** ....46
**Figure 1.18| GFP and RFP derivatives spectra.** ....46
**Figure 1.19|Quantum dots' emission spectra vary with their dimension.** ....48
**Figure 1.20|Illustration of FRET mechanisms.** ....49
**Figure 1.21| Distance-based FRET sensors.**. ....53
**Figure 1.22|HP35 distance-based FRET sensor and its calibration.** ....54
**Figure 1.23|Comparison between distance- and orientation-based FRET sensors.** ....55
**Figure 1.24| Overview of MTM constructs.** ....57
**Figure 2.1| Experimental setup combining optical tweezers and fluorescence microscopy.** ....60
**Figure 2.2|Schematic of the optical manipulation part of the experimental apparatus.** 63

**Figure 2.3| Linear fit of the optical power of the beam with respect to the diode current.** .....64
**Figure 2.4| Cell membrane manipulation experiment.**.....67
**Figure 2.5| Schematic of the fluorescence microscopy part of the experimental apparatus.** .....69
**Figure 2.6| Single molecule localization experiment to characterize the setup localization accuracy.**.....72
**Figure 3.1| Example of the final image obtained after complete algorithm operation.** .77
**Figure 3.2|Example of donor SBT modelling through the PixFRET plugin.** .....79
**Figure 3.3| Example of the resulting images after PixFRET plug-in processing.** .....81
**Figure 3.4| Characterization of FRET standards.** .....83
**Figure 3.5| The actin FRET sensor.** .....85
**Figure 3.7| The nesprin FRET sensor**.....86
**Figure 4.1| Example of a HEK cell transfected with the AcpA sensor.**.....91
**Figure 4.2|Comparison of FRET indexes of cpA and AcpA in HEK cells.** .....91
**Tab I** | FRET index values of actin sensors grown on substrates of different stiffness. .....93
**Figure 4.3| FRET index values of actin sensors grown on substrates of different stiffness.** .....93
**Figure 4.4|FRET in HEK cells transfected with alpha-actinin sensor.**.....95
**Table II |** FRET index values of actinin sensors grown on substrates of different stiffness. .....96
**Figure 4.5|FRET index values of alpha-actinin sensors grown on substrates of different stiffness.** .....97
**Figure 4.6| Protocol for Cardiac Maturation of Human Pluripotent Stem Cells on Nanopatterned Surfaces in Long-Term Cultures.** .....99
**Table III |** FRET index values of actin sensors in staminal hiPSC cells and in differentiated hiPSC-derived cardiomyocytes.....100
**Figure 4.7| FRET in hiPSCs and hiPSC-CMs transfected with the actin FRET sensor.** .....100
**Figure 4.8| Example of a fluorescence image of MSCs transfected with the nesprin FRET sensor.** .....102
**Table IV** | FRET index values of nesprin sensors in wild type (WT1) mesenchymal cells and in mutated (C6) mesenchymal cells. .....102
**Figure 4.9|FRET in WT1-MSCs and C6-MSCs transfected with the nesprin FRET sensor.** .....103
**Figure 6.1| PDMS chamber.**. .....116
**Figure 6.2|Imaging chamber schematics.** .....118
**Figure 6.3| hiPSC-derived cardiomyocytes.** .....120

# List of relevant publications

1. C. Arbore, L. Perego, M. Sergides, M. Capitanio (2019) *"Probing force in living cells with optical tweezers: from single-molecule mechanics to cell mechanotransduction"* Biophys Rev 11:5.

2. M. Sergides, L. Perego, T. Galgani, C. Arbore, F.S. Pavone, M. Capitanio *"Probing mechanotransduction in living cells by optical tweezers and FRET-based molecular force microscopy"* The European Physical Journal Plus 136.3 (2021): 1-19.

# *Abstract*

Cell's ability to respond and sense mechanical forces has a fundamental role in biological systems. Mechanotransduction, which is the conversion of mechanical forces into biochemical and biomolecular signals, is at the basis of many processes which are of great importance for cell's development and differentiation, for their correct behaviour and for the development of pathologies. However, a complete knowledge of the molecular mechanisms at the basis of mechanotransduction is still lacking [1]. *In vitro,* new developments in single-molecule force spectroscopy methods have provided important insights into how forces can influence enzymatic reactions and structural states of proteins and nucleic acids. There is also increasing evidence that the mechanical properties of the extracellular environment directly influence the mechanical properties of the cell and, in turn, trigger signalling pathways and tune gene expression. The complexity of these mechanisms makes the study of mechanotransduction impossible to tackle with a single experimental technique. Optical tweezers, magnetic tweezers and atomic force microscopes have been used to measure forces on the external part of the cellular membrane, since it is very difficult to use these approaches within the cell, due to the complexity of cellular systems and to the small accessibility of the intracellular structures [2].

My Ph.D. project aimed at the development and combination of advanced experimental approaches and techniques to investigate how mechanical signals are sensed by cells, how they propagate inside the cell, from the external membrane to the cell's cytoskeleton, and how they eventually translate into changes in biochemical signalling and gene expression. To this end, I designed and implemented an optical setup which combines optical tools to manipulate single cells with microscopy techniques to measure the propagation of mechanical and biochemical signals inside them.

I implemented through optical tweezers, which are made of a laser beam focussed by the microscope objective. Gradient forces acting near the focus of the beam are able to attract and stably trap particles with micrometric dimensions, which can in turn be used as handles to manipulate single molecules or cells. Moreover, optical tweezers, allow the direct measurement of forces, which can be applied both from the outer plasma membrane and inside the cell.

Nowadays, direct measurement of forces on distinct proteins inside cells in the piconewton range has been made possible also by using genetically encoded molecular tension sensors [3]. This technique, known as Molecular Tension Microscopy, is based on the use of elastic peptides, which are inserted between pairs of fluorescent proteins which undergo efficient FRET (Fluorescence Resonance Energy Transfer)[4]. Since FRET is highly dependent on distance and orientation

between fluorophores, we can measure forces by quantifying FRET efficiency. The insertion of a sensor module of this kind into the protein of interest, and the subsequent expression of this construct into cells, will then allow the analysis of molecular forces inside living cells.

In my thesis, in combination with optical tweezers, I implemented FRET microscopy and I applied it to the study of the propagation of mechanical forces into proteins that have a key role in mechanotransduction. This was made by using FRET-force sensors inserted into actin, alpha-actinin and nesprin. The investigation was focussed on three important aspects of mechanotransduction: the influence of the external environment on the transmission of forces in the actin cytoskeleton of cells, the role of tension sensed by the actin cytoskeleton during the differentiation of cells and, finally, the contribute of mechanical force on chromatin compartmentation in the cell nucleus.

The combination of optical manipulation, fluorescence, and FRET force microscopy (Fig. 1) is a powerful tool that will open the way to the study of the propagation of mechanical and mechanotransduction signals in living cells and has the potential to reveal new biophysical mechanisms in mechanobiology.

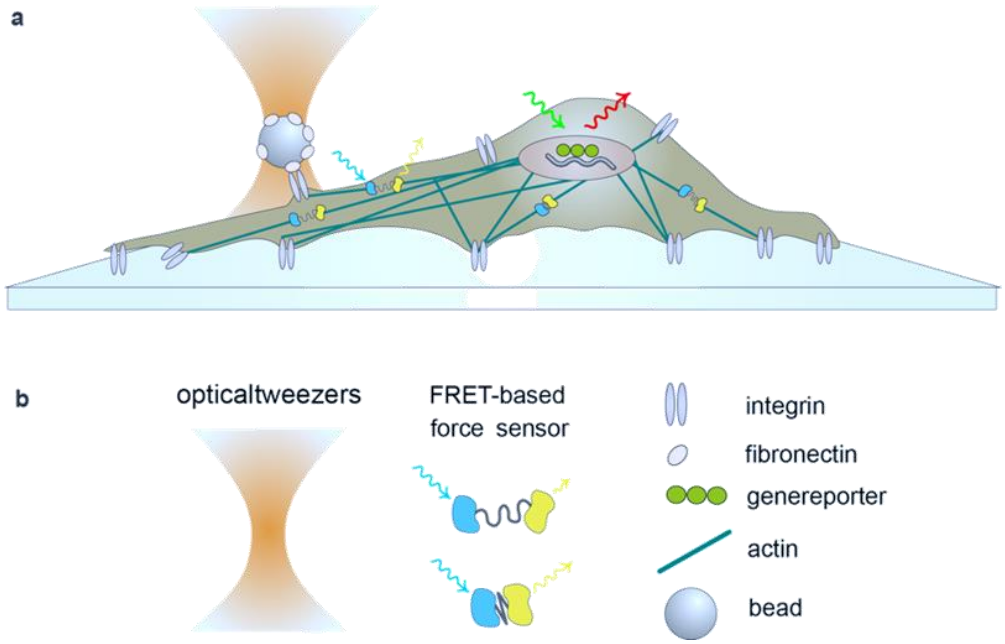


***Figure 1| Schematic of the experimental approach used in mechanotransduction experiments. (a)*** *Optical tweezers are used to apply and measure mechanical load on specific adhesion molecules on the cell plasma membrane. Genetically encoded FRET-based force sensors measure the propagation of mechanical signals in the cell. Fluorescent gene reporters detect mechanically induced changes in gene expression.* ***(b)*** *The various components in detail used in a mechanotransduction experiment. Image retrieved by* [5].

More in detail, this thesis is structured as follows:

- Chapter 1 is dedicated to the introduction of the background and state-of-the-art. First of all, a brief introduction about mechanotransduction is required to frame the biological issue. Different parts of the cell where mechanotransduction acts are considered in a more detailed way: focal adhesions and adherens junctions, the actin cytoskeleton and, finally, the LINC complex and the nuclear membrane. After that, different methods to apply mechanical forces on cells are investigated. A brief description of how optical tweezers work and the theory at the basis of optical trapping are given. Furthermore, the method of changing the substrate's stiffness to study the influence of the external environment on the mechanical properties and the forces sensed by the cytoskeleton of cells is examined. Finally, the last part of chapter one is dedicated to fluorescence microscopy and FRET (Fluorescence Resonance Energy Transfer). Here, a short review of how FRET efficiency can be measured and on the structure and function of FRET sensors are given.
- Chapter 2 deals with the description of the setup that I implemented during my Ph.D., which combines optical manipulation and FRET fluorescence microscopy. First, a detailed scheme of the optical tweezers implementation is presented, where the mechanism of trapping is shown. Then, the procedure for trap stiffness calibration is illustrated in detail. Finally, a proof-of-principle experiment for the measurement of cell membrane stiffness is described. The second part of chapter 2 is dedicated to the implementation of fluorescence FRET microscopy and the description of the parts of the setup enabling fluorescence excitation and two-colour imaging for FRET detection. Finally, characterization of the localization accuracy of the single chromophores through the FIONA algorithm is described in detail.
- Chapter 3 is dedicated to methods and procedures. In the first part, methods for post-processing and analysis of the acquired images are illustrated. After that, the experiments through which we performed FRET efficiency calibration are shown. Finally, the different kind of FRET sensors for specific proteins (actin, alpha-actinin, and nesprin) that we used are illustrated.
- In chapter 4 the results are shown. Results are divided accordingly to the aspect of mechanotransduction investigated: first, results obtained from experiments on the influence of external environment on forces sensed by the actin cytoskeleton, and in particular by F-actin and alpha-actinin, of HEK293 cells adhered both to glass coverslips and different stiffness hydrogels are shown. After that, the results concerning the investigation of the role of mechanical forces on actin cytoskeleton during differentiation performed on

human induced pluripotent stem cells and on hiPSC-derived cardiomyocytes are illustrated. Finally, the last part of chapter 4 shows the results obtained from investigation of the role of chromatin compartmentation on the mechanical forces sensed by the nuclear membrane, which were probed through the use of a sensor for nesprin, which is a protein located at the nuclear membrane, transfected and stably expressed into wild type and mutant mesenchymal cells.

- Chapter 5 is dedicated to scientific discussion and conclusions on the results obtained from experiments, as well as future perspectives.
- In chapter 6 I give a detailed description of technical procedures, showing both technical tools and biological protocols for handling of samples and transfection of FRET sensors into cells, as well as information on the experimental parameters used in experiments.

# 1 Introduction

## 1.1 Mechano-transduction

In the last decade the study of mechanical regulation of biological systems has earned growing interest and substantial evidence indicate that the mechanical properties of the external environment directly influence the mechanical properties of the cell and can in turn activate different signalling pathways [5].

Mechano-sensors are proteins or macromolecular complexes that can translate mechanical inputs into biochemical outputs. Sub-cellular structures that mediate cell-cell and cell-matrix adhesion act as mechano-sensors for the cell by sensing the physical properties of the extracellular environment. These structures have different shapes, dimensions, and dynamics, reflecting the fact that cells need to adapt and respond to the variability of the extracellular environment [1]. Although the proteins involved in adhesions complexes show very different structures and functions, a common feature relies on the fact that they all exhibit a dynamic interaction of the cytoplasmic domain with the actin cytoskeleton, thus allowing the cell to adapt to changes in the surrounding environment [6]

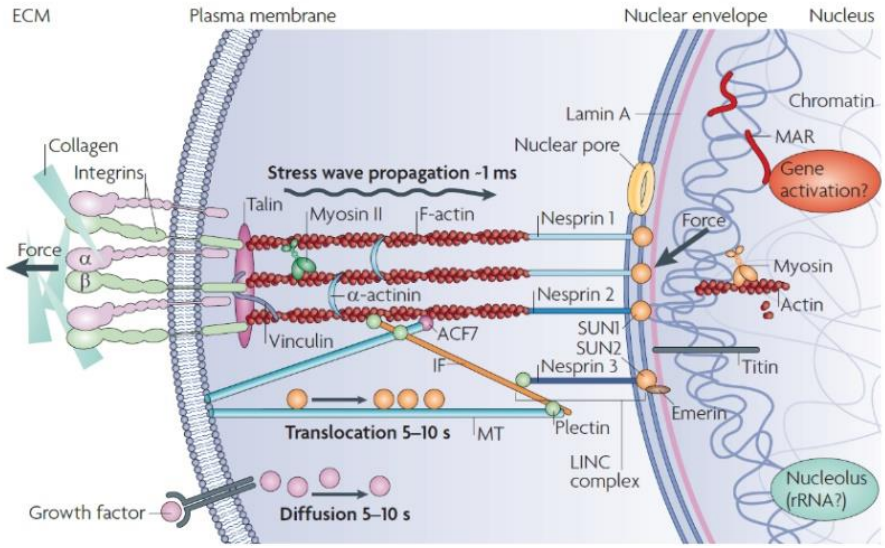


***Figure 1.1 | Scheme of molecular connectivity from the ECM to the nucleus***. *In the extracellular environment, a force is applied to integrins through the extracellular matrix and is then transmitted to the actomyosin cytoskeleton by focal adhesions. The signal is conveyed through all the cytoplasm and reaches nesprins, which connect F-actin to the inner nuclear membrane and to SUN proteins. These proteins connect to the lamins forming the nuclear scaffold, which attaches to DNA and chromatin. The force which has been transmitted from the extracellular matrix and conveyed by all these proteins along the whole cell can therefore directly affect gene positioning and activation. Image retrieved by [1]*

Mechano-sensors are not only present at the interface with the external part of the cell: for example, the LINC (Linker of Nucleoskeleton and Cytoskeleton) complex, which is located at the nuclear membrane level and consists of a chain of specific proteins, mechanically couples the nucleus to the rest of the cell [7].

### *1.1.1 Focal adhesions and adherens junctions*

Focal adhesions are the adhesion structures responsible for mechanical linkage between cells and the extracellular matrix (ECM) and their role in mechanotransduction is well characterized [8]. Focal adhesions are large and dynamic macromolecular assemblies which are involved in a great variety of cellular processes, such as development, differentiation and motility of the cell [9].

Integrins represent the key family of proteins of focal adhesions as they function as a bridge between the extracellular and the intracellular environment and participate to a great number of intracellular events. Integrins transmit signals through the ECM in both directions: by binding to ligands, they transmit signals into the cell and mediate re-organization of the cytoskeleton, gene expression and differentiation of the cell; on the other hand, signals coming from the intracellular environment can propagate through integrins and regulate cellular adhesion [10]. When an integrin receptor binds to its ECM ligand, its signalling domain is activated, and intracellular proteins are recruited. These proteins assemble around the activated cytoplasmic domain and form the molecular clutch (Fig. 1.2) , a molecular bridge that connects integrin receptors with actin filaments in the cell cytoplasm [11]. A great number of proteins are involved into this bridge, among which talin, vinculin, paxillin and α-actinin play a critical role.

In cell-cell adhesions, the structures analogous to focal adhesions are adherens junctions. In this case, the most relevant role in mechanotransduction is played by another super-family of proteins: cadherins. These are calcium-dependent proteins: they contain three binding sites for calcium ions and, when calcium is not present, they collapse into a compact structure which does not allow interactions [12]. Typically, each tissue expresses one family member of cadherins (i.e., E-cadherin or P-cadherin for epithelial tissue, VE-cadherin for endothelial tissue, and N-cadherin for all other non-epithelial cells), which has the role of linking the intercellular junction to the actin filaments. The cadherin intercellular junctions have different characteristics according to the family they belong, and these differences are reflected

in the structural organization of the adherens junctions and the associated F-actin, leading to different mechanical and mechanotransduction properties [13].

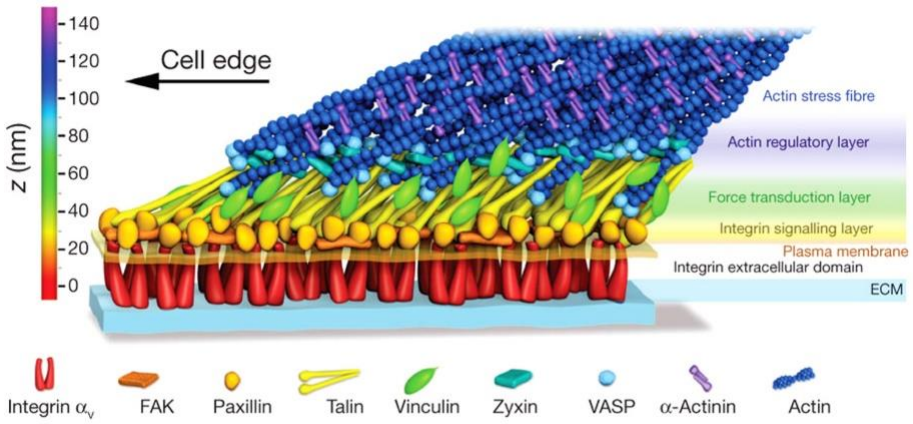


***Figure 1.2|Schematic model of focal adhesion molecular architecture.*** *Figure shows the three layers of focal adhesions: the integrin signalling layer (where signalling cascades that control adhesion dynamics happen), the force transduction layer (where diagonally arranged proteins make a direct connection between integrins and F-actin), and the actin regulatory layer, which connects to actin stress fibres. Image retrieved from* [11].

Despite the variety, all classical cadherins present a highly conserved cytoplasmic domain which functions as a binding site for catenins, cytoplasmic proteins anchoring classical cadherins to the underlying cytoskeleton [14]. The cytoplasmic domain is associated to β-catenin, which in turn binds to α-catenin. The latter interacts with the actin cytoskeleton with a bond that can be further reinforced through other proteins, as for example vinculin [15]. Cadherins can also be found in desmosomes, which are adhesion structures commonly found in mechanical stressed tissues (i.e., cardiac muscle, epithelium). In this case, cadherins structure differs significantly from the one found in adherens junctions, and for this reason they are identified with different names: desmoglein and desmocollin. In the cytoplasm, these proteins directly link to the intermediate filaments [13].

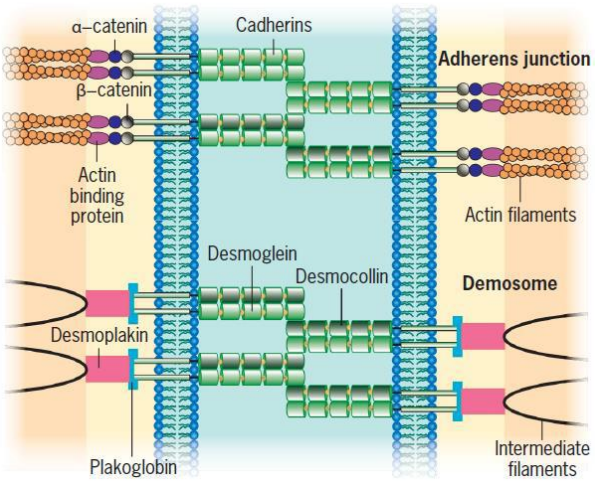


***Figure 1.3|Schematic model of adherens junction molecular architecture.*** *The key protein in adherens junctions is cadherin. Cadherin dimers of two different cells associate in the extracellular space. The cytoplasmic domain of cadherin connects to the actin cytoskeleton through different intermediate proteins, such as catenin. Desmosomes are structures similar to adherens junctions, but they are constituted by cadherin's isoforms (desmoglein and desmocollin), which directly bind to intermediate filaments. Image retrieved from* [16].

### *1.1.2 The LINC complex*

The LINC (Linker of Nucleoskeleton and Cytoskeleton) complex is a molecular bridge connecting the cellular nucleoskeleton and cytoskeleton. It wraps the nuclear membrane and bidirectionally transmits signals and information between nuclear and cytoplasmic environments [17] (Fig. 1.4). When a mechanical stress is applied to the cell membrane a consequent alteration of the nuclear morphology is observed, underlying the fact that mechanical stress can be transmitted from the ECM up to the nucleus [18].

The nuclear membrane is composed by a double-lipid system: an inner (INM) and an outer membrane (ONM), separated by the perinuclear space (PNS), which presents nuclear pores through which bilateral transport of macromolecules occurs. The ONM is contiguous with the endoplasmic reticulum, while the INM is connected to a network of filamentous proteins collectively known as nuclear lamina and composed of A-type and B-type lamins. Nuclear lamins have a key role in maintaining the nuclear structure, regulating gene expression, and organizing chromatin and it is part of the LINC complex by linking to the cytoskeleton through the INM and ONM

proteins [19]. The LINC complex is made of two protein domains: the SUN (Sad1 and UNC-84) domain and the KASH (Klarsicht, ANC-1, and Syne Homology) domain. KASH proteins are expressed in proteins known as nesprins and are localized in the PNS from which they extend into the cytoplasm, allowing the LINC complex to bind to different cytoskeletal elements; on the other hand, SUN proteins are localized in the INM and anchor the LINC complex to the nuclear lamina and other chromatin-binding proteins [20]. The nuclear envelope proteins interact with a variety of transcription factors that control critical signalling pathways involved in mechanotransduction signalling [7].

The LINC complex is implicated in different aspects of cellular organization and function. One of the most important functions of LINC is the control of orientation and shape of the nucleus: nesprins, which are the most important proteins of the KASH domain, can sense myosin-dependent cellular tension and alter the nuclear shape [21]. Another important function of the LINC complex as a mechanosensor is the potential to affect functions of centrosomes [22] and chromosomes [23] to regulate cell division and replication. It has also been observed that LINC proteins may play a regulatory role in the repair of DNA damage [24], [25]. Moreover, the physical interconnection between the LINC complex and nuclear chromatin may act as a key mediator for cellular differentiation [26]. Finally, LINC complex has also been associated with nucleus shape and movement during cell migration, and its disfunctions have been related with a range of diseases [27].

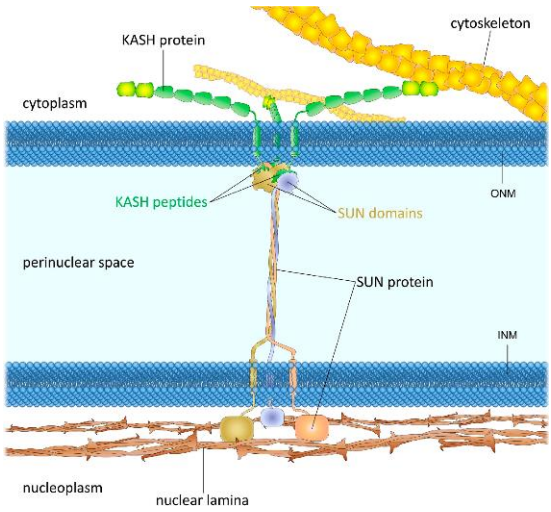


***Figure 1.4| Schematic model of the LINC complex molecular architecture.*** *The LINC complex is composed of KASH proteins in the ONM and SUN proteins in the INM. The cytoplasmic extensions of KASH proteins interact with different cytoskeletal elements. The nucleoplasmic domains of SUN proteins anchor the LINC complex to the nucleoskeleton through the interactions with the nuclear lamina and other chromosome-binding proteins. Image retrieved from* [20].

### *1.1.3 The actin cytoskeleton*

As mentioned above, force transmission through the actin cytoskeleton plays a central role in many aspects of cell life, and the starting point for mechanotransduction processes is at the interface with the extracellular matrix or surrounding cells. As the mechanical characteristics of the extracellular environment change, the actin cytoskeleton can organize in a great variety of structural architectures that corresponds to specific methods of transduction of mechanical forces into biochemical signals. Therefore, the actin cytoskeleton actively responds to mechanical stimuli through a structural reorganization. The architectural versatility of the cytoskeleton can be explained by considering the great abundance of proteins which can associate to actin filaments, and the corresponding signalling pathways they create. This can lead to think at the actin filaments as passive elements which connect mechanosensitive binding proteins, however it has been proposed that actin filaments are mechano-sensors themselves [28].

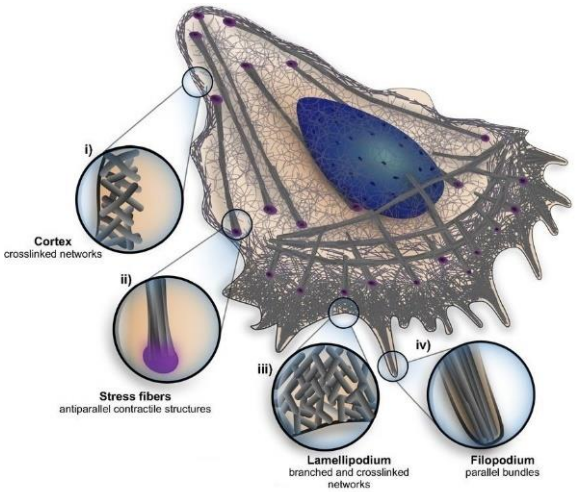


***Figure 1.5 | Actin different architecture regulates shape changes and cellular motility.*** *(i) A subtle layer of actin, called cortex, covers the plasma membrane in the rear and lateral regions of the cell, allowing changes and maintenance of cellular shape; (ii) The whole cell contains a network of crosslinked filaments intermixed with contractile bundles. The network includes stress fibres which connects the cytoskeleton to the ECM through adhesion sites; (iii) At the front of the cell lamellipodium are made up by branched and cross-linked networks which have a key role in cell movement since they push the cellular membrane by polymerizing against it; (iv) At the front of the cell there are finger-like structures known as filipodia, which are important for directional response of the cell. Image retrieved from* [29].

Recent advances suggest that different actin structures are used for different mechanical functions, proving that they can sense and respond to different mechanical stimuli. Insights into the architecture of polymerized actin filaments mostly come from electron microscopy data, showing a structure of double-stranded right-handed helices filaments, with an average pitch of 36 nm [30]. These filaments assemble into higher-order structures (Fig. 1.5), including dendritic networks, bundles, and meshes [29].

There is a clear relationship between actin architecture and mechanical loading of filaments, thus leading to a specific mechanical role in cell physiology. Different studies have been conducted on how the actin cytoskeleton senses and responds to mechanical stress, leading to the hypothesis that the cytoskeleton can act as a mechanosensor in three main different ways [28] (Fig. 1.6). One possibility is that the actin filament structure can be modified by a mechanical load that directly alters the affinity with certain binding proteins (Fig. 1.6, (I)). It has been observed that when the tension increases, the actin filament stiffens due to an increasing affinity with myosin II and a correspondent decrease of affinity with cofilin [28], [31], [32]. A second way through which actin can respond to tensions is by a conformational change of Actin-Binding Proteins (ABPs), which usually link one hand of the cytoskeleton to a cellular membrane. Mechanical force induces unfolding of the actin-binding protein, thus giving access to previously hidden binding sites for other proteins (Fig. 1.6, (II)). An example of this mechanism has been shown for talin, which is associated to focal adhesions, and vinculin, which is an actin binding protein. It has been suggested that force induced by actomyosin contraction could cause talin unfolding and exposure of a previously buried vinculin binding domain, thus strengthening the link between focal adhesions and the actin cytoskeleton [33]. The last mechanism of transduction (Fig. 1.6, iii) is given by the fact that mechanical forces can directly influence actin polymerization kinetics and that actin polymerization occurring against an obstacle can affect architectural properties of the network structure (i.e., when growth is opposed by high forces, polymerization can stall) [28].

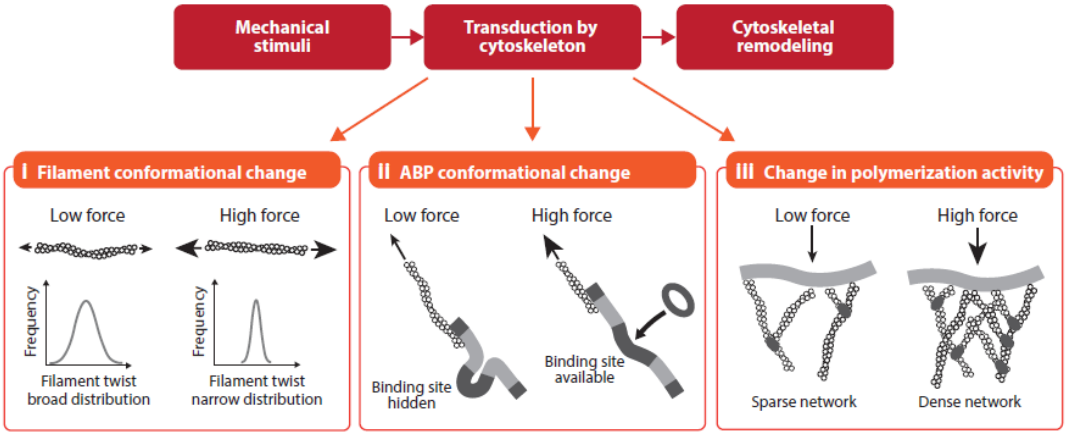


***Figure 1.6| Force transduction by the actin cytoskeleton.*** *(i) Actin filaments can directly be sensitive to mechanical stress, changing conformational state under direct tension; (ii) Actin-binding proteins can change conformation under tension, opening previously hidden binding sites for other proteins; (iii) The polymerization kinetics of actin-binding proteins can be altered by mechanical load, thus changing the network density. Image retrieved from* [28].

## 1.2 Application of forces on biological systems

Cell's ability to respond to mechanical forces plays a fundamental role in the development, differentiation, and correct functionality of biological systems. However, molecular mechanisms underlying mechanotransduction are unclear, owing to the lack of appropriate techniques to measure molecular tensions at the molecular level inside living cells and to the complexity of intracellular structures.

*In vitro,* the development of single-molecule force spectroscopy methods has allowed the study of how forces might influence enzymatic reactions and structural states of proteins and nucleic acids. Optical tweezers (OT) have been used to study how molecular motors produce mechanical forces or to determine conformational changes induced by tension in specific proteins [34]–[36]. Atomic force microscopy (AFM) has allowed the study of the unfolding mechanics of proteins, as well as the quantification of adhesion forces both *in vitro* and *in vivo* [37]. Magnetic tweezers (MT) have been used to evaluate the rigidity and the torque of DNA [38]. As mentioned above, the use of these techniques inside living cells is extremely difficult owing to the complexity and restricted accessibility of intramolecular structures. For this reason, these methods have been used mostly in a non-specific manner and for measurements on the external part of the cellular membrane. One promising way to use these methods is in combination with the imaging of genetically-encoded FRET (Fluorescence Resonance Energy Transfer)- force sensors [5], as we discuss to a greater extent below.

### 1.2.1 Optical tweezers

The very first application of optical tweezers was live cell manipulation [39], [40]. After that, force measurements in live cells developed slower than in vitro since the application in vivo was made difficult by the complexity of cell environment. Optical tweezers are now considered as a powerful tool for quantifying molecular forces in vivo: if compared to other techniques as AFM and magnetic tweezers, optical tweezers are characterized by higher position and force resolution that allow measurements of movements on the Angstrom scale and of pN and sub-pN forces, which make them an ideal choice in several applications [2], [34].

#### *1.2.1.1 Trapping mechanisms*

Optical tweezers are easily implemented in an optical microscope by focusing a laser beam through the microscope objective to create a large gradient of light intensity. Forces in optical tweezers are generated by the interaction of the laser light with the trapped dielectric microsphere. Scattering of the laser light by the dielectric particle alters the photon flux and the momentum carried by the light. For the momentum conservation principle, an equal and opposite momentum change is imparted to the particle. Analytical expressions for the forces that arise from this interaction can be obtained in two extreme cases: the Rayleigh regime, when the particle dimension is much smaller than the wavelength of the laser beam, and the ray optics regime, when the beam wavelength is much smaller than the bead dimension [41].

Optical tweezers were thought to act at the level of atomic systems, therefore in the Rayleigh regime. In this case, the microsphere behaves as a simple point dipole [42] and the total force acting on the trapped bead can be decomposed in two different components: the scattering force $\overrightarrow{F_s}$ and the gradient force $\overrightarrow{F_g}$ (Fig 1.7, (d)). The scattering force is in the direction of propagation of the incident light and is directly proportional to its intensity. The second force is a gradient force, which arises from the interaction between the inhomogeneous electric field and the dipole, and it is proportional to light intensity as well. Different works [42], [43] describe the Rayleigh regime, and it is known that the two forces are described by the following equations [44]:

$$\overrightarrow{F_s} = \sigma_s \frac{m}{c} I(\vec{r})\hat{z} = \frac{8}{3}\pi \left(\frac{2\pi}{\lambda} R\right)^4 R^2 \frac{(n_r^2 - 1)^2}{(n_r^2 + 2)^2} \frac{m}{c} I(\vec{r})\hat{z} \tag{1.1}$$

$$\langle \vec{F}_g \rangle_T = \langle \left[\vec{d}(\vec{r}, t) \cdot \vec{\nabla}\right] \vec{E}(\vec{r}, t) \rangle_T = \langle 4\pi\varepsilon_0 m^2 R^3 \frac{(n_r^2 - 1)^2}{(n_r^2 + 2)^2} I(\vec{r}) \rangle_T \tag{1.2}$$

where $R$ is the microsphere radius, $c$ is the speed of light, $\varepsilon_0$ is the dielectric constant of vacuum, $\vec{E}(\vec{r}, t)$ is the electric field, $\sigma_s$ is the scattering cross section, and $n_r = n/m$ is the relative refraction index of the particle $(n)$ with respect to the surrounding medium $(m)$. The relationship between the laser beam intensity and the radiation field is described through the equation:

$$I(\vec{r}) = \frac{1}{2} \varepsilon \langle E^2(\vec{r}, t) \rangle_T \tag{1.3}$$

Therefore, whereas the scattering force is directed along the laser propagation axis $\hat{z}$, the radiation intensity gradient points towards the focus of the trapping laser beam, setting the force direction in this way. At any point in space where the gradient force is higher than the scattering force the bead is stably trapped. Since the gradient force is generally higher in the radial direction rather than in the direction of propagation of the laser, the trap usually applies stronger forces in the radial direction, that is the focal plane of the objective. On the other hand, along the propagation axis, if the bead is at equilibrium, it means that the scattering force is balanced by the longitudinal component of the gradient force: in a microscope, this is translated in the fact that the trapping area is localized near the objective focus but is lightly displaced toward the positive direction of $\hat{z}$ due to radiation pressure (Fig. 1.7b and 1.7c).

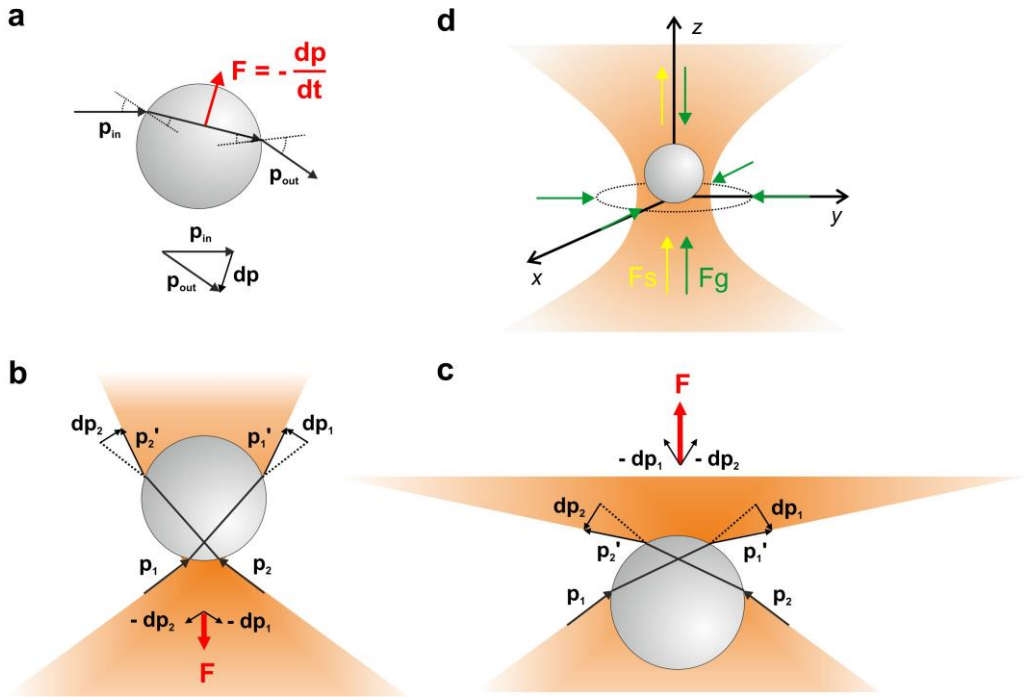


***Figure 1.7| Schematic of optical tweezers' trapping mechanisms. (a)*** *A single light ray is two-times reflected while passing through a dielectric sphere.* $\overrightarrow{p_{in}}$ *and* $\overrightarrow{p_{out}}$ *represents the incoming and outcoming momentum, respectively, whereas* $\overrightarrow{dp} = (\overrightarrow{p_{out}} - \overrightarrow{p_{in}})$. $\vec{F}$ *is the resulting optical force applied to the bead.* ***(b), (c)*** *The trapping laser beam is refracted by a trapped dielectric microsphere that is located above (b) or below (c) the beam focus. The two light rays are symmetric with respect to the beam axis and for each ray the refracted ray and the change in momentum are depicted. The optical force, represented in red, pushes the bead towards the beam focus, whatever the position of the bead with respect to the laser beam.* ***(d)*** *The gradient force (green) is directed towards the beam focus, whereas the scattering force (yellow) points towards the direction of laser propagation. Image retrieved from* [41].

The trapping mechanisms can be easily understood in the ray optics regime. In this approximation, the laser beam can be decomposed into light rays propagating in straight lines. A light ray can be thought as made by a photon flux which carries momentum parallel to the ray direction and which is refracted when it passes through mediums characterized by different refractive indexes, following Snell's law. Figure 1.7a shows what happens when a single light ray is refracted by a microsphere with refractive index higher than the surrounding medium. The change in momentum and the resulting force are also shown.

The focussed beam can be split in rays pairs (Fig. 1.7b, 1.7c), each one having appropriate intensity and direction. For each pair, the change in momentum and the optical force arising from refraction can be drawn. Whatever the position of the microsphere with respect to the laser beam, the gradient force points towards the beam focus. This qualitative scheme shows how stable 3D-trapping of a dielectric microsphere is established [41].

#### *1.2.1.2 Dynamics of a trapped bead*

One common characteristic of all trapping regimes described above is that, for small distances, the trap behaves as an ideal spring, thus following Hooke's law. It is therefore possible to characterize the optical trap through an elastic constant $k$, named "trap stiffness". The trap stiffness is constant in the radial plane, and it is smaller in the axial direction, where the intensity gradient is smaller [45]. The stiffness of optical tweezers depends on several factors such as the laser power, the numerical aperture of the objective, the dimension of the bead, and the refractive index of both the microsphere and the surrounding medium.

Understanding the bead dynamics is fundamental to understand the experiments on living cells, to measure the amplitude and dynamics of proteins' conformational changes, to optimize spatial and temporal resolution, and to calibrate the trap stiffness. Here we focus on the simple case of one bead moving in one direction on the radial plane [41]. As shown in figure 1.8, the bead is modelled as a pointlike mass which is subjected to an external force imposed by the optical tweezers. The force is represented as a spring, characterized by an elastic constant $k$ moving in the viscous buffer surrounding the microsphere. The elastic force is described through Hooke's law, where the force is proportional to the spring extension:

$$\vec{F}_{trap} = -k\vec{x} \tag{1.4}$$

where $\vec{x}$ is the radial distance, which is perpendicular with respect to the propagation direction of the laser beam, and $k$ is the trap stiffness. $\vec{F}_{trap}$ always points towards the centre of the trap.

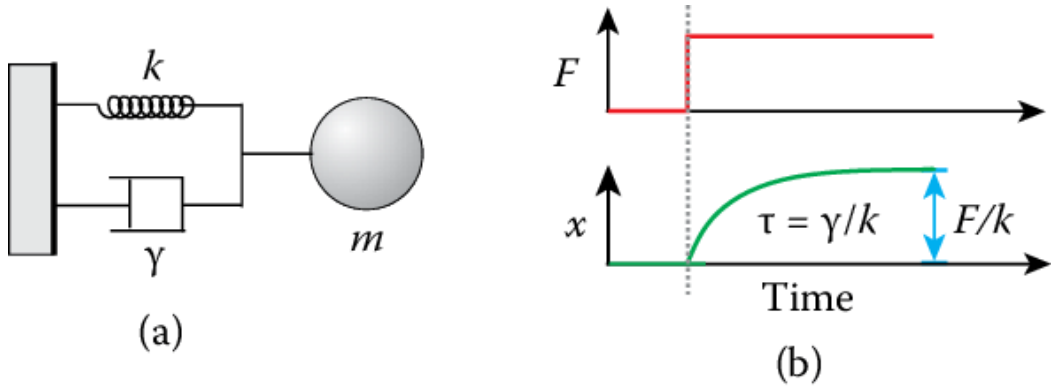


***Figure 1.8|Dynamic of a trapped bead. (a)*** *Dynamic model of a bead of mass m which is trapped through optical tweezers characterized by a trap stiffness k, and surrounded by a medium with a viscous drag coefficient γ.* ***(b)*** *Dynamic of the bead after the application of a force F: the bead moves exponentially from the zero position to the equilibrium one, which is given by* $x = F/k$*, with a characteristic time constant given by* $\tau = \gamma/k$*. Image retrieved from* [41].

The elastic force is not the only force acting on the bead: viscous friction acts on the bead owing to the presence of the immersion medium, which is characterized by the viscous drag coefficient γ. The bead is also subjected to an inertial force ($m \cdot a$), but this force is always negligible compared to the viscous force. The ratio between the inertial and the viscous force is named Reynold's number (Re). When dealing with small objects such as microbeads, cells, or proteins in aqueous solutions, Re is always less than unity. If $Re << 1$, the object of interest is subjected to a force which is directly proportional to its velocity, following Stokes' law [46]:

$$\vec{F}_{drag} = -\gamma\vec{v} \tag{1.5}$$

where the viscous drag coefficient $\gamma$ for a sphere of radius R immersed in a buffer of viscosity η is:

$$\gamma = 6\pi\eta R \tag{1.6}$$

The equation of motion for the bead in the $\vec{x}$ direction can be obtained by applying Newton's second equation:

$$\gamma \frac{\delta \vec{x}}{\delta t} + k\vec{x} = \vec{F} \tag{1.7}$$

where $\vec{F}$ is a generic external constant force that is applied to the microsphere, and the inertial term $m \cdot \delta^2 \vec{x}/\delta t^2$ is neglected due to the low Reynolds' number approximation. If we consider that a perturbation starts at a time $t = 0$, that is the time at which the bead is located at equilibrium in the centre of the trap ($x(0) = 0$), from eq. 1.7 we can write that the microsphere starts to move with a velocity given by:

$$\frac{\delta \vec{x}}{\delta t} = \frac{\vec{F}}{\gamma} \tag{1.8}$$

Thus, the spring extends in the direction of the force and produces a growing opposite force which slows down the bead, until the external force is equal to the elastic force of the trap, which corresponds to the condition given by:

$$\vec{F} = k\vec{x} \tag{1.9}$$

The evolution of motion over time is represented in Fig. 1.8b, described by the solution of the equation of motion:

$$|\vec{x}(t)| = \frac{|\vec{F}|}{k}\left[1 - \exp\left(-{}^{t}/_{\tau}\right)\right] \tag{1.10}$$

where $\tau = \gamma/k$ is the system relaxation time and describes the time that the bead takes to reach the new equilibrium position, thus establishing a temporal resolution limit for the optical tweezers. Therefore, it is not possible to reveal movements faster than the relaxation time. It is important to consider that the relaxation time can notably change when the microsphere is bound to a cell or to the coverslip's surface through a protein, since the system stiffness increases [41].

### *1.2.1.3 Thermal fluctuations of a trapped bead*

In the previous section we analysed the case of a bead subjected to an external force in a viscous medium, but we did not consider that thermal forces considerably influence the motion of micrometric beads in aqueous solutions at room temperature. We now examine the case of a bead subjected to thermal forces only. In this case, the force $\vec{F}$, which was a constant external force in the previous paragraph, now indicates a random force which arises from collisions between water molecules and the trapped microsphere. Owing to the stochastic nature of the motion arising from collisions, the bead position can only be studied in statistical terms, thus by measuring the probability $p(x)$ of finding the bead in position $x$, or by calculating mean values as the mean position $\langle x \rangle$ or the mean quadratic position $\langle x^2 \rangle$. The trapped bead randomly oscillates around the initial equilibrium position $x(0) = 0$, so that $\langle x \rangle = 0$. In this case, considering the definition of variance ($\sigma_x^2 = \langle x^2 \rangle - \langle x \rangle^2$), we have that $\langle x^2 \rangle = \sigma_x^2$. This parameter quantifies how much the trapped bead moves due to thermal forces, or how high the thermal noise is in the position measurements of the bead. For an object affected by a harmonic potential $\left(U(x) = \frac{1}{2}kx^2\right)$, the equipartition theorem holds, and we have:

$$\frac{1}{2}k_B T = \frac{1}{2}k\langle x^2 \rangle \tag{1.11}$$

and thus:

$$\langle x^2 \rangle = \sigma_x^2 = \frac{k_B T}{k} \tag{1.12}$$

where $k_B$ is the Boltzmann's constant and $T$ is the absolute temperature. Equation 1.12 shows that the thermal fluctuations of the bead increase with temperature and decrease with the trap stiffness (Fig.1.9 (a)).

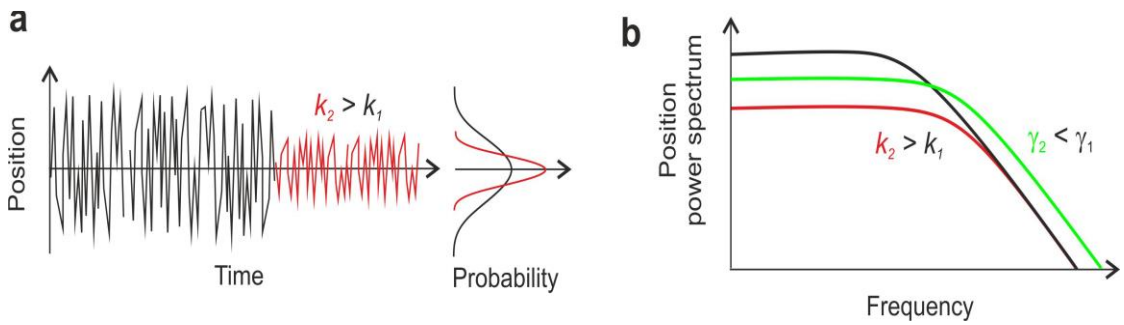


***Figure 1.9|Thermal fluctuations of a trapped bead. (a)*** *Position fluctuations of a trapped bead owing to thermal noise. The amplitude of fluctuations depends on trap stiffness (Eq. 1.12). Position thermal noise is distributed as a Gaussian (Eq. 1.13).* ***(b)*** *Frequency distribution of position noise is represented in a log-log plot. From Eq. 1.14, position fluctuations decrease with stiffness at low frequency, but not at high frequency (red and black lines). Position fluctuations also decrease with the drag coefficient γ for low frequency but, on the other hand, they increase for lower values of γ at high frequency (green and black lines). Image retrieved by* [41].

At thermal equilibrium it is possible to describe the probability to find the bead in a certain position through the following equation [47]:

$$p(x) = \frac{1}{Z} exp\left[-\frac{U(x)}{k_B T}\right] = \frac{1}{Z} exp\left[-\frac{x^2}{2\sigma_x^2}\right] \tag{1.13}$$

where $Z$ is the partition function that normalizes the probability. This result shows that the position of the bead is Gaussian distributed (Fig. 1.9 (a)).

The power spectrum of the bead position (Eq. 1.14) describes how the amplitude of position noise changes with frequency (Fig. 1.9 (b)) [45].

$$S_x(f) = \frac{k_B T}{\pi^2 \gamma (f_C^2 + f^2)} \tag{1.14}$$

where $f_C = k/2\pi\gamma = 1/2\pi\tau$ is the cut-off frequency, which is inversely proportional to the relaxation time of the trap. This equation implies that the amplitude of noise is constant for frequencies much lower than the cut-off frequency, whereas it decreases proportionally to $1/f^2$ at high frequencies (Fig 1.9 (b)). The variance $\sigma_x^2$ can always be obtained by calculating the area under the power spectrum, which gives the same result obtained with the equipartition theorem (Eq. 1.12). The cut-off frequency and the amplitude of thermal noise are strictly dependent on each other because of the existence of the system's relaxation time. In fact, since the bead's movements cannot occur on temporal scales faster than the relaxation time, all the collisions between the bead and the molecules of the buffer that happen at those

temporal scales, do not contribute to the thermal noise, which is then reduced at frequencies $f \gg f_C$.

In the case in which the bead is subjected both to thermal forces and to a constant external force, the resulting movement is described by adding the random motion described here and the motion described in the previous paragraph (1.2.1.2) [41].

#### *1.2.1.4 Measuring forces and displacements with optical tweezers*

The main advantage of optical tweezers is that they allow the observation of biological details up to the single molecule level, owing to their ability to measure forces and displacements on the cellular and molecular scales. Thus, it is possible to measure biological phenomena of great relevance, as forces and displacements applied by living cells, proteins' conformational changes and forces applied on biomolecules [34].

The movement of cells and biological molecules is measurable through the displacement of the bead to which they are bound. Light scattered by the bead in optical tweezers is collected by a position detector (generally, a quadrant photodiode) whose output is generally a differential voltage signal linked to the displacement of the laser beam and of the microsphere. The output voltage $V$ must be converted in a position signal $x$. In the same way, to measure forces exerted on the bead, it is necessary to know how the force $F(x)$ is linked to the bead displacement $x$. Therefore, two calibration curves are needed: $x(V)$ and $F(x)$. Since these curves have a linear trend in the proximity of the trap centre, optical tweezers calibration is reached by determining two parameters: the conversion factor of the position detector, $\beta$, and the trap stiffness, $k$. These equations hold:

$$F(x) = -kx \tag{1.15}$$

$$x(V) = \beta V \tag{1.16}$$

As mentioned above, the trap stiffness depends mostly on the power and the focussing of the laser beam, on the dimension of the microsphere, and on the refraction indexes of the bead and the surrounding buffer. To obtain a good sensitivity in force and displacement measurements, it is important to keep in mind that the conversion factor depends mostly on the type of detector used and its electronics, as well as on the microsphere characteristics. The maximum sensitivity can be reached by using beads of dimensions comparable to the trapping laser wavelength.

In literature we can find a great number of descriptions of different methods to calibrate optical tweezers [45], [48]–[51]: here we focus only on the method relying on the analysis of the power spectrum. Frequency analysis of thermal fluctuations of a trapped bead can provide both calibration parameters of optical tweezers. Determining the conversion factor $\beta$ means measuring the detector sensitivity ($\alpha = 1/\beta$). Since $\beta = x/V$, the power spectrum of the output voltage $V(t)$ of the photoelectric detector can be obtained from the power spectrum of the position $x$ of the bead through the following equation:

$$S_V(f) = \frac{1}{\beta^2}[S_x(f)] = \frac{1}{\beta^2}\frac{k_B T}{\pi^2 \gamma (f_C^2 + f^2)} \tag{1.17}$$

A complete calibration can be obtained simply through fitting of Eq. 1.17 on the experimental power spectrum of the voltage signal (Fig. 1.10), through the method of least squares. The experimental spectrum is measured when the particle is stably trapped by the optical tweezers. In the fitting procedure, the free parameters are the cut-off frequency $f_C$ and the conversion factor $\beta$. In this way, after obtaining the conversion factor $\beta$, we can also obtain the trap stiffness through the equation below (1.18):

$$k = 2\pi\gamma f_{C.} \tag{1.17}$$

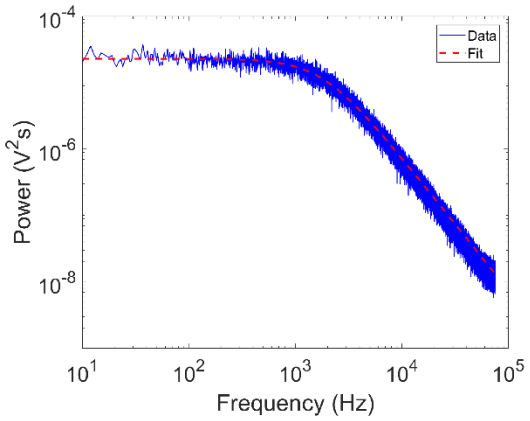


***Figure 1.10|Example of fitting of a power spectrum.*** *This spectrum $V(t)$ is measured for a 1 μm-diameter polystyrene bead in a watery buffer at room temperature. For frequencies under the cut-off frequency the noise is lower and almost constant, whereas at higher frequencies there is a relevant increase in the amplitude of the thermal noise. The fitting function is depicted in red.*

### *1.2.2 An indirect method: changing the substrate stiffness*

In the previous paragraphs we examined how optical tweezers can be used as handles to apply forces on biological systems at the single cell or molecule level. Another way to modulate forces and mechanical tensions on cells is by growing them on substrates characterized by different stiffnesses. From literature, it is known that the cell responds to substrate rigidity during functional and morphological differentiation with complex mechanisms that require more examination.

It has been proved that traction forces arising from the cell are influenced by the substrate's stiffness: cellular morphology plays a major role in this relationship. It has been observed that the extension of the area that cells occupy is higher when the stiffness of the substrate increases, and that the formation of a well-organized cytoskeleton is also facilitated, owing to formation of stable focal adhesions (Fig 1.11) [52].

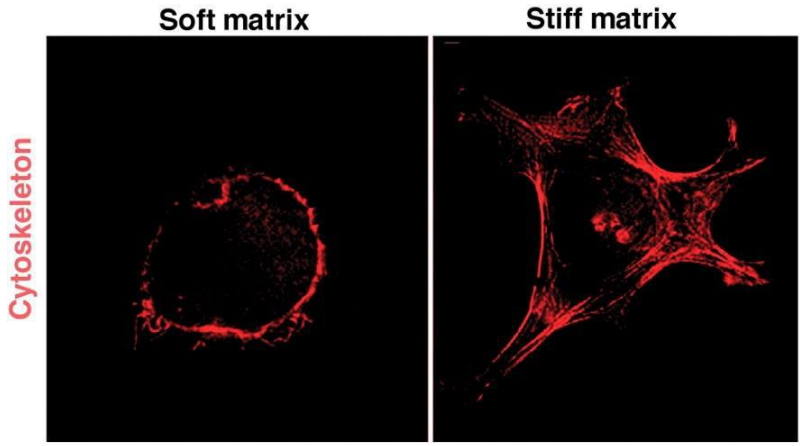


***Figure 1.11|Substrate's stiffness influences the extension of the cell and the assembly of the cytoskeleton.*** *Here, two fibroblasts were grown on hydrogels characterized by different stiffnesses: the lower stiffness' substrate on the left is characterized by an elastic modulus of* $E \sim 1\ kPa$ *, whereas the higher stiffness' hydrogel on the right is characterized by a elastic modulus of* $E \sim 100k\ Pa$*). Actin structures are revealed through fluorescence microscopy and are shown to be more organized on the stiffer matrix. In this case, in fact, the cell acquires an extended conformation, thus applying a higher tension on the cytoskeleton. Image retrieved by* [52].

By modifying substrate's stiffness, the mechanical forces applied on cell's adhesions change, and we can hypothesize that this change in tension is also reflected on cell's cytoskeleton. Growing cells on different substrates, moreover, also allows us to simulate the mechanical characteristics of various biological tissues of the human body. In fact, the complex system of the human body is composed by tissues that

cover a wide range of stiffness, spanning about six orders of magnitude between the intestinal mucus ($E \sim 11\ Pa$) and the cortical bone ($E \sim 20\ GPa$) (Fig. 1.12) [53].

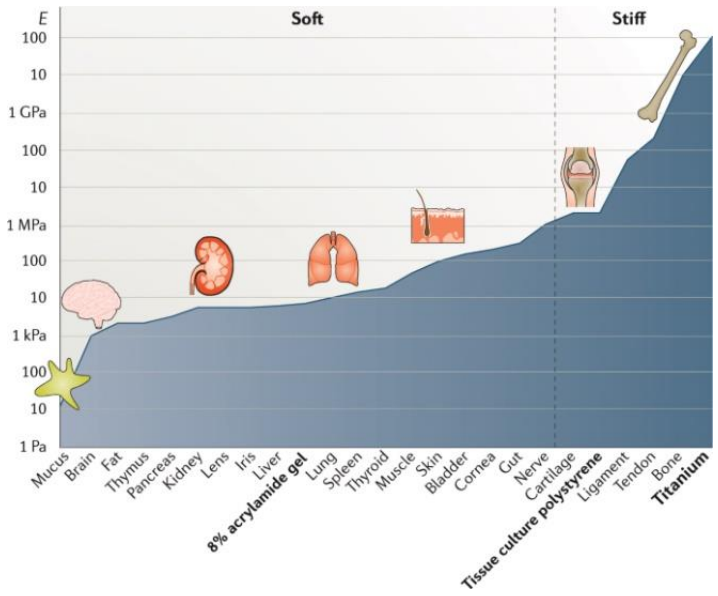


***Figure 1.12|Typical stiffnesses of human tissues.*** *The elastic moduli (E) of different tissues as described in the literature are reported on the left (logarithmic scale). Tissues are organized by increasing moduli. Image retrieved by* [53].

## 1.3 FRET (Forster Resonance Energy Transfer) MICROSCOPY

As previously mentioned in the abstract, recently, direct measurements of piconewton forces on distinct proteins inside cells has become possible by using genetically encoded molecular tension sensors, which are based on elastic peptides inserted between couples of fluorophores which undergo efficient FRET [3].

Therefore, I briefly introduce fluorescence microscopy, its advantages, and current state of the art. After that, I introduce theoretical background on the FRET phenomenon, further insights on the sensors used for force measurements, and the different methods available to measure FRET efficiency.

### 1.3.1 Fluorescence microscopy and advantages of fluorescent probes

If compared to other types of brightfield microscopy, fluorescence microscopy presents an intrinsic lower signal and a higher background. The principal characteristic that makes this type of microscopy very useful is its intrinsic specificity. Owing to this intrinsic selectivity, fluorescence imaging has become the most used microscopy method for the study of biological systems. The wide spectral range covered by all the available fluorophores allows the simultaneous observation of different cellular, sub-cellular and molecular components. Moreover, the existence of intrinsically fluorescent proteins, as for example GFP (Green Fluorescent Protein) and its variants, makes it possible to genetically tag proteins in living systems. Finally, the growing innovations in the development of fluorescence microscopy techniques (confocal, two-photon, super-resolution, light-sheet, etc.) provide a very powerful approach for the investigation of microscopic structure in three dimensions [54].

#### 1.3.1.1 Fluorescence and Stokes shift

Fluorescence is a phenomenon where the emission of light from an object occurs within few nanoseconds after the absorption of a radiation at a lower wavelength. What makes fluorescence such a powerful tool is exactly this difference between the excitation and the emission wavelength, which is known as Stokes Shift. In fact, by filtering the excitation wavelength during detection, without blocking the emission light, it is possible to observe only fluorescent objects. The molecules which are used for their fluorescent properties are called fluorophores: the orbitals of the outer

electrons of these molecules determine both their fluorescence efficiency and their excitation and emission wavelengths. When fluorescent molecules in the ground state absorb light (photons), variations in the electronic, vibrational, and rotational states of the molecule can occur: the absorbed energy can move an electron into a different orbital. The transition to an excited state occurs very rapidly on the time scale of femtoseconds, after which the fluorophore returns to its ground state by vibrational relaxation and fluorescence emission [54].

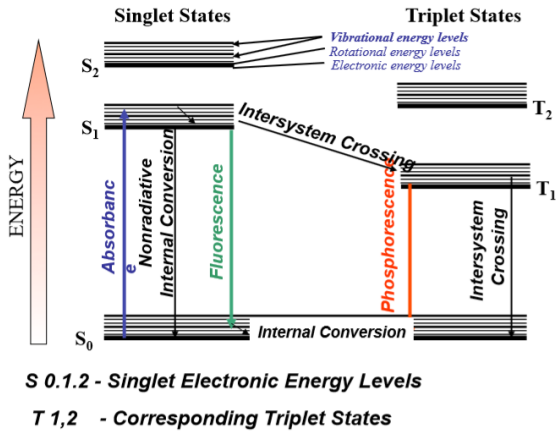


***Figure 1.13|Jablonski's diagram.*** *The diagram shows the energetic states of a molecule. Molecules which do not absorb energy are mostly confined in the lowest vibrational states of the ground state* $S_0$. *Image retrieved by* [54].

Excitation and emission processes can be better understood through a diagram, which was first depicted by Alexander Jablonski (Fig. 1.13). On the left part of the diagram are the singlet states: these states maintain the normal paired $+{}^1/_2$ and $-{}^1/_2$ spin states of the electrons. $S_0$ is the ground state and represents the energy of the molecule when it is not excited by any radiation. $S_1$and $S_2$ are excited singlet states, in which one outer electron is excited in a different orbital: $S_2$ has higher energy with respect to $S_1$, which in turn is higher than the ground state. On the right part of the diagram are the triplet states: in these states, an outer electron, which has been excited to a higher-energy orbital, is then subjected to a change in spin, leading to the formation of an electron pair with parallel spins. From quantum mechanics, this condition is forbidden and the only way for the electron to reverse its spin again is by undergoing through a forbidden transition, which is mostly unlikely to occur. Nevertheless, electrons can be subjected to a phenomenon called 'intersystem crossing' between the singlet and the triplet states. Singlet states return to the fundamental state through fluorescence emission, whereas triplet states undergo

phosphorescence emission. Phosphorescence is an emission phenomenon which differs from fluorescence because, while fluorescence ends as soon as illumination is interrupted, phosphorescence has a higher lifetime ($\sim 10^{-3} s$) and continues even for minutes after excitation is suspended.

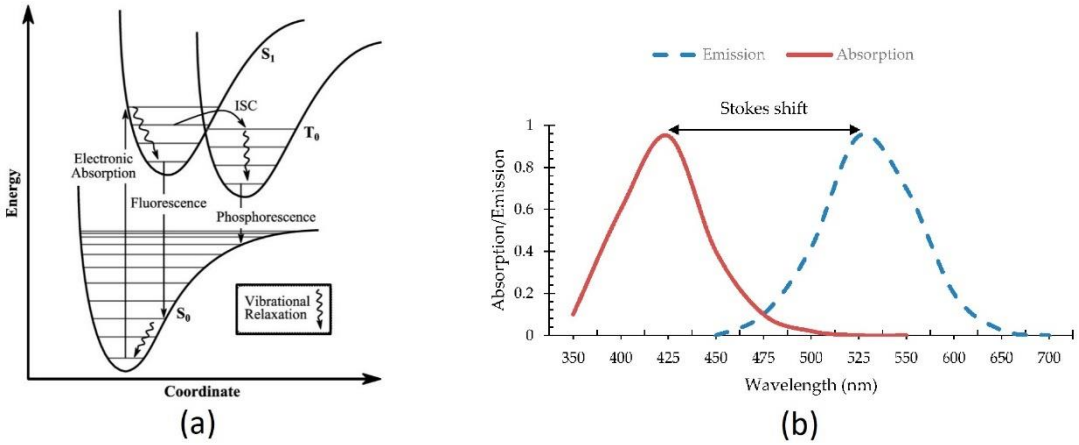


***Figure 1.14| Franck-Condon Principle and Stokes Shift representations. (a)*** *Potential curves of the fundamental and excited levels: energy absorption proceeds from the potential minimum and ends on a certain excited vibrational level (vertical absorption). The vibrational relaxation leads to the minimum of the excited potential curve, from which fluorescence emission proceeds.* ***(b)*** *Owing to internal relaxation, the emission spectrum is centred around a peak wavelength higher than the excitation one.*

The emission spectrum of one molecule is peaked around a wavelength which is higher with respect to the peak wavelength of the absorption spectrum: this happens because the excited energy is partially transferred to the surrounding environment before fluorescence emission, owing to the nuclear relaxation of the excited molecule and of the surrounding medium (Fig. 1.14 (b)). For this reason, factors as polarity and viscosity of the buffer, or its relaxation velocity, have an influence on fluorescence since they have a role in the energy level at which the fluorophore can be found. The resulting redshift of the molecule is called Stokes shift, because of its discovery by George Stokes. The Stokes shift reflects both the intramolecular vibrational relaxation and the surrounding buffer relaxation.

#### *1.3.1.2 Spatial resolution*

In the previous paragraph we discussed the main characteristics that make fluorescence microscopy one of the most suitable methods to study biological systems. However, fluorescence microscopy, as well as other optical microscopy

techniques, suffer from a great limitation: spatial resolution. In 1873, Ernst Abbe reported that there was a theoretical limit in the resolution of a light-based optical microscope. The resolution of an optical system is defined as the minimum distance between two light sources that allows to distinguish them as separate objects on the image plane created by the optical system itself. This distance depends on the wavelength $\lambda$ of the light used to create the image and on the numerical aperture $NA$ of the microscope objective as follows:

$$d = \frac{\lambda}{2NA} \tag{1.18}$$

For visible light microscopy this distance is $\sim 200\ nm$. This resolution is good enough to look at relatively large features such as organelles and cellular compartments, but many subcellular structures are much smaller than that.

When light passes through a circular aperture it is diffracted and creates a diffraction pattern known as "Airy disk" [55]. A lens such as a microscope objective acts like a circular aperture, transforming every point-like source of light into an Airy disk pattern on the image plane (Fig. 1.15). Thus, the Airy function coincides with the point spread function (PSF) of the circular aperture itself. More generally, the Airy function well approximates the PSF of real and more complex imaging systems, as an optical microscope [56].

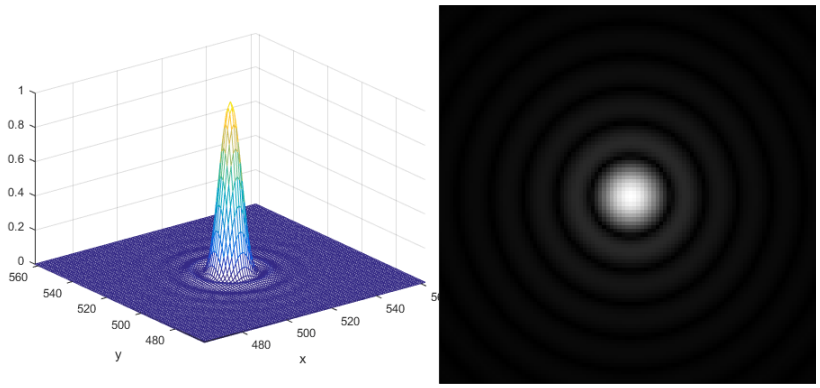


***Figure 1.15|Airy disk.*** *The image shows the Airy diffraction pattern generated by a point-like source on a camera chip.*

Based on this phenomenon, several criteria have been proposed to set the minimum distance between two point-like light sources to be spatially resolvable. The Rayleigh and Abbe criteria are the most used in microscopy (Fig. 1.16).

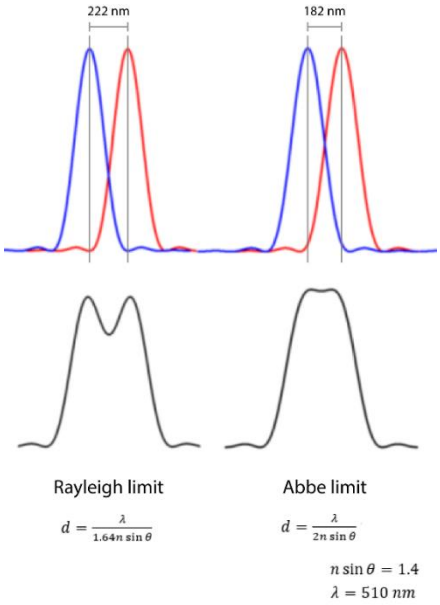


***Figure 1.16| The Rayleigh and Abbe diffraction limits and their definitions.*** *The values of d, which is the minimal resolvable distance for each criterion, are calculated from two point-like sources emitting at a wavelength of 510 nm and passing through an objective lens with a numerical aperture NA of 1.4. In the upper panel the two Airy patterns are plotted at a distance given by the diffraction limit, whereas in the lower panel the summed profiles are shown*

For Rayleigh criterion, $d$ corresponds to the distance at which the minimum of the first PSF overlaps with the maximum of the second one; for Abbe criterion, instead, it corresponds to the distance at which the peak of one Airy function overlaps with the zero of the second function. In both cases, $d$ depends on the wavelength λ of the light source, the refractive index $n$ of the medium in which the objective is immersed, and on the objective aperture angle $\theta$. The numerical aperture $NA = n \sin\theta$ of the objective can reach a maximum value of $NA \sim 1{,}4 - 1{,}5$ for common oil immersion objectives.

More recent developments in fluorescent microscopy have allowed to localize single molecules by using chromophores as fluorescent markers of single biologic molecules. The emission distribution of a single chromophore is described by the PSF, which is shaped as the Airy function. The image arising from a point-like fluorescent object is typically $\sim 250\ nm$ large in the visible region, owing to diffraction effects, but their real dimension is of the order of some nanometres. Therefore, when single molecule studies are performed, it is important to localize biological molecules with nanometric precision and localization accuracy must overcome the resolution limit imposed by diffraction effects. Recent advances in fluorescence microscopy have allowed reaching this aim by using the emission of fluorescent chromophores, which

can be bound in a specific way to molecules of interest in the sample. It is possible, in fact, to bind chromophores to antibodies targeting specific proteins in biological samples, as well as to fuse a gene coding a fluorescent protein with one of the protein of interest and transfect living cells to obtain the fluorescently labelled protein. The position of a fluorescent probe of this kind can be localized with high accuracy by determining the centre of its emission pattern. There are different methods to localize single molecules, but one of the best methods consists in bi-dimensional Gaussian fitting of the PSF [56].

#### *1.3.1.3 Different fluorescent markers*

Fluorescent molecules have a great number of applications both as probes to study structural changes that can occur in proteins or molecules and as markers to visualize intracellular components. Fluorophores can be divided in two classes: intrinsic fluorophores, that are naturally found in biomolecules, and extrinsic fluorophores, that can be chemically or physically bound to biomolecules. Recently, great advances have been achieved in the available techniques used to tag proteins inside cells, thus increasing the ability to reveal details of cellular events. A fundamental part of these advances has been possible thanks to the development of fluorescent proteins that can be incorporated into cells through genic fusion, thus producing fluorescent tags. Moreover, new techniques have made it possible to tag proteins with little organic fluorophores or nanocrystals [57].

One of the most important class of fluorophores comes from the isolation of the Green Fluorescent Protein (GFP), which was firstly isolated from Shimomura in 1962 [58] from *Aequorea Victoria* jellyfish (Fig. 1.17). GFP exhibits a bright green fluorescence when exposed to light with wavelengths in the range between blue and ultraviolet light: it shows a principal excitation peak at a wavelength of 475 nm and a secondary one at 395 nm; the emission peak is centred around of 509 nm. Since the *Aequorea* GFP is spontaneously fluorescent, chimeric fusions of GFP can be expressed *in situ* thanks to a genic transfer inside cells, without the need of complicated operations such as purification, *in vitro* labelling, or recombinant proteins injections. Moreover, these proteins can be localized at specific sites inside the cell thanks to appropriate targeting signals. Even if spectral variants with emission in the range of blue, cyan, and yellow have been generated from *Aequorea* GFP, none of these exhibit emission peaks higher than 539 nm (Fig. 1.18).

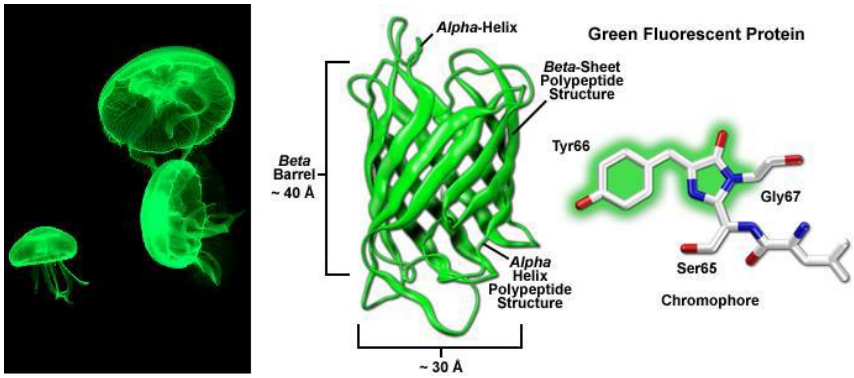


***Figure 1.17| Green Fluorescent Protein from Aequorea Victoria.*** *In the left part a photography of the fluorescent organism of Aequorea Victoria jellyfish is shown. In the central panel there is a scheme of the structure of the protein: it is composed by 238 amino acids, with a weight of 26.9 kDa. In the right part, the chemical representation of the chromophore that makes the protein fluorescent. Image retrieved by* [59].

Fortunately, the discovery of new "GFP-like" proteins in *Anthozoa*, which is a coral, has significantly expanded the range of available colours for biological cellular applications. As a result, the family of "GFP-like" proteins includes now approximatively 30 different members. The proteins that present fluorescence emission at wavelengths in the red or far-red range (RFPs: Red Fluorescent Proteins) are of particular interest, since eukaryotic cells and tissues show a reduced auto-fluorescence at those wavelengths. Moreover, RFPs can be used in combination with other fluorescent proteins that present fluorescence emission at shorter wavelengths, both for a multi-colour labelling and FRET experiments (Fig. 1.18).

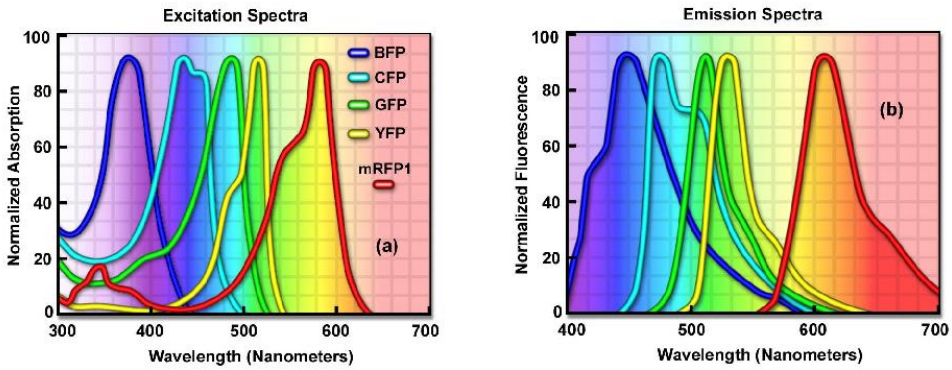


***Figure 1.18| GFP and RFP derivatives spectra.*** *On the left the excitation spectra of GFP-derived and RFP-derived proteins, on the right the emission spectra. The GFP-derived proteins emission spectra are always lower than 529 nm, which constitutes a limit since higher wavelengths are in a spectral region of reduced autofluorescence which allows to obtain a higher signal to noise ratio, thus allowing a more precise localization of the protein. The emission spectrum of RFP-derived protein (mRFP1), which is centred around 610 nm, allows to obtain a better signal to noise ratio and to perform a multi-colour staining in combination with GFP-derivatives. Image retrieved by* [60].

Despite the advantages offered by *in vivo* imaging through fluorescent proteins, they are relatively big (around 27 kDa if we consider the monomeric protein) to be used as protein markers. There is a great interest in reducing fluorescent protein dimensions, but genetic mutations have not produced the desired results so far. For this reason, the most promising results for small proteins tag come from the usage of small organic fluorophores like rhodamine and fluorescein, which are smaller than one kDa and can be positioned into specific sites of the protein by using non-trivial chemical labelling techniques. The important advantage obtained by using these small organic fluorophores is that possible interferences with the protein function are minimized. Moreover, the binding to a specific site of the protein allows studying conformational changes of the protein, as for example in FRET experiments. Recent *in vitro* experiments have used these little fluorophores as acceptors, in combination with a GFP-like donor [61], [62].

In addition to small organic fluorophores, semiconductor nanocrystals (i.e., quantum dots) represent a relatively recent and promising labelling method, thanks to their photostability and to the wide range of excitation and emission wavelengths available. Despite the advantages of quantum dots with respect to fluorescent proteins and organic fluorophores, their usage is limited by their lack of biocompatibility, which forces to cover them with compatible molecules layers, thus incrementing their size. However, new insights in the chemistry of surface coating have allowed the reduction of these problems, allowing a multicolour and long-term imaging of living cells [63]. Quantum dots are semiconductor nanocrystalline particles with a diameter typically in the 2-10 nm range, even if the organic coatings bring the effective diameter in a range between 5-20 nm. They offer numerous and important advantages with respect to fluorescent proteins and organic fluorophores, as for example the fact that they are characterized by tight and symmetric emission spectra. Moreover, the emission spectra can be regulated by changing the size and the material of the particles (Fig. 1.19): this property allows performing multicolour microscopy without spectral overlapping. Quantum dots excitation spectra, on the other hand, are very large, allowing simultaneous excitation of all the different coloured variants with a single excitation wavelength, thus minimizing the autofluorescence of the sample. Lastly, quantum dots have a very high photostability.

All the fluorescence labelling techniques of proteins described above have advantages and disadvantages which must be considered and weighted for every application, depending on the experiment that must be performed. The potentialities and the limitations of each technique must be evaluated to fully exploit the potential and obtain the maximum possible efficiency.

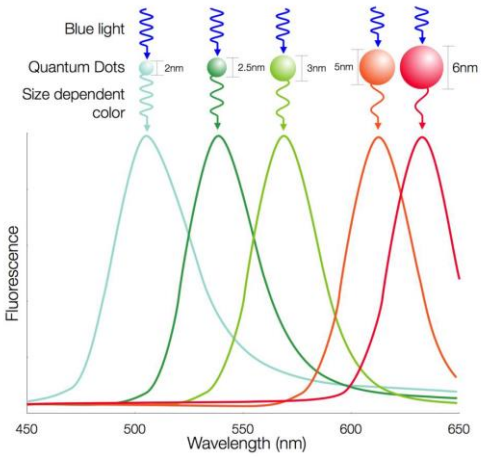


***Figure 1.19|Quantum dots' emission spectra vary with their dimension.*** *The emission wavelength peak of quantum dots changes with the diameter of the particle itself. When the diameter increases, the emission wavelength gets higher too. In this figure, all the quantum dots are excited by blue light, thanks to the fact that these particles present large excitation spectra.*

## *1.3.2 FRET: a molecular ruler*

As already said, fluorescence is a phenomenon which concerns the absorption of light by a fluorophore and the subsequent energy emission at a longer wavelength. If this emission is superimposed with the absorption spectrum of an acceptor fluorophore, an energy transfer without radiation emission can occur, provided that the two molecules involved are no more than few atomic diameters apart. This property is called *Förster Resonance Energy Transfer* (FRET) and its development began with Förster and Weber, which provided the first experimental and theoretical tools to use FRET to measure intramolecular and intermolecular distances. In 1967, Stryer and Haughland metaphorically called FRET "molecular ruler" and even today it represents one of the most used tools to measure distances in the 10-100 Å range. FRET is used to reveal conformational changes of the order of few Å, mostly in proteins.

FRET requires the use of two molecules: a fluorescent donor and an acceptor, that must be fluorescent too if we intend to use FRET to measure molecular distances. Irradiation of the donor with a radiation of light with an adequate frequency produces an oscillating dipole, which resonates with the acceptor dipole that is located nearby. For every donor-acceptor couple, the energy lost by the donor is transferred to the acceptor. The 'Jablonski diagram modified' (Fig. 1.20) shows the relationship between the vibrational energy states, the state of fluorescence and the resonance energy

transfer. Light absorption by a donor causes excitation from the fundamental singlet state ($S_0$) to a higher energy state, $S_4$. After that, a very quick decay occurs on the order of picoseconds from $S_4$ to the lowest vibrational state $S_1$. This decay is then followed by a slower one (on the scale of nanoseconds), from $S_1$ to the ground state $S_0$. This process is accompanied by a photon emission $Hv_F$ [64].

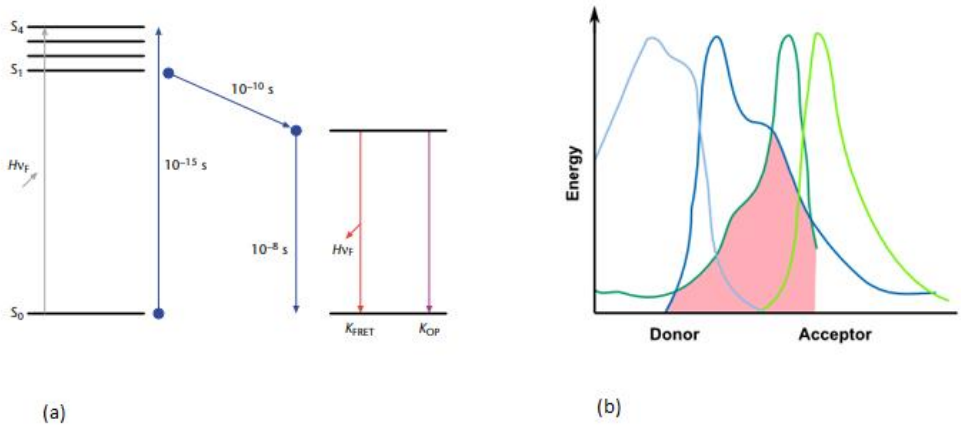


***Figure 1.20|Illustration of FRET mechanisms. (a)*** *'Jablonski diagram modified' indicates the energy levels of the donor in the ground state ($S_0$) and in the excited state ($S_{1,4}$). An energy transfer between the donor and the acceptor, which is not accompanied by radiation, weakens the fluorescence of the donor molecule. In figure, $Hv_F$ indicates the energy of the photon that is absorbed or emitted, $k_{FRET}$ is the resonance energy transfer rate, and $k_{OP}$ is the rate of all the relaxation processes different from FRET.* ***(b)*** *Excitation and emission spectra of donor and acceptor molecules: the pink-coloured region is the spectral overlapping $J_{da}$, i.e., the region where the emission of the donor coincides with the excitation of the acceptor. Image retrieved by* [64].

Fluorescence emission is only one of the numerous ways through which the donor, in its excited state, can lose its energy and return to the ground state. In fact, fluorophores can relax through a certain number of competitive processes, whose emission rates are the fluorescence rate $k_F$, the rate of energy loss in the form of heat due to internal conversion $k_{IC}$, the rate of bleaching or photo destruction $k_{PB}$, the rate of formation of a triplet state through 'intersystem crossing' $k_{ISC}$ and, finally, the rate of resonance energy transfer $k_{FRET}$. All the processes described are mutually linked and may take place in parallel, so that determining a rate allows to determine all the other rates. The most used procedure is to determine $k_{FRET}$ by observing $k_F$ in the presence or in the absence of the acceptor. There is a relationship between $k_{FRET}$ and the fluorescence lifetime of the donor (τ) given by:

$$\frac{1}{\tau} = k_{FRET} + k_{OP} \tag{1.19}$$

where $k_{OP}$ is the rate of all of the relaxation processes different from FRET. From Eq. 1.19 we can observe that an increase in $k_{FRET}$ brings to a reduction of the donor lifetime. If a significative loss of energy through processes different from FRET occurs, this will be reflected in an introduction of significative errors in the calculation of the donor-acceptor distance.

FRET efficiency, which is the efficiency of energy transfer from the donor to the acceptor fluorophore, is defined as follows:

$$E = 1 - \frac{I_{DA}}{I_D} \tag{1.20}$$

where $I_{DA}$ is the fluorescence emission intensity of the donor in the presence of the acceptor, whereas $I_D$ is the emission intensity of the donor when the acceptor is not present. If the whole intensity of the donor is transferred to the acceptor, we have that $I_{DA} = 0$ and, thus, FRET efficiency will have a maximum value ($E = 1$).

The important characteristic of FRET efficiency is that it strongly depends on the distance between the pair of fluorescent proteins that undergo FRET. Thus, the determination of this value is a powerful tool to determine intramolecular distances, and that is the reason why it is called 'molecular ruler'. Förster's equation (Eq. 1.21) defines the elements needed to calculate the donor-acceptor distance:

$$E = \frac{1}{1 + {R^6}/{R_0^6}} \tag{1.21}$$

In Eq. 1.21, $R_0$ is called Förster's radius, and is the distance at which FRET efficiency is equal to 50%, and it is defined through the equation below:

$$R_0^6 = (8{,}79 \times 10^{23})\kappa^2 n^{-4} \Phi_d J_{da} \tag{1.22}$$

Here (Eq. 1.22) $R_0$ is expressed in angstrom, $\kappa^2$ is the orientation factor (dimensionless number), $n$ is the refractive index of the buffer, $\Phi_d$ is the quantum yield of the donor, that is the ratio of the number of photons emitted to the number of photons absorbed, and $J_{da}$ is the spectral overlap (Fig. 1.20 (b)), which can be defined as:

$$J_{da}(\lambda) = \frac{\int I_d(\lambda)\varepsilon_a(\lambda)\lambda^4 d\lambda}{\int I_d(\lambda)\, d\lambda} \tag{1.23}$$

In the integral, $I_d(\lambda)$ is the intensity of donor emission in the absence of the acceptor and $\varepsilon_a(\lambda)$ is the molar extinction coefficient of the acceptor at the wavelength $\lambda$. The spectral overlap integral $J_{da}$ is measured in $cm^3M^{-1}$ [64].

An important factor to evaluate to obtain significative information through FRET experiments is the dependence of FRET efficiency on the relative orientation between the donor and the acceptor dipoles. Different conformations of the donor-acceptor couple can make $\kappa^2$ assume different values in the range $0 \leq \kappa^2 \leq 4$. If the dipole moments assume all the possible orientation angles with respect to the substrate (i.e., isotropy condition) in a time interval much shorter than the time taken for the energy transfer to be completed (dynamic mean condition), the mean value of the orientation factor is $\langle\kappa^2\rangle = 2/3$. However, when measuring FRET efficiency in biological systems, it may happen that these conditions are not satisfied. Polarization spectroscopy can be used to obtain information both on the donor and acceptor rotational degrees of freedom and on their relative orientation. This information usually are not enough to define a precise value for $\kappa^2$, but often can provide a range of values with realistic lower and upper limits [64].

### *1.3.3 Methods to measure FRET efficiency*

The relationship between FRET efficiency and fluorescence intensity is given by the definition of efficiency (Eq. 1.20), that indicates the efficiency of transfer of the donor emission to the acceptor molecule. In order to use this equation to measure efficiency, it is necessary to perform two fluorescence intensity measurements: with and without the acceptor fluorophore. This can be done in a sequential manner, by measuring before and after the acceptor photobleaching in the same sample, so that there are no changes in the donor concentration, since the fluorescence intensity is proportional to the fluorophore concentration. This approach assumes that all of the acceptor molecules has undergo complete photobleaching in the region of interest, while the donor molecules are still fluorescent: this condition is very difficult to verify in practical experiments. An insufficient photobleaching of the acceptors or a simultaneous bleaching of the donors can result in an underestimated FRET efficiency value. To avoid this problem, FRET efficiency is usually measured by using another method which is called *Acceptor sensitized emission*. To use this method, it is useful to notice that FRET efficiency, under continuous excitation of the donor molecule, is also related to a ratio between the acceptor fluorescence intensity $I_{AD}$ and the intensities of the acceptor and the donor $I_{DA}$ and $I_{AD}$, as described by the following equation:

$$E = \frac{I_{AD}}{I_{AD} + \gamma I_{DA}} \tag{1.24}$$

where $\gamma$ is a factor that considers the differences in fluorescence quantum yield of the donor and the acceptor molecules, as well as the differences in detection efficiency of the same. $\gamma$ can be experimentally determined by using Eq. 1.25.

$$\gamma = \frac{I_{AD}}{I_D - I_{DA}} \tag{1.25}$$

In Eq. 1.25, $I_{AD}$ has been corrected for the so called 'spectral bleed through'. The spectral bleed through is the phenomenon for which, since the spectra of the two fluorophores are partially overlapped, it can happen that a portion of the donor fluorescence (or of the acceptor alone) can go into the channel of FRET emission. These contributes can lead to overestimate FRET efficiency; thus, it is necessary to take it into account and eventually correct for it. To do this, some special constructs that contain only the donor (or acceptor) molecule are used. Moreover, a systematic determination of the acceptor intensity $I_{AA}$ must be done for every measurement of $I_{AD}$ and $I_{DA}$.

Alternatively, it can be convenient to operate without determining the factor $\gamma$ nor the bleed through corrections and to define a FRET index, as for example $I_{AD}/(I_{AD} + I_{DA})$. A similar approach is as fast as the standard imaging of fluorescence intensity can be and thus is suitable for rapid biological processes. FRET efficiency can then be obtained through a calibration of the FRET index, by using standard FRET constructs previously used with known FRET efficiencies [65]. The majority of MTM (Molecular Tension Microscopy) studies that can be found in literature have used this method to define a FRET index and then adopted the method of the 'acceptor sensitized emission' described above [4].

### *1.3.4 FRET force sensors*

Mechanical forces have a key role in physiological processes, in the onset of pathologies and in the development of cells. However, as discussed above, a complete knowledge of the mechanisms of the transmission of forces inside cells has not been achieved yet, thus constituting a major obstacle in revealing molecular mechanisms. For this reason, different genetically encoded force sensors have been studied and

engineered, whose generic structure is constituted by an elastic peptide inserted between a couple of fluorophores that undergo efficient FRET.

#### *1.3.4.1 Distance-based FRET sensors*

The first FRET force sensor that was engineered was designed by Meng, Suchyna and Sachs [66] and it's called "stretch sensitive FRET" (stFRET) (Fig. 1.21 (a)). This sensor consisted of mutants of the GFP proteins which are called Cerulean and Venus, linked by a stable alpha-helix. This cassette could be inserted successfully into structural protein hosts such as collagen, myosin, filamin, actinin and spectrin [66], [67]. stFRET opened the way to the study of mechanical stress driven physiological processes in real time in biological systems. With time, other research group began to design other similar force sensors. One of the first sensors that has been created and successfully calibrated was engineered by Grashoff et al. [68] and is called "tension sensor module (TSMod) (Fig. 1.21 (b)). It is a calibrated biosensor that can measure forces in specific proteins inside cells with piconewton sensitivity. It consists of an elastic domain constituted by 40 amino acids which is inserted between the two fluorescent proteins mTFP1 and Venus(A206K), which undergo FRET.

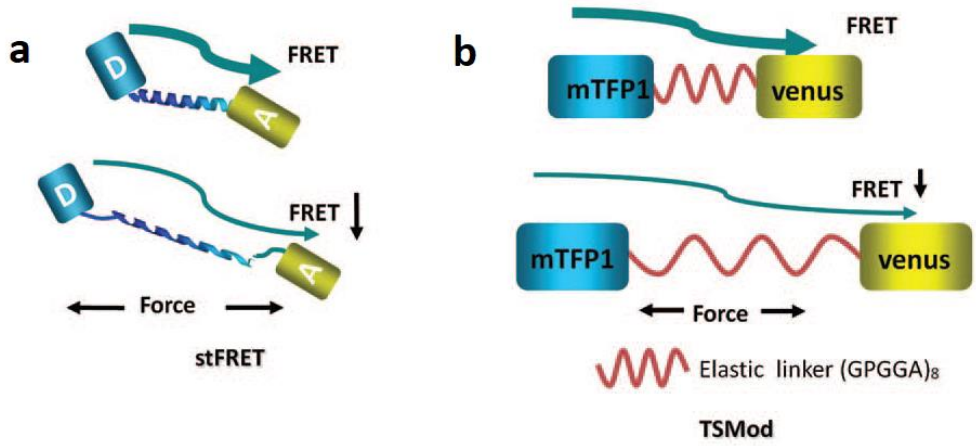


***Figure 1.21| Distance-based FRET sensors. (a)*** *stretch sensitive FRET (stFRET) sensor. The force sensor module consists of two mutant GFPs (Cerulean and Venus) separated by an alpha-helix. When forces that act on the sensor stretch the elastic linker (lower image), FRET efficiency decreases.* ***(b)*** *Tension sensor module (TSMod). The force sensor module consists of two fluorescent proteins separated by a flagelliform linker sequence* $(GPGGGA)_8$*. When forces that act on the sensor stretch the elastic linker (lower image), FRET efficiency decreases. Image retrieved by* [69].

TSMod sensor was successfully incorporated into the flexible linker domain between head and tail domains of vinculin, thus allowing the estimation of the tension applied to focal adhesions through vinculin, which resulted to be higher at the leading edge of migrating cells and lower at the lagging edge [70]. TSMod sensor allows measuring forces in the 1-6 pN limited range by using FRET. Inside cells, myosin motors produce forces on the actin cytoskeleton which are transmitted to numerous subcellular structures and macromolecular complexes. Single myosin motors can generate forces up to 5-10 pN and it has been proven that forces that act through distinct integrins receptors are significantly higher than the ones measured with TSMod [4].

Therefore, two tension sensors have been engineered by using the villin headpiece peptide HP35, which is 35 amino acids long, as the tension-sensitive element, flanked by the couple of fluorophores YPet and mCherry (Fig. 1.22 (a)). The HP35 peptide is characterized by very rapid folding and by a folding/unfolding transition at equilibrium in response to mechanical forces of about 7 pN. A stable mutant of HP35, called HP35st, is subjected to this transition when the force applied is around 10 pN [71]. For these reasons, this sensor is able to measure mechanical tensions occurring in living cells in a range of forces which is higher (6-11 pN) with respect to force values measurable by TSMod.

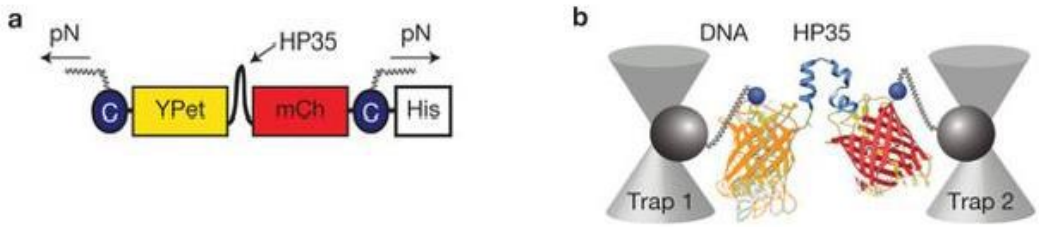


***Figure 1.22|HP35 distance-based FRET sensor and its calibration. (a)*** *Structure of the HP35-TS sensor, which comprehends the two fluorophores YPet and mCherry, which are linked by a villin peptide (HP35). Mechanical forces that act on the sensor lead to the unfolding of HP35, which in turn is translated into an increase in the distance between the fluorophores and, thus, to a reduction of FRET efficiency.* ***(b)*** *Schematic illustration of the double-trap optical tweezers setup which has been used for calibration: to calibrate the single molecule, DNA filaments have been used, which allow to attach the microspheres to the fluorophores.*

The HP35 sensor has then been calibrated through single molecule measurements by using a setup constituted by a double trap optical tweezers system (Fig. 1.22 (b)). The mean equilibrium transition values have been determined to be 7,4 pN for HP35-TS and 10,6 pN for HP35st-TS, and it has been observed that both sensors quickly go back to their original conformation when the force ceases (reversable unfolding transition), thus allowing measurements of cell's dynamics.

Starting from these modules, numerous other sensors of this kind have then been engineered, depending on the experiments to perform and on the proteins under exam.

#### *1.3.4.2 Orientation-based FRET sensors*

The sensors showed until now have the characteristic to elongate in response to a uniaxial stress, and this elongation can be detected through a couple of fluorescent molecules which undergo FRET. In contrast to this kind of sensors, it has been developed a sensor module, called cpstFRET, which allows taking advantage from FRET sensitivity to the relative orientation between the dipoles of the two fluorophores [4]. This sensor is constituted by a 5 amino acids-long linker that connects to two circularly permuted fluorescent proteins, which are parallel at rest and rotate towards a perpendicular configuration when subjected to tension (Fig. 1.23). Therefore, the cpstFRET sensor is much smaller than the distance-based force sensors.

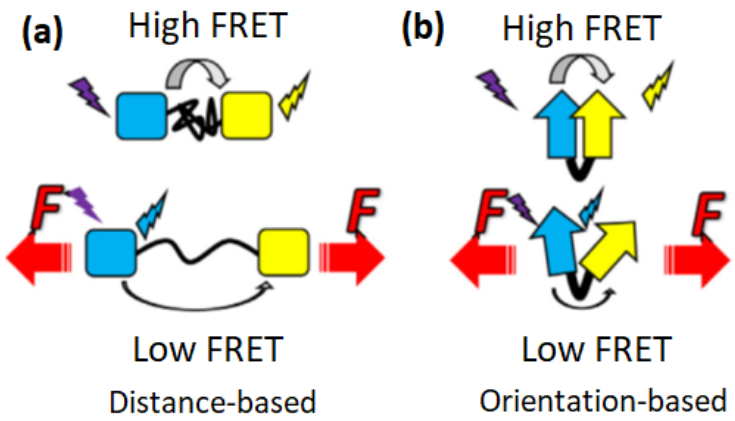


***Figure 1.23|Comparison between distance- and orientation-based FRET sensors. (a)*** *Schematic of the mechanism of distance-based FRET sensors. When a uniaxial tension is applied, the elastic linker stretches and the two fluorophores get more distant, thus bringing to a lower FRET signal.* ***(b)*** *Schematic of the mechanism of orientation-based FRET sensors. At rest, the dipoles of the two dipoles are parallel; when a stress is applied, they rotate towards a perpendicular configuration, resulting in a decrease of the FRET signal as well. Image retrieved by* [4].

Most of the FRET sensors that are commonly used are made of couples of donor-acceptor fluorophores of the CFP-YFP type. Each fluorophore couple has different advantages and disadvantages and the couple to be used must be chosen according to the specific experiment.

#### *1.3.4.3 Insertion of FRET sensors into proteins*

The different FRET-based tension biosensors, up to date, have been tested on a growing number of proteins: the target proteins include cytoskeleton proteins as α-actinin, spectrin, actin, and other proteins of cellular adhesion such as vinculin, E-cadherin, PECAM-1 and many others. In principle, the sensor can be inserted in any of these proteins and in any site that is subjected to mechanical forces. As an example, the cpstFRET sensor has been inserted into actin filaments, by flanking the sensor module with two monomers of β-actin, so that the sensor could be inserted in the polymer without inserting it in the single monomer. By operating in this manner, the sensor should presumably transmit tension from one side of the filament to the other [72]. The insertion of the two fluorescent proteins and of the linker is not a trivial modification of the protein structure since the total length of the sensor cassette could overcome 600 amino acids. Thus, it is necessary to have a good knowledge of the amino acids sequence and of the structure of the protein where we want to insert the sensor, to avoid that the modification disrupts the protein's functions.

To assert if the protein under exam is subjected to tension, it is necessary to compare it with some control constructs which do not undergo changes if subjected to mechanical forces. To do this, a certain number of constructs have been developed: the sensor module alone (not inserted in any protein), the sensor module attached to the C- or to the N- terminus of the protein, or the sensor attached to the protein which is then truncated or mutated at one extremity (Fig. 1.24).

Since all these sensors lack a binding site at least at one extremity of the sensor, it is presumably not subjected to forces. Not any protein, however, exhibits tension in any cellular line. For example, the protein spectrin is not subjected to significant tension in HEK cells [73], as well as PECAM-1 that does not exhibit tension in endothelial cells if they are not subjected to shear stresses [74].

For these reasons, a comparison with control constructs and experiments to ensure that the control localizes where the sensor-transfected protein localizes too, are always needed and of great importance, owing to the strong sensitivity of FRET from the surrounding environment [4].

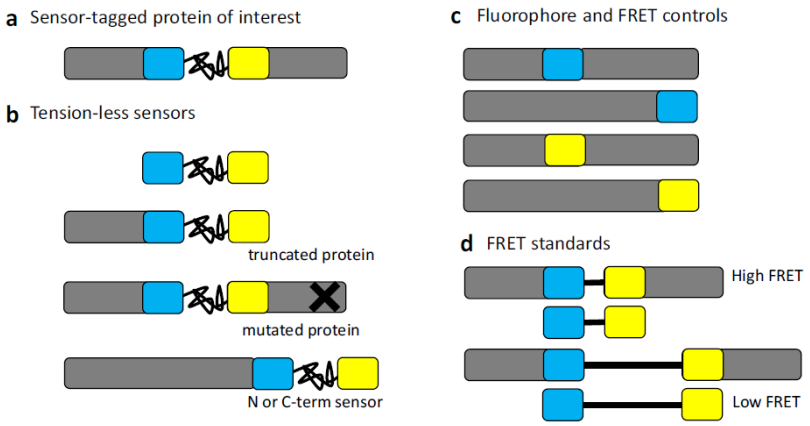


***Figure 1.24| Overview of MTM constructs. (a)*** *Sensor-tagged in the full-length protein of interest: the sensor is inserted into a specific site of the protein under exam.* ***(b)*** *Tension-less control constructs: the sensor alone, the sensor attached to the C- or N-terminus of the protein, or the sensor-tagged protein mutated or truncated at one end.* ***(c)*** *Fluorophore and FRET controls. Proteins with only the donor (or acceptor) fluorophore at the sensor insertion sites or at the N- or C- terminus, useful for localization control and for bleed through corrections.* ***(d)*** *FRET standard constructs with known efficiency consist of two fluorophores separated by a rigid peptide sequence. Image retrieved by* [4].

# 2 Setup implementation: combining optical manipulation and fluorescence microscopy

In order to directly observe and image the response of biological systems to mechanical stimulation, the experimental arrangement combines optical tweezers and fluorescence microscopy. A schematic of the apparatus is shown in Fig. 2.1. The system allows for the simultaneous manipulation of specific cell membrane receptors and detection of intracellular signals, with sensitivity down to the single molecule [5].

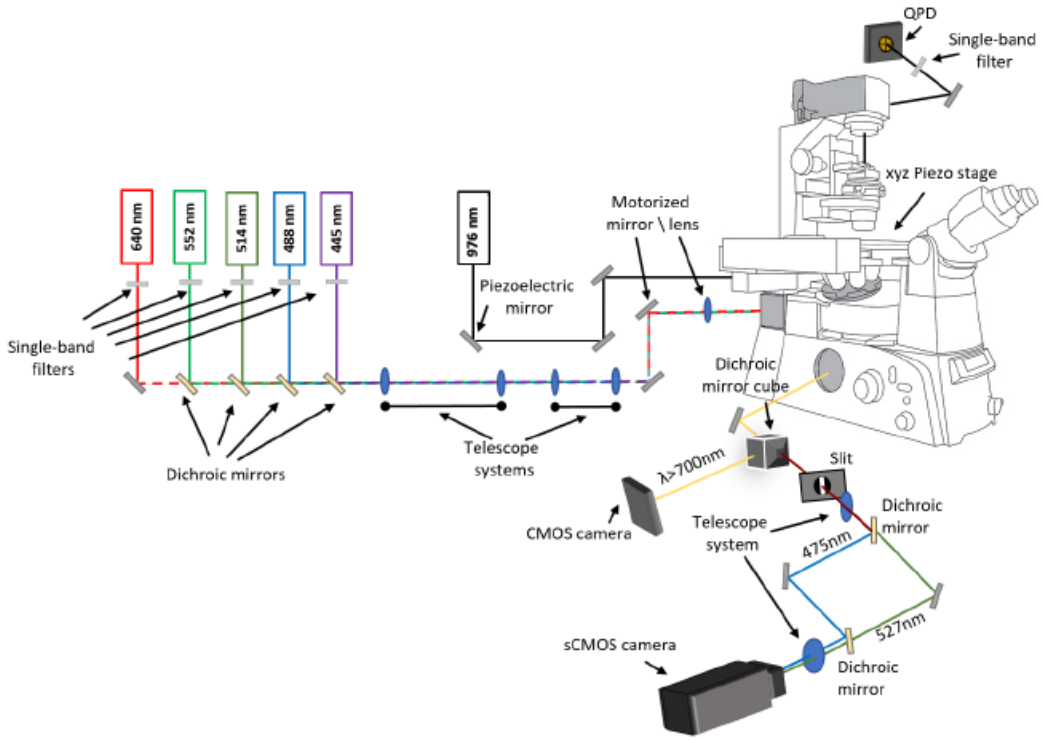


***Figure 2.1| Experimental setup combining optical tweezers and fluorescence microscopy.*** *Schematic of the experimental setup used in the mechanotransduction experiments. The apparatus combined dual-colour fluorescence microscopy and optical manipulation by optical tweezers.*

The setup is realized around a commercial inverted microscope (Nikon Eclipse Ti-U). This is an infinity-corrected microscope, so that the image produced by the objective is projected to infinity and the tube lens is positioned between the objective and the camera to produce the image on the camera itself. The commercial microscope has been adjusted to accommodate different excitation and emission wavelengths. Different illumination schemes such as highly inclined and laminated optical illumination (HILO) and total internal reflection fluorescence (TIRF) microscopy are obtained by using motorized mirrors and lenses mounted on the optical table. The microscope objective (Nikon CFI Apochromat TIRF, 60X magnification and numerical aperture NA=1.49) provides high transmission and an efficient correction

of chromatic aberrations in the range from 435 nm to 1064 nm: this allows to image the single molecules in the visible range and to trap particles for optical manipulation with a near-infrared laser (976 nm peak wavelength) on the same focal plane. The microscope is equipped with a piezoelectric stage (PI PInano P-545) that is able to translate the sample along three directions ($200\ \mu m \times 200\ \mu m \times 200\ \mu m$) with nanometre steps and step time response of the order of few milliseconds, allowing for rapid and precise positioning and stabilization of the sample [50]. Moreover, the piezoelectric stage is mounted on a high stable motorized stage (PI M-545) characterized by the capacity of performing long-range displacements ($25\ mm \times 25\ mm$). The optical trap can be moved independently from the stage by tilting the laser beam near to the source with a piezoelectric mirror, allowing for the decoupling of fluorescence imaging from optical manipulation. The movement of the stage, the operation of the laser sources and collection of data from the different detectors can be remotely controlled by a custom-made software package. An acquisition board (National Instruments PCIe-6343) is used for data acquisition. The latter consists of 32 analogue inputs with 16-bit resolution and sampling rate of 500 kS/s, and 4 analogue outputs with the same resolution and sampling rate of 900 kS/s. The whole optical setup is positioned on an anti-vibration optical table (Melles Griot) to minimize mechanical vibrations [5].

## 2.1 Optical tweezers implementation

### 2.1.1 Optical trapping

The optical tweezers system has been developed to precisely apply external forces on cell membranes by trapping microscale beads and bring them in contact with the cells. Optical manipulation is accomplished by a diode laser (Thorlabs BL976-PAG900), emitting at 976 nm with FWHM of 0.8 nm and maximum power $P_{max} = 900\ mW$. The choice of this wavelength was made to minimize photodamage effects in living cells, which are known to be significantly reduced in the near-infrared region [75]. The diode laser is driven by a compact laser diode driver (Thorlabs CLD1015) (Fig. 2.2).

The trapping beam is directed toward the microscope through a piezo-driven steerable mirror. The piezoelectric mirror (PI N-480 PiezoMike) has an angular range of $\vartheta = \pm 5° = \pm 87\ mrad$ and a minimum angular resolution of $0.3\ \mu rad$. The piezoelectric mirror is conjugated to the back focal plane of the microscope objective through a $M = 10\times$ magnification telescope: in this way, the beam size is adjusted to slightly overfill the back aperture of the objective and a rotational movement of the piezo-mirror is translated into a linear movement of the trap in the sample plane (Fig. 2.2, grey background). The lateral movement of the trap $x$ can be calculated through the following equation:

$$x \sim \vartheta\, {f_0}/{M} \tag{2.1}$$

where $f_0 = 3.33\ mm$ is the focal length of the objective [41]. Considering the angular range of the piezoelectric mirror written above, the lateral movement of the trap could then span from a minimum lateral displacement of $x_{min} \sim \pm 0.1\ nm$ to a maximum displacement of $x \sim \pm 29\ \mu m$.

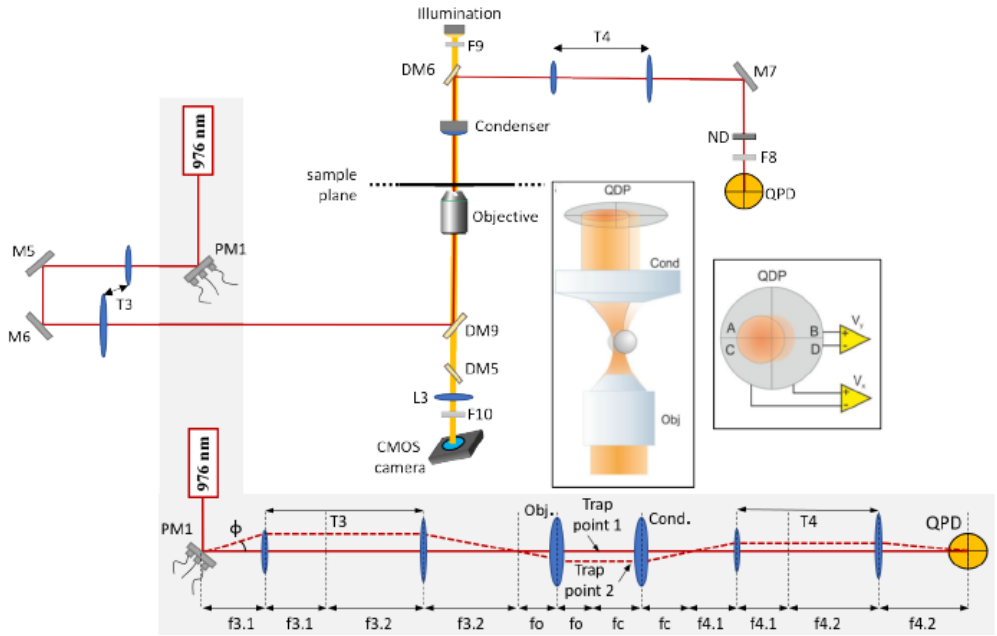


***Figure 2.2|Schematic of the optical manipulation part of the experimental apparatus.*** *A 976 nm laser source is used for the optical tweezers system. The piezoelectric mirror PM1 is used to stir the trapping beam to move the optical tweezers in the sample plane. The bottom grey area shows how the rotation of the piezoelectric mirror, and the placement of optics can result to a new trap position. f3.1 and f3.2 denote the focal lengths of the lenses of the telescope T3, f0 is the focal length of the microscope objective, fc of the condenser and f4.1 and f4.2 the focal lengths of the lenses of the telescope T4. The beam is passer through the telescope T3 to enlarge the beam to overfill the microscope objective back aperture. A dichroic mirror DM9 directs the trapping beam to the microscope objective. After passing through the sample, the beam light is collected by the condenser and reflected by the dichroic mirror DM6 to the QPD. The beam is then passed through the telescope T4, through an ND filter, and through a notch filter F8, before finally reaching the QPD. Inset: interaction of scattered and unscattered light creates an interference pattern depending on the relative position between the trapped sphere and the trap centre-of-mass. The intensity distribution can be measured through the differential voltage signals revealed by the QPD* [5].

Finally, the trapping beam is directed to the microscope objective by a dichroic mirror (Chroma ZT775sp-2p). The Nikon Eclipse microscope allowed to insert an extension turret between the fluorescence dichroic wheel and the microscope objective, which is the one that conveniently accommodates the tweezers' dichroic mirror. A calibration curve to describe the relation between the diode current and the optical power of the beam was plotted by measurements after the microscope objective (Fig.2.3). The power measured after the objective was taken as the power incident on the sample.

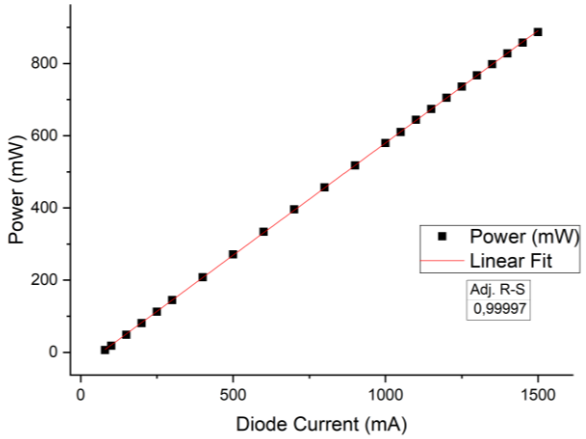


***Figure 2.3| Linear fit of the optical power of the beam with respect to the diode current.*** *Measurements of the optical power of the infrared laser at the fibre output were taken while changing the current of the laser diode. A fit was performed to verify that the relation was linear (Adjust R-Square = 0,99). After validation of linearity, the optical power measured after the microscope objective was taken as the power incident on the sample.*

Regarding detection, a quadrant photodiode detector (QPD) (OSI Optoelectronics SPOT-15-YAG) with custom-built 30 kHz bandwidth electronics is used to record the position of the trapped microspheres. This is made by using back-focal-plane interferometry, thus collecting the interference pattern that forms at the condenser back focal plane [41]. In this technique, the same laser source is used for both trapping and detection: the trapping laser beam, after being focused by the objective in the sample plane, is collected by the condenser and projected on the QPD positioned in a plane conjugated to the condenser back focal plane (Fig. 2.2, grey background). The telescope T4 is used both for creating the conjugated plane and for adapting the beam size to the QPD sensor. In this configuration, the image of the interference pattern between light scattered by the trapped particle and the unscattered light is projected on the detector [76]. The distribution of the interference pattern depends on the position of the bead with respect to the trap (Fig. 2.2, inset). The intensity centre-of-mass can be measured from differential voltage signals $V_x, V_y$ with a variable gain (g) that, in turn, are obtained from the four quadrants currents $i_A, i_B, i_C, i_D$ by an electronic circuit that performs the following operations:

$$V_x = g\frac{(i_A + i_C) - (i_B + i_D)}{i_A + i_B + i_C + i_D}, \qquad (2.2, \text{a})$$

$$V_y = g\frac{(i_C + i_D) - (i_A + i_B)}{i_A + i_B + i_C + i_D}, \qquad (2.2, \text{b})$$

Tension signals are linearly dependent on the bead displacements.

The light is directed to the QPD by means of a dichroic mirror (Chroma ZT775sp-2p), which reflects wavelengths between 775 nm and 1200 nm and is mounted on top of the condenser. The condenser lens has a relatively low numerical aperture ($NA = 0.52$) and high working distance to allow the use of cell culture dishes and a microscope incubator (Okolab H301 chamber with UNO-T-H-CO2 all-in-one controller).

In a later development of the experimental setup, the trapping laser has been split into two beams to allow for double trap configuration, by using polarizing beam splitters and mirrors. Moreover, the second lens of the telescope system T3 was substituted with a tunable lens by Optotune (EL-10-30-TC-NIR-12D), which allows to change the focal distance of the lens in the range between 55 mm and 120 mm. This lens will allow to move the trap not only in the $\widehat{xy}$ plane, but also in the axial direction [77].

### 2.1.2 Calibration of the trap stiffness

Calibration of the optical tweezers system is performed by analysing the trapped bead position frequency spectra [45]. This is essential to quantify forces and displacements experienced by living cells. The calibration allowed to determine both the trap stiffness $k$ and the conversion factor $\beta$. Determining the conversion factor is equivalent to measuring the sensitivity of the QPD $\alpha = 1/\beta$. Since $\beta = x/V$, the power spectrum of the output voltage $V(t)$ of the photoelectric detector can be obtained from the power spectrum of the position $x$ of the trapped beam through the equation:

$$S_v(f) = \frac{1}{\beta^2} \frac{k_B T}{\gamma \pi^2 (f_c^2 + f^2)} \tag{2.3}$$

where $k_B$ is the Boltzmann constant, $T$ is the temperature, $\gamma = 6\pi\eta R$ is the viscous drag coefficient for a sphere of radius $R$ immersed in a fluid of viscosity $\eta$, and $f_C$ is the cut-off frequency. Trap calibration can be obtained by fitting the voltage power spectra recorded while a particle is stably trapped by the optical tweezers by using Eq. 2.3 and the least squares method. An example of a fitted frequency spectra is shown in chapter 1 in Fig. 1.10. The cut-off frequency and the conversion factor are the

parameters that are set as free parameters in the fitting procedure. The value obtained for $f_C$ is used to calculate the trap stiffness through the equation below:

$$k = 2\pi\gamma f_{C.} \tag{2.4}$$

The linear dependence of the trap stiffness, as well as the independence of the voltage-to-position calibration factors on laser power, have been tested for different kind of beads.

### *2.1.3 Cell membrane stimulation*

To test the experimental setup, we performed a cell membrane stimulation experiment. Optical tweezers can be used to manipulate specific receptors on the membrane of living cells by applying forces through a trapped bead, to investigate on mechanotransduction processes. As an example, after application of forces, structural changes in the membrane receptors can occur and the application can also trigger intercellular processes. Fig. 2.4 shows an illustrative cell manipulation experiment in which a fibronectin-coated polystyrene bead is attached to the cell membrane and then pulled away from it. The bead binds to the cellular membrane while the force is applied by forming a membrane tether [34], which is clearly visible in Fig. 2.4 (a) on the right. The QPD signal is recorded during this process, allowing the calculation of the applied force on the membrane during tether pulling (Fig. 2.4 (b)). The conversion factor $\beta$ is then determined by fitting the power spectra through Eq. 2.3 and, together with the difference in voltage signal as recorded by the QPD for each step, it allows to calculate the trapped bead mean displacement by using equation 2.5.

$$x = \sum_i x_i = \sum_i \beta \Delta V_i \tag{2.5}$$

The force is then calculated for each step by using the trap stiffness obtained from the power spectra fitting as well. The mean force is then calculated, revealing a linear relationship with the mean displacement of the trapped bead. Finally, the tether stiffness with its error is obtained by linear fit of the data with Hooke's law (Fig. 2.4 (c)).

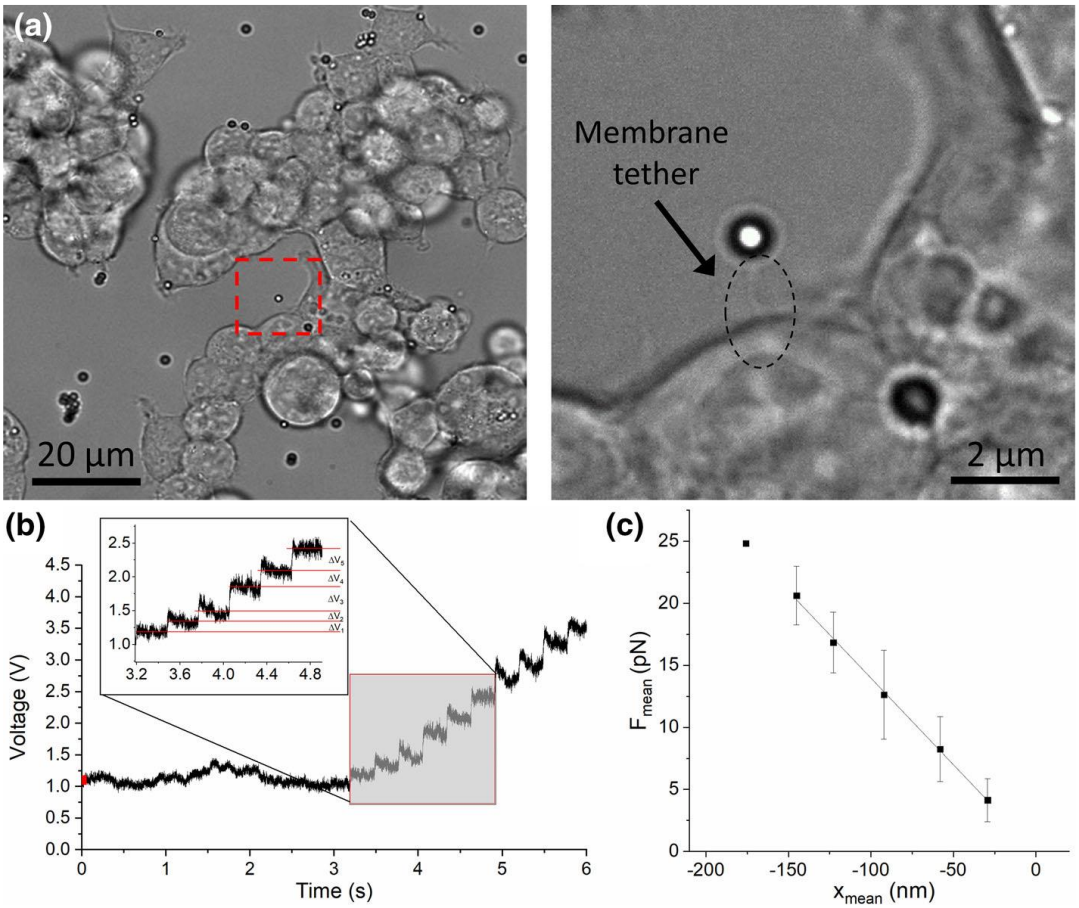


***Figure 2.4| Cell membrane manipulation experiment. (a)*** *Contact between the cell membrane a fibronectin-coated 1.2-µm polystyrene bead driven by optical tweezers. The bead is then pulled away from the cell creating a membrane tether while applying force to the membrane.* ***(b)*** *Voltage signals recorded by the QPD during stepwise motion of the trap, beam power 28 mW. The bead follows the movement of the trap with some delay.* ***(c)*** *Linear dependence between the mean force and the mean bead displacement. Tether stiffness was found to be* $k_{teth} = 0.139 \pm 0.001\ pN/nm$ *in this case.*

## 2.2 Fluorescence microscopy implementation

### 2.2.1 Excitation and detection of fluorescence

The fluorescence microscopy part of the experimental setup consists of five excitation semiconductor TEM00 laser sources (Fig. 2.5 (a)). From right to left, an OBIS 445LX laser at 448 nm, with a maximum output power $P_{max} = 75\,mW$ and a collimated beam waist $\omega = (0.6 \pm 0.1)mm$, an OBIS 488LX at 488 nm, with $P_{max} = 150\,mW$ and $\omega = (0.7 \pm 0.1)mm$, and OBIS 514LX at 518 nm, with $P_{max} = 40\,mW$ and $\omega = (0.6 \pm 0.1)mm$, an OBIS 552LS at 552 nm, with $P_{max} = 150\,mW$ and $\omega = (0.70 \pm 0.05)mm$, and finally an OBIS 640LX laser at 643 nm with $P_{max} = 110\,mW$ and $\omega = (0.8 \pm 0.1)mm$. Telescope systems are placed after each laser source output to enlarge the laser beam to a common size of roughly 4 mm. Their spatial profile is optimized through a pinhole placed in the focal plane between the two lenses of the telescope. Narrow band-pass filters (Semrock FF01-445/20-25, FF01-488/6-20, FF01-513/13-25, FF01-542/27-25 and FF01-640/14, respectively) are placed at the diode laser outputs to eliminate undesired wavelengths that could be present due to the spurious emission outside the emission bandwidth. Each beam is directed to the microscope by dichroic mirrors (Semrock Di02-R442, LM01-503-25, Di02-R514 and Chroma ZT568rdc) allowing for the consecutive excitation of samples by the different wavelengths. Two achromatic telescope systems are inserted to allow for full field ($200\,\mu m \times 200\,\mu m$) excitation at low powers, which is suitable for cell imaging. The second telescope system is mounted on flip mounts in order to have the possibility of half-field at 4X power when removed, which is optimal in the case of single molecule imaging. An additional achromatic lens focuses the excitation beam into the back aperture of the objective lens, providing constant intensity illumination since the focussing lens and the objective are in a telescope configuration. Moreover, an iris is placed in the back focal plane of the focussing lens and, thus, is conjugated to the objective's focal plane to spatially limit the excitation beam and regulate the illumination area. By placing a mirror before the focusing lens, and the focussing lens itself on motorized translators, it is possible to translate the excitation beam at the entrance of the objective to switch between different illumination schemes such as wide field, HILO and TIRF.

The Nikon microscope contains a microscope wheel that accommodates several dichroic mirrors (DM5 in Fig. 2.5 (a)) (e.g., Chroma ZT440/488/561/635rpc-uf2, Chroma ZT488/561rpc-uf2 and Chroma ZT440/514/561/640rpc-uf1) which reflect the excitation beams to the objective and transmit the emitted fluorescence to the

detection system. This allows to image samples characterized by the presence of a combination of fluorophores with different excitation wavelengths.

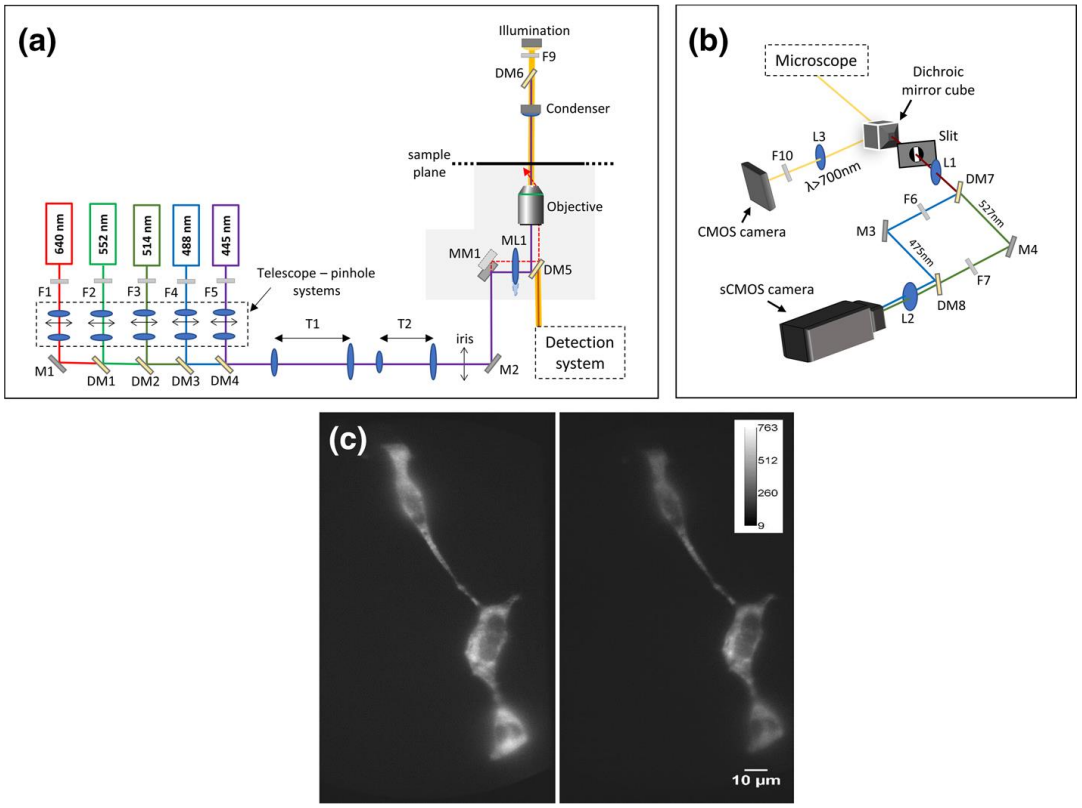


***Figure 2.5| Schematic of the fluorescence microscopy part of the experimental apparatus. (a)*** *Fluorescence excitation part consists of five laser sources. After each laser narrow band filters F1-F5 are placed to eliminate undesired spurious wavelengths. Telescope and pinhole systems are also positioned to enlarge the excitation beams to a common size and optimize their spatial profile. By using dichroic mirrors DM1-DM4, the excitation beams are directed to the microscope after passing through two telescope systems (T1 and T2) which allow for different fields of excitation. The mirror MM1 and the focussing lens ML1 are mounted on motorized mounts, providing the possibility to switch between different illumination schemes (wide field, HILO and TIRF). The dichroic mirror DM5 can be selected by rotating the microscope wheel to match the excitation and emission wavelengths desired. The filter F9 is used to allow wavelengths longer than 700 nm to reach the sample, providing the possibility for bright-field imaging.* ***(b)*** *The detection part of the system allows for simultaneous imaging of bright-field and fluorescence emission. The light coming from the microscope is divided into two parts by a dichroic mirror cube: wavelengths longer than 700 nm are reflected on a CMOS camera for bright-field imaging, whereas shorter wavelengths pass through a slit that splits the fluorescence image in two parts. The dichroic mirror DM7 transmits wavelengths longer that 506 nm and reflects shorter ones. The two parts are then recombined by a dichroic mirror DM8 identical to DM7 and focused on the sCMOS camera side by side by the achromatic doublet telescope system consisting of lenses L1 and L2. Emission filters F6 and F7 are placed in each arm to filter out undesired wavelengths.* ***(c)*** *Live HEK cells transfected by the cpstFRET sensor (Par. 1.3.4.2) and imaged in two emission channels simultaneously. On the left, the "donor" channel is shown corresponding to 479 emission and on the right the "acceptor" channel corresponding to 542 emission.*

The detection apparatus is able to image two emission channels of the fluorophores on a single sCMOS camera (Hamamatsu Orca-Flash4.0 V2), as shown in Fig. 2.5 (b). This is particularly beneficial for the realization of FRET experiments since it is essential to display the emission from both donor and acceptor fluorophores (Fig. 2.5 (c)). Simultaneous bright-field imaging is achieved by a CMOS camera (Thorlabs DCC1545M), allowing for combined trapping and fluorescence experiments. In order to achieve this, the halogen lamp light is filtered with a long-pass filter (Thorlabs FEL0700) to allow the transmission of wavelengths longer than 700 nm and minimize interference with fluorescence microscopy. The light exiting the microscope arrives to a dichroic mirror (Chroma ZT775sp-2p), which is transparent to wavelengths shorter than 730 nm and reflective for longer wavelengths. The reflected light is focussed on the CMOS camera after passing through a notch filter (Thorlabs NF808-34) to block the optical tweezers beam. The transmitted light passes through the centre of a slit positioned on the image plane produced by the microscope tube lens. This is done in order to divide the image into two identical halves centred side by side on the sCMOS camera chip. After the slit, a telescope system consisting of two achromatic doublet lenses with the same focal length is inserted. The first lens is placed at a distance from the slit equal to its focal length, while the second one is placed at the same distance from the sCMOS camera. A dichroic mirror (Semrock FF506-Di03) reflects wavelengths shorter than 506 nm, thus giving the possibility to divide the emission optical path into two different wavelength groups. The two new beam components are ensured to cover the same distance. Finally, the two beams are recombined by a dichroic mirror identical to the one splitting them and are then focussed on the sCMOS chip side by side by the second achromatic doublet. The choice of achromatic doublets was made to reduce chromatic aberrations and focus different wavelength rays at the same point. Two additional emission filters (e.g., Semrock, FF01-479/40 and FF01-542/27 for FRET experiments) are introduced in each path to narrow the transmitted wavelengths around the peak value of the desired emission spectra of the fluorophores used in experiments. Furthermore, the two dichroic mirrors are mounted on flip mounts to easily switch to a single image detection scheme, also thanks to the possibility to enlarge the slit with a micrometre screw. This detection system was later substituted with the Hamamatsu W-VIEW GEMINI A12801-01 image splitter, which provides the same simultaneous image acquisition of dual wavelength images with better precision.

Fig. 2.5 shows a detailed schematic of the fluorescence microscopy part of the apparatus as well as the simultaneous acquisition of the “donor” and “acceptor” image channels in a sample containing human embryonic kidney (HEK) cells which were transfected with an actin FRET force sensor (cpstFRET).

### 2.2.2 Characterization of localization accuracy through FIONA

Fluorescence excitation of organic chromophores and fluorescent proteins can be obtained by using total internal reflection fluorescence (TIRF) to follow processes occurring near the cell membrane, or by using an optimized highly inclined and laminated optical (HILO) sheet to image intracellular events with high signal-to-noise ratio. In order to follow mechanotransduction events at the molecular scale, the sensitivity of the apparatus must be sufficient to detect single chromophores and localize them with few nanometres resolution. To establish the sensitivity and resolution of our setup, detection and localization of single chromophores were performed to accurately derive the coordinates of each dye in the sample plane. The localization of single fluorescent molecules is determined by fitting the point spread function (PFS) with a bidimensional Gaussian function [78] centred at $(x_0, y_0)$:

$$I(x,y) = b + I_0 exp\left\{-\frac{1}{2s^2}[(x-x_0)^2 + (y-y_0)^2]\right\} \quad (2.6)$$

where $b$ is the background intensity, $s$ is the standard deviation of the bidimensional Gaussian function, and $I_0$ is the peak intensity.

The localization uncertainty can be reduced by increasing the number of collected photons and by minimizing noise factors [78]. Single molecule localization experiments were performed by using Alexa Fluor 568 and Alexa Fluor 647 dyes, with absorption and emission maxima at 578 nm and 603 nm, and at 650 and 665 nm, respectively. Samples were prepared using flow chambers made as depicted in Fig. 2.6 (a). A microscope slide and a 18 $mm$ × 18 $mm$ glass coverslip (170 μm thickness) was cleaned with pure ethanol and then dried under nitrogen flow. Two flow chambers were created by attaching three stripes of double-stick tape to the slide surface and fixing the coverslip to the tape. Each chamber measured ~15 $\mu L$ of volume. 20 $\mu L$ of biotin-conjugated bovine serum albumin (bio-BSA) 1 $mg/mL$ was flowed in each chamber and incubated for 5 minutes. Next, the chambers were washed with 60 $\mu L$ of phosphate buffer (PB) 50 mM. Subsequently, 20 $\mu L$ of the two streptavidin-conjugated alexa fluor dyes was separately flowed in the two chambers and incubated for 3 minutes. The concentration chosen for Streptavidin-Alexa Fluor 647 was 0.2 $ng/mL$, and for Streptavidin-Alexa Fluor 568, 0.7 $ng/mL$, to obtain separated single emitters attached to the coverslip surface. Finally, the chambers were washed with 100 $\mu L$ of imaging buffer (928 $\mu L$ PB, 10 $\mu L$ DDT 1 $M$, 40 $\mu L$ glucose oxidase 5 mg/mL, 12 $\mu L$ glucose 250 ng/mL). Careful wash is essential in preventing the presence of background fluorescent molecules during the imaging process, while the

oxygen scavenger enzymes in the imaging buffer assure reduced oxygen levels in the sample to minimize blinking and photobleaching phenomena.

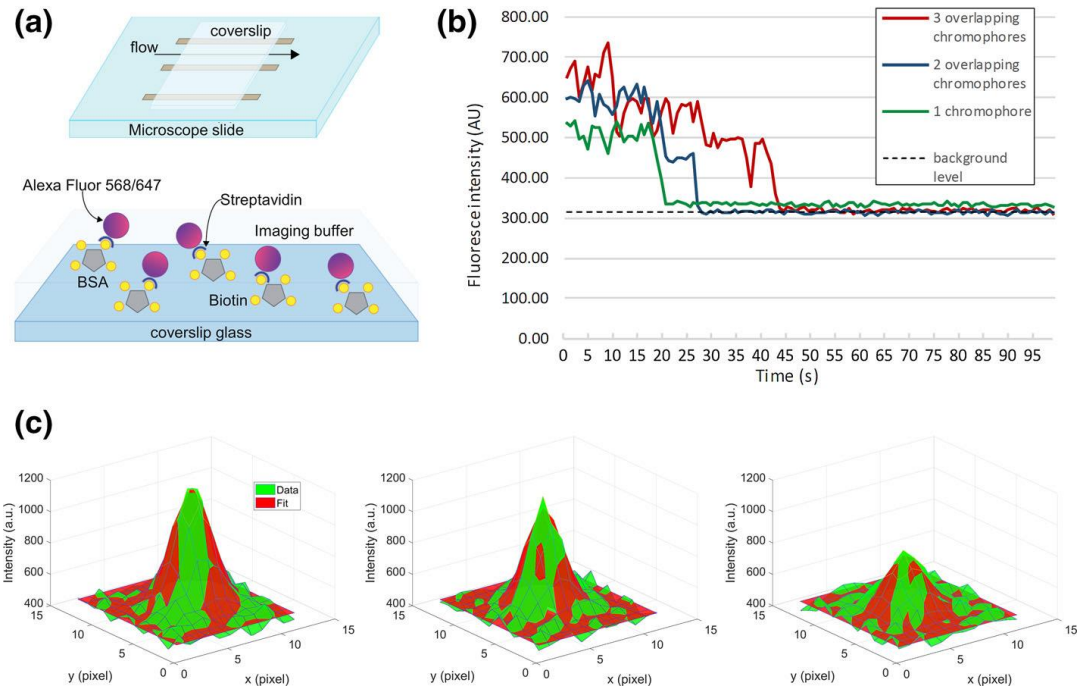


***Figure 2.6| Single molecule localization experiment to characterize the setup localization accuracy. (a)*** *Top: Flow chamber. Bottom: streptavidin-Alexa Fluor molecules specifically bound to the coverslip through biotinylated BSA.* ***(b)*** *Emission intensity dropping in step-like fashion implying that the source of emission consisted of clusters of multiple dyes, each one photobleaching in time.* ***(c)*** *Time evolution of FIONA algorithm tracking of single chromophores. The green colour represents the recorded data, while red is the Gaussian fit providing the centre of mass coordinates. The intensity drops observed between frames are due to the photobleaching of one dye.*

The sCMOS camera was set to acquire 200 frames with 500 ms integration time. The acquisition of data was performed in all the three illumination configurations possible: wide field, HILO and TIRF. The intensity of the excitation beam on the sample plane was set to $I = 100\ W/cm^2$. HILO and TIRF are high signal-to-noise ratio fluorescence microscopy techniques, owing to the reduction in background noise coming from out-of-focus fluorescence [79]. These illumination schemes produce higher intensity if compared with wide field microscopy: TIRF microscopy, which occurs when the incident angle $\theta_i$ equals the critical angle for total internal reflection, results in $I_{TIRF} = 4I = 400\ W/cm^2$, which was comparable to the intensities produced by HILO microscopy.

The temporal evolution of fluorescence emission was studied to ensure that the localization analysis was conducted on single chromophores: in some cases, emission intensity decreased in a step-like fashion with time, implying that the source of emission was an agglomerate of dyes and not a single molecule (Fig. 2.6 (b)). Each step in the intensity corresponds most likely to the photobleaching of one of the chromophores belonging to these agglomerates. Furthermore, in these situations quenching and blinking effects originating from the interaction between chromophores of the same group resulted in irregular intensity profiles. Parts of the collected data which contained these dye groups were not considered for localization analysis. Moreover, the absolute position of each dye had to be corrected because of the presence of thermal drifts. For these reasons, we used as a reference the coordinates $(x_{ref}, y_{ref})$ of a single chromophore in the field of view which emitted at a constant average intensity during all frames and calculated the position of the other dyes as the relative position $(x^r = x - x_{ref}, y^r = y - y_{ref})$. We then evaluated the localization accuracy for each chromophore as the standard deviation of its relative position. The mean localization accuracy for all the Alexa Fluor 647 chromophores analysed was evaluated to be $\bar{s}_x = (8 \pm 3)\, nm$ and $\bar{s}_y = (8 \pm 2)\, nm$ for wide field microscopy, and $\bar{s}_x = (7 \pm 2)\, nm$ and $\bar{s}_y = (7 \pm 2)\, nm$ for both HILO and TIRF microscopy. For Alexa Fluor 568 were found $\bar{s}_x = (15 \pm 7)\, nm$ and $\bar{s}_y = (15 \pm 7)\, nm$, $\bar{s}_x = (12 \pm 3)\, nm$ and $\bar{s}_y = (12 \pm 6)\, nm$, and $\bar{s}_x = (10 \pm 4)\, nm$ and $\bar{s}_y = (10 \pm 3)\, nm$ for wide field, HILO and TIRF microscopy, respectively. The errors given here are standard deviations from the average value.

# 3 Methods and procedures

## 3.1 Scaling and cross-correlation of the acquired images

As described above, when performing FRET experiments, we obtain a final image constituted by two identical images simultaneously displayed on each half of the sCMOS detector: the 'donor' channel and the 'acceptor' channel. After the implementation of the detection part of the experimental apparatus, it was necessary to check if the fields of view of the two channels were perfectly aligned and characterized by the same magnification, as well as if there was distortion at the image borders. To this end, a sample of mixed pollen grains was used. From fluorescence images obtained from this sample, we could clearly observe that one of the two fields of view presented a higher magnification. As a first step, we tried to directly solve this problem by manually adjusting the optics' positions on the setup. These efforts were insufficient to solve the problem: thus, we concluded that, even though we used achromatic doublets in the detection part, residual chromatic aberrations were not negligible. Therefore, we decided to perform post-processing correction on the acquired images by writing a custom MATLAB program.

The program allows the selection of an image taken when the excitation wavelength is the one of the donor molecules (445 nm), which displays fluorescence in both channels (e.g., direct emission of the donor fluorophores in the donor channel and FRET induced emission of the acceptor fluorophores in the acceptor channel). Then, the program asks for the selection of the correspondent image taken when the excitation wavelength is the one of the acceptor molecules, which only shows fluorescence intensity in one channel (e.g., direct emission of the acceptor fluorophores in the acceptor channel). After the selection of these two images, the program asks to draw a selection in the image corresponding to the donor channel. The selected region is the one that the program will use to perform the correlation process. To this end, it is convenient to take as selected region a cell or a cell part that shows high S/N ratio, so that cross-correlation can be performed with higher precision.

After the selection of the region of interest, the cross-correlation of images starts through the MATLAB specific algorithm called "xcorr2" (2D cross-correlation). This function returns the cross-correlation of two images matrices A (donor channel) and B (acceptor channel) with no scaling: this is done to find the exact point where a section of the first image is superimposed onto the same section in the second image, in order to find the regions where the two signals are identical. The fact of performing this process only on a limited section of the image allows the algorithm to calculate more rapidly the cross-correlation function, since it operates on a restricted number

of pixels without working on the whole image. Furthermore, the program allows scaling the two images to readjust the dimensions of each channel by using the bright-field image as a reference. Finally, as a result, the script automatically builds an image stack composed of three channels aligned (Fig. 3.1) [5].

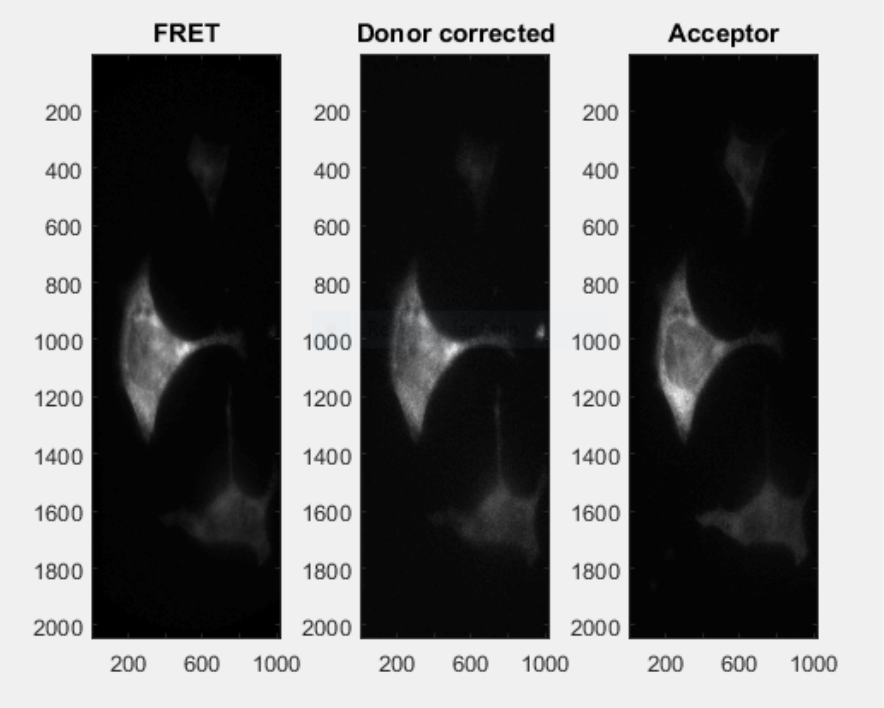


***Figure 3.1| Example of the final image obtained after complete algorithm operation.*** *The figure shows an example of the fluorescence image displayed after running the MATLAB program we wrote. The "donor corrected" image (middle) is the image corrected by the algorithm, which first readjusts its dimensions with respect to the other channel and then performs a 2D-cross-correlation operation between the two of them.*

The image obtained (Fig. 3.1) is automatically saved in the original folder in the form of a stack of three images. All the images acquired in this work and used to calculate FRET efficiency have been processed through this MATLAB program.

## 3.2 Calculation of FRET efficiency through the PixFRET plugin

As mentioned in the first chapter (Par. 1.3.3), a large number of methods to calculate FRET efficiency exist. Usually, the simplest solution consists in using a FRET index, which can be defined in many ways as well. Comparison of the FRET index values obtained from force sensors in different experiments is sufficient to determine changes in tension. If a more quantitative measurement of the FRET efficiency is needed, a good solution consists in performing a calibration of the FRET index through standard FRET constructs with known FRET efficiency values.

When performing fluorescence microscopy experiments, there are a lot of factors to be considered for a correct FRET efficiency calculation. First of all, an evaluation of the background fluorescence level is needed, so to exclude it from FRET signal. Then, another important factor to consider is the fluorophores' photobleaching: when a region of the sample is excited by a laser beam, a fraction of the fluorophores in that region are somehow "burnt" by the beam and, thus, their emission decreases proportionally. Finally, another crucial factor to keep in mind when performing FRET experiments is the phenomenon of the spectral bleed through (SBT), which is the fluorescence emission revealed in the FRET channel that is not due to resonance energy transfer. The principal causes of SBTs are (i) the emission of the donor molecule that overlaps with the spectrum detected in the acceptor channel and (ii) the indirect excitation of the acceptor molecule by the excitation laser of the donor [80]. Both contributions must be considered to avoid artifacts in FRET efficiency calculation.

Among the large number of programs and algorithms available to calculate FRET efficiency or indexes, we decided to use a publicly available ImageJ plug-in called PixFRET [80]. A convenient feature of this plug-in comes from its ability to perform SBTs modelling. In the past, it was thought that SBTs were not dependent from emission intensity, and that they were constant factors. However, it has been observed that SBT values can notably vary according to the intensity of the fluorophore fluorescence emission. Therefore, this plug-in offers the possibility to describe the SBT factors as an increasing function of the fluorophore's intensity and in particular with a constant, linear, or exponential dependence (Fig. 3.2).

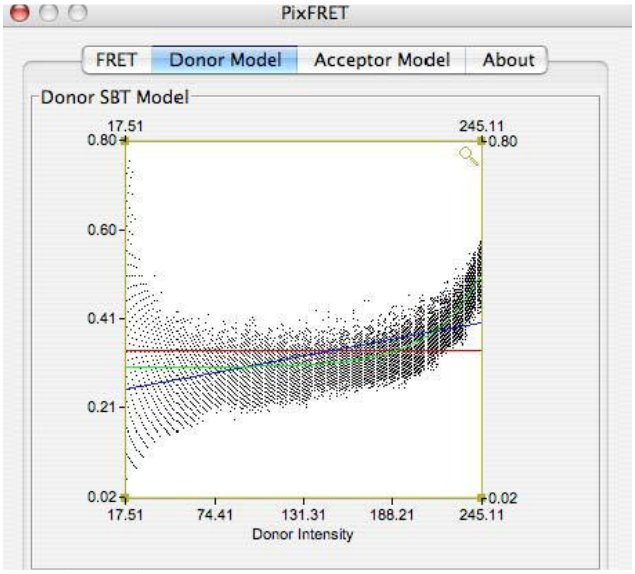


***Figure 3.2|Example of donor SBT modelling through the PixFRET plugin.*** *SBT ratios increase with fluorophore intensity in a manner that can be fitted with a constant value (red line), linear fit (blue line), or exponential fit (green line).*

The PixFRET plugin allows generating FRET images that are normalized with respect to the emission intensity of the donor and acceptor molecules. Different formulas can be chosen to calculate FRET indexes, the one we decided to use is the following:

$$NFRET = \frac{I_{DA} - aI_{AA} - dI_{DD}}{\sqrt{I_{DD} \times I_{AA}}} \times 100 \qquad (3.1)$$

where $I_{DA}$ is the fluorescence intensity obtained through excitation of the donor and measured in the acceptor channel, $I_{AA}$ is the intensity measured in the acceptor channel when excitation wavelength of the acceptor is used, and $I_{DD}$ is the intensity measured in the donor channel upon donor excitation. The parameters $a$ and $d$ are the spectral bleed-through ratios. In particular, $a$ is the emission of the donor in the acceptor channel, while $d$ is the excitation of the acceptor using the donor excitation wavelength. The result of this operation is a final image where a FRET index is calculated and displayed in each pixel with a colour map (Fig. 3.3).

When the program is launched an interface opens where it is possible to set all the parameters required for the calculation and the creation of the FRET image. Starting from the windows regarding the SBT models for the donor and the acceptor molecules, it is necessary to open the stack images of the samples expressing only the donor or the acceptor molecule. The user is asked to draw a region in an empty space

where no cells are present to determine the background value in each image of the stack. After that, one or more regions must be selected to allow the program to interpolate the SBTs as functions of the fluorophores' intensities, calculating the linear or exponential interpolation parameters. The program automatically executes the SBT fitting as a function of the fluorophore's intensity, suggesting to the user which of the three fitting functions (constant, linear, or exponential) is the best (Fig. 3.2). The program returns the fit coefficients, that are later used in the calculation of NFRET (Eq. 3.1). On the other hand, it is also possible to manually insert all the values, both of background and of spectral bleed-through.

Subsequently, the program asks to open the stack composed of three images (Fig. 3.1) acquired from the sample where both the donor and the acceptor are expressed. In the interface table dedicated to FRET calculation, the user must first determine the background by drawing a rectangular section in a region without cells, or by manually inserting it. Moreover, the plug-in offers the possibility to perform image filtering through a Gaussian blur: this filtering notably reduces noise, resulting in a better FRET image, at the expense of lower spatial resolution. Finally, the program allows the user to choose between different normalization methods for the calculation of NFRET. By clicking on "Compute FRET", PixFRET generates an image where the FRET index (Eq. 3.1) is calculated and displayed with a colour bar pixel per pixel. The FRET index is calculated only if the pixel values of each image are higher than a given threshold value, otherwise it is set as null value and the pixel is depicted in black. An example of the images of a stack acquired from a sample where both the donor and the acceptor are expressed, which has been subjected to the entire MATLAB and PixFRET analysis is shown in Fig. 3.3.

For the analysis of cells, we used ImageJ to identify the areas of interest above an intensity and area size threshold and we used the function "Analyse particles" on the NFRET image (Fig. 3,3, right panel). This function calculates the surface (cell) area, the mean value of FRET index of the cell, its standard deviation and standard error. In this way, we were able to obtain the mean FRET index values of all the cells that we imaged in the sample. After that, we performed a statistical analysis later discussed in detail.

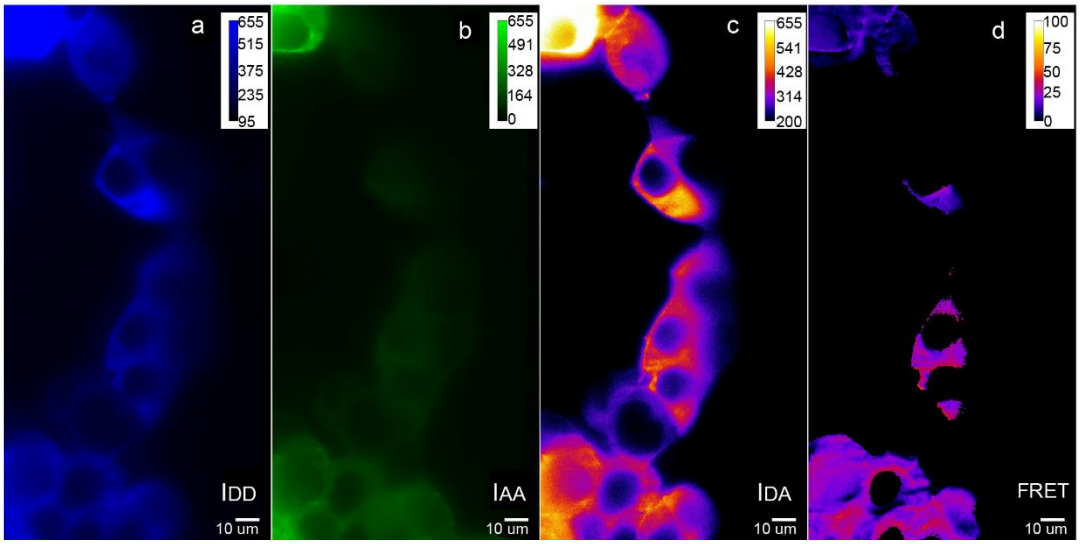


***Figure 3.3| Example of the resulting images after PixFRET plug-in processing.*** *A stack of three images is analysed through the PixFRET plug-in and the resulting images are shown here. The image shows HEK cells transfected with the c32V FRET standard (Par. 3.3). The program returns the images of the* ***(a)*** *donor channel (excitation with the 445 nm laser and emission in the range* $460\ nm < \lambda_{em} < 500\ nm$*),* ***(b)*** *the acceptor channel (excitation with the 514 nm laser and emission in the range* $530\ nm < \lambda_{em} < 560\ nm$*), and,* ***(c)*** *the FRET channel (excitation with the 445 nm laser and emission in the range of the acceptor channel). Panel* ***(d)*** *shows the NFRET image in which ratio metric FRET index is calculated pixel per pixel through Eq. 3.1 and displayed with a coloured map. The power of both lasers on the sample plane was 2.5 mW, 50 ms integration time.*

## 3.3 FRET index calibration

As we discussed previously (Par. 1.3.3), there is a large number of methods that can be used to measure FRET, and it is possible to choose a multitude of FRET indexes that relate to the actual definition of FRET efficiency. Since FRET efficiency is often undefined or subject to non-negligible systematic errors, it becomes very difficult to compare FRET measurements obtained with different methods and experimental setups. A possible solution to this problem comes from the existence of samples containing fluorescent proteins (FPs) pairs, which have been accurately characterized in terms of FRET efficiency: these constructs can be used as "standards" to validate and calibrate FRET in different imaging systems with high reproducibility [65].

We used three different models of standard constructs which are all characterized by a couple of fluorescent proteins (Cerulean and Venus) and show an increasing separation between them. The FRET efficiency in these constructs is well known from literature [65], where it has been measured with three different methods: lifetime fluorescence spectroscopy, acceptor sensitized emission (Par. 1.3.3) and spectral imaging. Since the values derived from these methods are in good agreement with each other, FRET efficiency value of each construct could be established with high confidence and, thus, these sensors have been used as reference standard constructs. We used these FRET standards to calibrate our FRET imaging system and relate out measurements of FRET index to the FRET efficiency values obtained by Koushik et al. [65].

In particular, the three sensors under exam are called C5V, C17V, and C32V, where letter C stands for "Cerulean" fluorophore (donor), letter V stands for "Venus" fluorophore (acceptor), and the number specifies how many amino acids are placed in the linker between the two dyes. Constructs with a shorter amino acidic linker are expected to show higher FRET efficiency. Therefore, we expected C5V to exhibit the highest efficiency, followed by C17V and C32V, respectively. The Cerulean fluorescent protein is excited by the 445 nm-wavelength laser and shows an emission peak at a wavelength of 475 nm, whereas Venus is excited by the 514 nm-wavelength laser and has the emission peak at a wavelength of 528 nm. Before performing FRET measurements on standard sensors, we took experiments on cells expressing only the donor or the acceptor molecule, so to determine the background level and the SBT value of the two channels required by the ImageJ PixFRET plugin for an accurate calculation of FRET indexes (Par. 3.2).

In these measurements presented here, C5V, C17V and C32V were transfected into HEK (Human Embryonic Kidney) cells, which were allowed to adhere on glass

coverslips (18 mm diameter) and then positioned on the microscope. Images were taken sequentially: first, by exciting the sample with the 445 nm-wavelength laser with a 50 ms exposure time to acquire the FRET and donor channels, and then, by illuminating with the 514 nm-wavelength laser with 50 ms exposure time to image the acceptor channel.

All the images acquired have been scaled and processed through the MATLAB program described in Par. 3.1 and then analysed with the PixFRET plugin described in Par. 3.2., through which we obtained data of the area (cell) dimension, its mean FRET index value, and its relative standard deviation and standard error. A simple average among the FRET index values of cells with the same construct was taken as result, with the respective standard error.

FRET indexes measured as described above are shown in Fig. 3.4 (a). The linear trend observed in both our measurements of FRET index (black lines) and the FRET efficiencies obtained in [65] (red lines) within the measured range, allowed for a calibration curve relating the measured FRET index with the calibrated FRET efficiency, for a better comparison with experiments performed with different methods (Fig. 3.4, b).

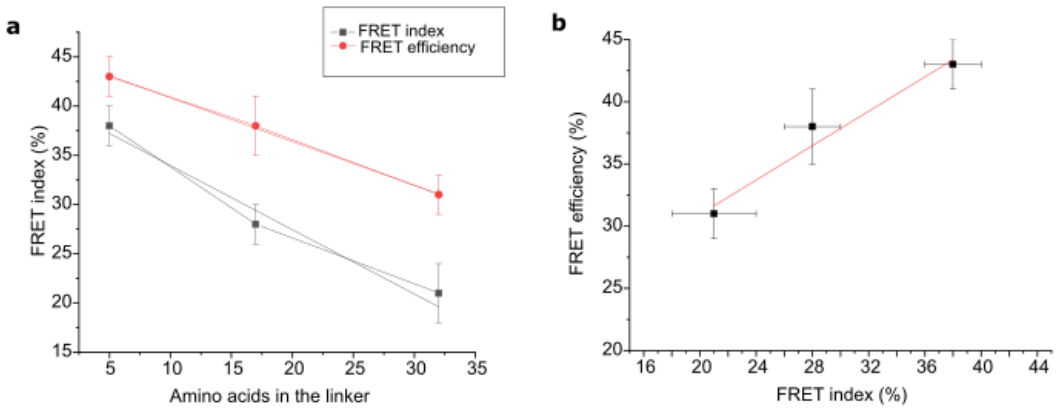


***Figure 3.4| Characterization of FRET standards. (a)*** *FRET index of C5V, C17V and C32V standards versus calibrated FRET efficiency (N=10 cells per construct). The linear fit of FRET index gives an adjusted R-square value of 0.9333.* ***(b)*** *Calibration curve to relate FRET index measurements with the calibrated FRET efficiency. The linear fit between FRET efficiency and FRET index gives a slope of* $0.7 \pm 0.2$ *and an intercept of* $17 \pm 6$ *with a Pearson's coefficient value of 0.98.*

## 3.4 Measuring tension on specific proteins with different FRET-force sensors

The transmission of mechanical tensions in the cell can be probed, as mentioned above, by using genetically encoded FRET-based force sensors. As we described in Par. 1.3.4.3, the DNA sequence coding for the force sensor module is inserted within the coding sequence of the protein of interest. The plasmid containing the protein fused with the sensor is then transfected in the cell for transient or stable expression. Force sensors for several proteins (such as actin [72], spectrin [66], alpha-actinin [66], alpha-catenin [81], nesprin [21] and vinculin [70]) and sensor modules based on different linkers have been developed [73], [82], allowing the measurement of different ranges of forces from few pN to several tens of pN per molecule. In the following paragraphs, I will describe the FRET-force sensors we used to probe mechanical tensions in specific proteins.

### 3.4.1 The actin sensor

In order to investigate the role of mechanical stresses on the actin cytoskeleton, Guo et al. developed a specific tension sensor that is inserted into F-actin [72]. The sensor module used in these experiments is based on the relative orientation of the donor-acceptor pair. This sensor is called cpstFRET (circularly permuted stress-sensitive FRET), and it was developed starting from the existing stFRET sensor [66]. cpstFRET is composed of five amino acids that link two circularly permuted fluorescent proteins, whose dipoles are parallel at zero force and are supposed to twist towards a perpendicular configuration under tension, decreasing FRET efficiency values. As a consequence, this sensor is much smaller than the ones based on linear springs [4].

The actin force sensor, named actin-cpstFRET-actin (AcpA), is shown in Fig. 3.5, and consists of the dipole orientation-based sensor cpstFRET flanked by two β-actin monomers, which polymerise with native G-actin and label F-actin efficiently. A zero-force control sensor called cpstFRET-actin (cpA) was also used, and it is shown in Fig. 3.5 as well. This sensor has only one actin monomer, leaving the other end of the probe free to move and not be subject to forces [72]. Both sensors were transfected into HEK cells and two cell lines that stably expressed them were selected from Kerafast Inc. For another set of experiments, we transiently transfected the two sensors into human induced pluripotent stem cells (hiPSCs) and hiPSC-derived cardiomyocytes (see Par. 4.2 and Appendix 6.2.2-6.2.3).

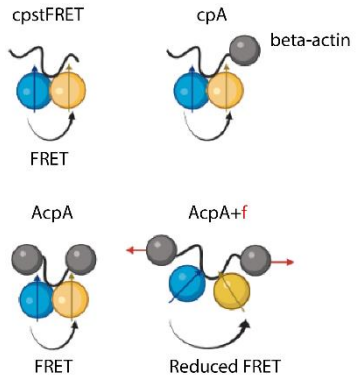


***Figure 3.5| The actin FRET sensor.*** *Sketch of the cpstFRET sensor and how it is inserted into F-actin. "cpA" is a cpstFRET- β-actin construct, where one actin monomer is bound to the C-terminal of the cpstFRET sensor. "AcpA" stands for "Actin-cpstFRET-Actin" and is a construct where to actin monomers are linked by the cpstFRET sensor. "f" represents an external force, which induces rotation of the emission dipoles of the FPs, thus resulting in lower FRET.*

### *3.4.2 The alpha-actinin sensor*

Another protein that has a key role in defining the structure and rearrangement of the cytoskeleton is α-actinin, a cross linking and bundling protein that constitutes the backbone of contractile actin bundles and stress fibres. Therefore, α-actinin is particularly interesting for investigating the tension induced by myosin contraction.

We used a force sensor for α-actinin, called Actinin-M-cpstFRET, in which the same cpstFRET cassette used in the actin force sensor is inserted between spectrin repeat domains 3 and 4 towards the middle of α-actinin [72]. On the other hand, the zero-force control, called Actinin-C-cpstFRET, is created by binding the cpstFRET construct to the C-terminal of α-actinin. A scheme of these two sensors is shown in Fig. 3.6. As in the case of the actin force sensor, the two α-actinin FRET sensors were transfected and stably expressed in HEK cells that we received from Kerafast Inc.

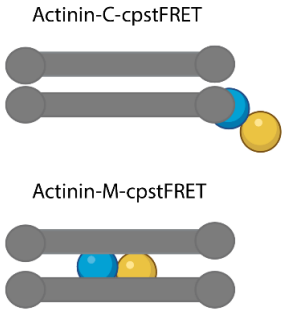


***Figure 3.6|The alpha-actinin FRET sensor.*** *A sketch of the two α-actinin sensors used. "Actinin-C-cpstFRET" is the zero force-control sensor, where cpstFRET is linked to the C-term of α-actinin. "Actinin-M-cpstFRET" is the force sensor, where cpstFRET is inserted in the middle of the α-actinin protein and is subjected to stress under tension.*

### 3.4.3 The nesprin sensor

The nucleus of a cell is connected with its cytoskeleton through a variety of nuclear membrane proteins known as nesprins, which are bound to F-actin, intermediate filaments, and microtubules. The nucleus is subject to mechanical forces that influence its shape and geometry, and, importantly, the arrangement of chromatin, and movement, but how these forces are transmitted from the cell cytoskeleton to the nuclear membrane is not well understood. In order to study how mechanical tensions are transmitted to the nucleus and might influence genic expression, we studied a specific FRET-based force sensor inserted into nesprin protein [21].

The sensor we used is called NesprinTS (Fig. 3.7) and consists of a linear-elastic spring in between a fluorescent protein FRET pair inserted in the middle of the coding sequence of the nesprin protein. Thus, it is a linear-based FRET sensor, differently from the ones used for actin and α-actinin, which are orientation-based. The sensor cassette is called "TSMod" and was previously developed by Grashoff et al. [70] for measuring forces in vinculin. The module consists of a 40-amino-acid-long elastic domain inserted between two fluorescent proteins (mTFP1 and Venus(A206K)) that undergo efficient FRET. The elastic domain was derived from the spider silk protein flagelliform, which is composed of repetitive amino-acid motifs that form entropic nano springs suitable for measuring piconewton forces. This module was inserted into nesprin by Arsenovic et al. [21]. The TSMod module was inserted between the XhoI and NotI sites of the mini-nesprin-2G linker, which consists of the mini-nesprin-2G sequence (mouse-derived), with an XhoI and NotI site linker between the actin-binding CH region and the SUN-binding domain (Par. 1.1.2).

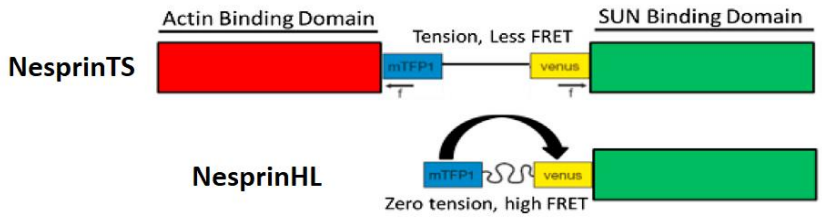


***Figure 3.7| The nesprin FRET sensor.*** *Schematic of nesprin-2G tension sensor and its headless control. "NesprinTS", is the force sensor, where TSMod is inserted in between the actin binding domain and the sun binding domain of the nesprin-2G sequence. "NesprinHL" is the zero-force control sensor, which lacks the actin binding domain. Image retrieved by* [21].

Both sensors were transfected into mesenchymal cells (MSCs) and were stably expressed by them (Par.4.3 and Appendix 6.2.4).

# 4 Results

## 4.1 Tension on actin and alpha-actinin increases with the stiffness of the substrate

As already mentioned in Par. 1.1.3, mechanotransduction processes usually involve force transmission through the cytoskeleton, which plays a central role in many aspects of cell life. Therefore, the fist proteins on which we decided to test FRET sensors where proteins of the cytoskeleton, and in particular actin and α-actinin, in order to study the transmission of mechanical tensions through the cytoskeleton of cells.

In this paragraph I will show the results we obtained from measurement on cells incorporating the FRET sensors for actin and alpha-actinin. The initial step was to compare the force sensor with the control sensor, which should be unaffected by mechanical forces. In this way we could assess that our system was correctly working and that there was a significative difference between the FRET index of the sensor and the zero-force control, also quantifying the dynamic range of each sensor. After that, we grew cells on substrates characterized by different stiffnesses (Par. 1.2.2), to see how the cytoskeleton responds to the mechanical properties of the environment.

### 4.1.1 Characterization of the actin-FRET sensor in cells adhered to a glass coverslip

First, the FRET efficiency of the actin sensors (both the force sensor and the control) transfected into HEK cells and grown on bare microscope glass coverslips were evaluated. All measurements were taken using the protocols and the experimental parameters described in Par. 6.2.1. Subsequently, data were analysed using the MATLAB script and the PixFRET plug-in (Par. 3.1 and 3.2), which resulted in images like the one showed in Fig. 4.1. From these images, the mean values of normalized FRET indexes (Eq. 3.1) were obtained along with their standard errors. As expected, a high FRET index of $(89 \pm 1)\%$ for the force-free actin sensor (cpA) was obtained, while this value decreased to $(58 \pm 1)\%$ for the force-sensitive actin sensor (AcpA) (Fig. 4.2).

Next, cells with actin sensors were grown on microscope glass slides covered with polylysine, which facilitates cell adhesion, and fibronectin, which stimulates focal adhesion (FA) formation and possibly stimulated higher mechanical tension on the actin cytoskeleton (Par 1.1.1).

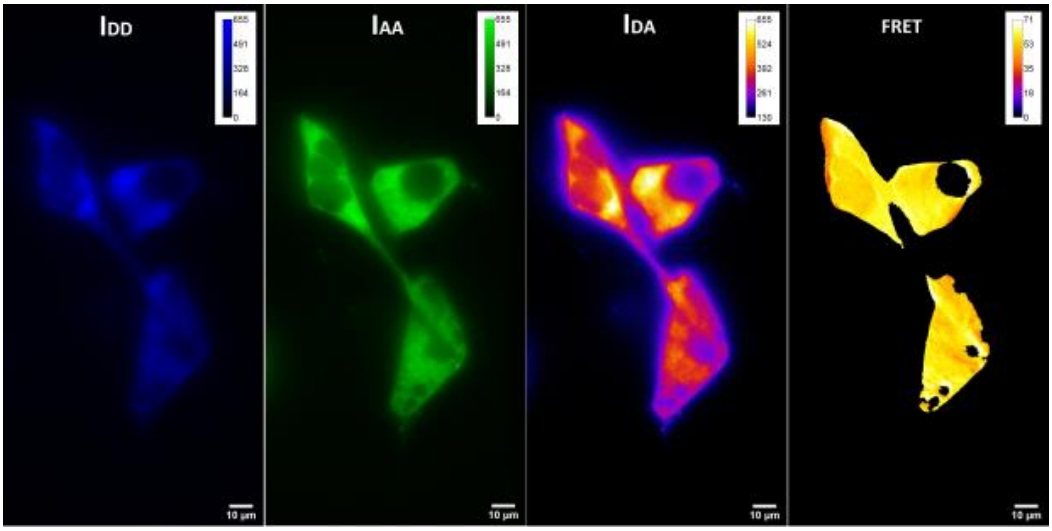


***Figure 4.1| Example of a HEK cell transfected with the AcpA sensor.*** *Images were taken in the three channels with an integration time of 50 ms, and the power of both lasers at the sample plane was 8 mW. The sample was illuminated in wide-field configuration. The last image on the right is the FRET index image calculated by the PixFRET plugin (Par. 3.2).*

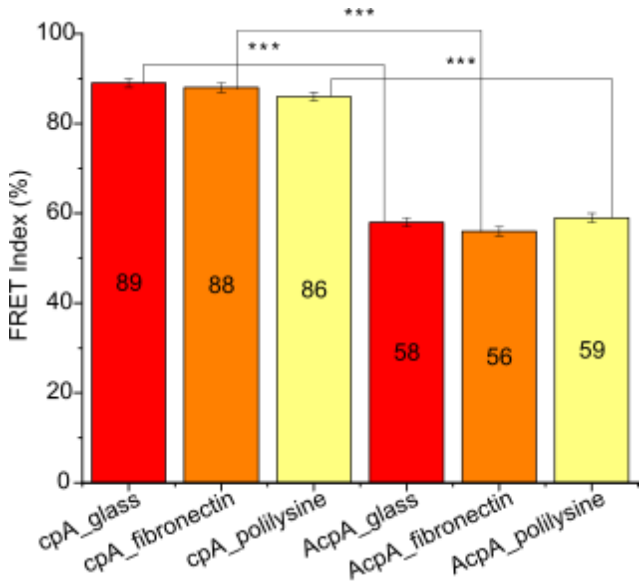


***Figure 4.2|Comparison of FRET indexes of cpA and AcpA in HEK cells.*** *FRET indexes of cpA and AcpA in HEK cells grown on glass slides (red), glass slides covered with fibronectin (orange) and glass slides covered with polylysine (yellow). All the force-free cpA sensors have significantly higher indexes compared to the AcpA sensor. According to a two-sample t-test, FRET index of AcpA on glass (N = 20) is not significantly different from FRET indexes of AcpA grown on fibronectin (N = 23, p = 0.43) and polylysine (N = 20, p = 0.79).*

The results, which are shown in Fig. 4.2, revealed that there was no significant difference between the actin sensors grown on different biochemical substrates. A possible explanation derives from the fact that in these series of measurements, we did not specifically image the glass-cell interface where FAs form, but, instead, the FRET signal came also from regions located deeper inside the cell. Thus, the measured FRET signal originated from parts of the cytoskeleton that were possibly not significantly influenced or involved in focal adhesions.

### *4.1.2 Actin tension in cells grown on hydrogels with different stiffnesses changes with substrate's rigidity*

After the characterization of cpA and AcpA sensors, which was performed on HEK cells grown on bare glass coverslips, we wanted to test whether growing cells on hydrogels of different stiffnesses could lead to a change in FRET index values, indicating that the stiffness of the substrate has an effect on the mechanical stress acting on the cell cytoskeleton.As previously mentioned in Par. 1.2.2, in fact, by modifying the stiffness of the substrate the mechanical forces applied on cell's adhesions change, and we can hypothesize that this change in tension is also reflected on cell's cytoskeleton.

Cells were plated at around 15% confluency on top of Easy Coat™ Softslip hydrogels from Matrigen. We used hydrogels with three different rigidities: 0.2 kPa, 4.0 kPa and 50.0 kPa. These stiffnesses resembled the ones of characteristic tissues of the human body (Fig. 1.12), with 0.2 kPa close to the stiffness of blood cells and epithelial tissue, 4.0 kPa similar to the stiffness of pancreas and kidney, 50.0 kPa mimicking the stiffness of the muscle, whereas bare glass resembles the stiffness of bones. Samples were prepared as described in Appendix 6.2.1 and positioned in the Easy Inject chamber (Appendix 6.1). The illumination was performed in TIRF configuration with the experimental parameters listed in Appendix 6.2.1.

The results obtained are shown in Fig. 4.3 and Tab. I: with 0.05 confidence level, results indicated that there was a relevant difference between the actin sensors grown on different rigidity substrates, whereas zero-force control sensors were not statistically different, as expected. Moreover, we observed that the FRET index value of AcpA sensors decreased as the stiffness of the substrate increased, showing that a stiffer substrate determined higher forces on the cell actin cytoskeleton.

| Sensor + Substrate | FRET index value (%) | Standard Error (%) |
|---|---|---|
| cpA + glass | 89.3 | 0.2 |
| cpA + 50 kPa hydrogel | 84.7 | 0.3 |
| cpA + 4 kPa hydrogel | 85.7 | 0.3 |
| cpA + 0.2 kPa hydrogel | 85.2 | 0.3 |
| AcpA + glass | 33 | 1 |
| AcpA + 50 kPa hydrogel | 43 | 2 |
| AcpA + 4 kPa hydrogel | 47 | 1 |
| AcpA + 0.2 kPa hydrogel | 53.2 | 0.9 |

***Tab I** | FRET index values of actin sensors grown on substrates of different stiffness.*

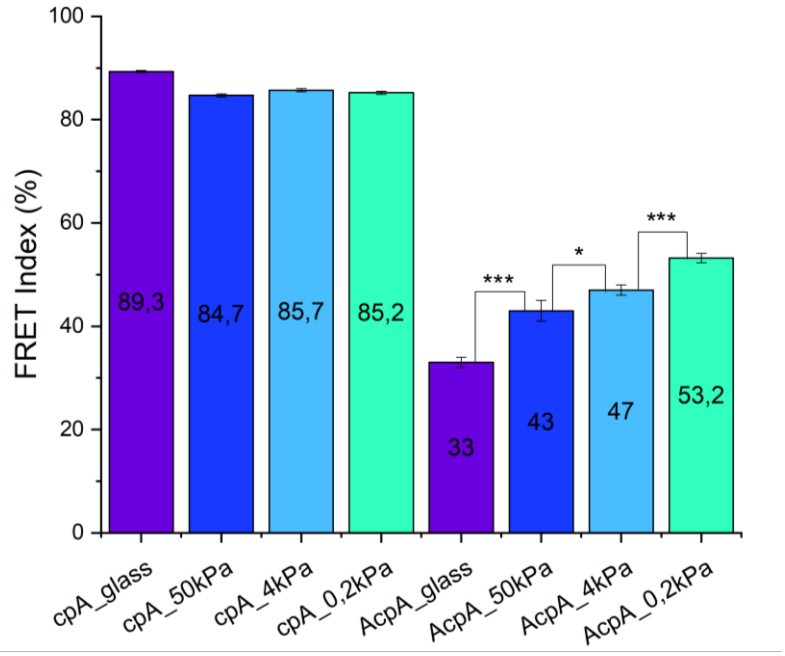


***Figure 4.3| FRET index values of actin sensors grown on substrates of different stiffness.*** *FRET indexes of cpA and AcpA in HEK cells grown on glass slides (violet), 50.0 kPa hydrogels (blue), 4.0 kPa hydrogels (light blue), and 0.2 kPa (light green). All the force-free cpA sensors have significantly higher indexes compared to the AcpA sensors. Data on AcpA sensors were confronted for each stiffness, showing that there is always a significant statistical difference: $p = 5x10^{-5}$ between cells on 0.2 kPa hydrogels (N = 87) and cells on 4 kPa hydrogels (N = 77); p = 0.03 between cells on 4.0 kPa hydrogels (N = 77) and cells on 50.0 kPa hydrogels (N = 39); $p = 2x10^{-4}$ between cells on 50.0 kPa hydrogels (N = 39) and cells on bare glass (N = 56).*

### *4.1.3 Characterization of the alpha-actinin-FRET sensor in cells adhered to a glass coverslip*

Alpha-actinin is a cross-linking protein that has a fundamental role in the maintenance and regulation of contractile actin bundles and stress fibres. For this reason, to better investigate how mechanical forces act on different parts of the cytoskeleton, we performed experiments on the α-actinin force sensor (Par. 3.4.2). The FRET efficiency of the α-actinin sensor (both the one subject to force and the zero-force control) transfected into HEK cells grown on bare microscope glass coverslips was initially evaluated by TIRF microscopy. All measurements were taken using the protocols and the experimental parameters described in Appendix 6.2.1. Consequently, data were analysed using the MATLAB script and the PixFRET plug-in (Par. 3.1 and 3.2), which generated images similar to the ones showed in (Fig. 4.4, (a)). From these images, the mean values of normalized FRET indexes (Eq. 3.1) were obtained along with their standard errors. With 0.05 confidence level, there was no significant difference between the sensor under tension and the force-free control ($p > 0.05$) from the standard statistical two-sample t-test (Fig. 4.4, (b)). However, through a more careful observation of the images acquired (Fig. 4.4, (a)), we could notice that the actinin fluorescence was mostly localized along cell-cell junctions.

For this reason, a new analysis was performed by selecting only the junctional areas as the region of interest. All the acquisition and processing of data was done in the same way as before, but instead of using the "Analyse particles" function of ImageJ on the final normalized FRET index image, we selected by hand the regions of cell-cell junctions, where fluorescence was predominantly localized, as shown in the right panel of Fig. 4.4a, where the yellow line underlies an example of the hand-made selection we drew.

As illustrated in Fig. 4.4 (b) (light blue), the difference between the zero-force control and the sensor resulted to be significant ($p < 0{,}05$) with a standard two-sample t-test. The FRET index of the Actinin-M-cpstFRET sensor is $(38 \pm 1)\%$, lower than the FRET index resulting from the Actinin-C-cpstFRET sensor ($(53 \pm 1)\%$), underlying that α-actinin is affected by tension near cell-cell junctions.

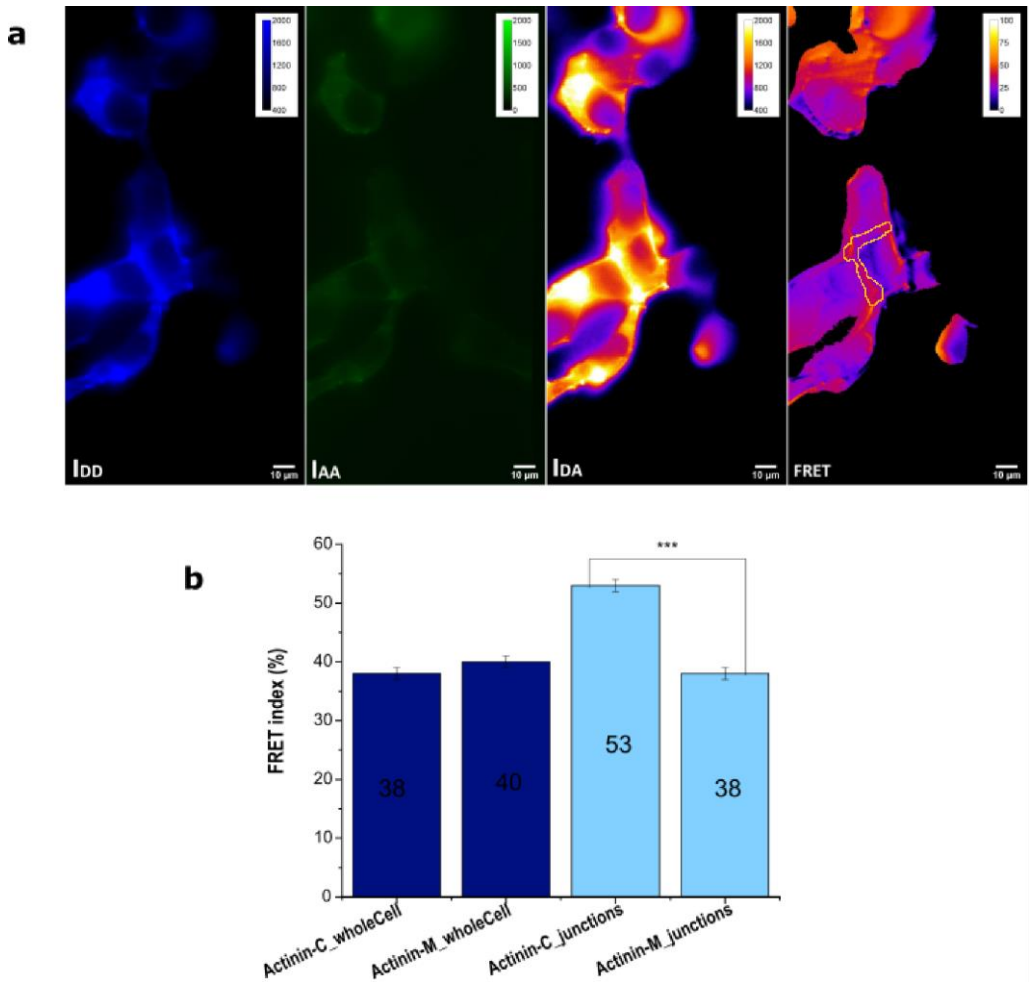


***Figure 4.4|FRET in HEK cells transfected with alpha-actinin sensor. (a)*** *Image of Actinin-M-cpstFRET sensor in HEK cells acquired through TIRF microscopy. Fluorescence emission is concentrated mainly along cell-cell junctions. Images were taken in the three channels with an integration time of 50 ms. Last image of panel (a) on the right is the FRET index image calculated by the PixFRET plug-in as described above.* ***(b)*** *FRET indexes of Actinin-C-cpstFRET and Actinin-M-cpstFRET grown on microscope glass slides and measured through TIRF microscopy in the whole cell (blue, N = 123 for Actinin-C-cpstFRET, N = 140 for Actinin-M-cpstFRET) and only along cell-cell junctions (light blue, N = 131 for Actinin-C-cpstFRET, N = 103 for Actinin-M-cpstFRET). Analysis of cell-cell junctions only reveals a significant difference between the zero-force sensor and the sensor subjected to tension (two-sample t-test,* $p < 0{,}05$*).*

### *4.1.4 Alpha-actinin tension in cells grown on hydrogels with different stiffnesses changes with substrates' rigidity*

As we previously made for HEK cells with the actin sensors, we decided to test FRET efficiencies of HEK cells grown on hydrogels of different stiffnesses containing the sensor for alpha-actinin. The stiffnesses chosen were the same used with the actin sensor (0.2 kPa, 4.0 kPa, and 50.0 kPa) and all the experimental parameters were the same as in the case of cpA and AcpA (Par. 4.1.2). Cells were plated again at around 15% confluency on top of Easy Coat™ Softslip hydrogels from Matrigen. The illumination was performed in TIRF configuration with the experimental parameters listed in Appendix 6.2.1. This analysis was performed by hand-selecting cell-cell junctions as regions of interest, as we previously made for cells grown on glass (Par. 4.1.3): in fact, as in the case of cells adhered to glass coverslips, we observed that alpha-actinin fluorescence was mostly localized in those regions.

The results obtained are summarized in Fig. 4.5 and Tab. II. Whereas zero-force control sensors didn't show the same behaviour as in the case of the actin sensors and showed less constant FRET index values, for the force-sensitive sensors we obtained the same trend observed for actin. In fact, with 0.05 confidence level, results indicated that there was a relevant statistical difference between the alpha-actinin sensors grown on different rigidity substrates. Moreover, we observed that the FRET index value of Actinin-M-cpstFRET sensors decreased as the stiffness of the substrate increased, as in the case of AcpA.

| Sensor + Substrate | FRET index value (%) | Standard Error (%) |
|---|---|---|
| Actinin-C + glass | 52.8 | 0.5 |
| Actinin-C + 50 kPa hydrogel | 57 | 1 |
| Actinin-C + 4 kPa hydrogel | 62.8 | 0.5 |
| Actinin-C + 0.2 kPa hydrogel | 63.7 | 0.4 |
| Actinin-M + glass | 38 | 1 |
| Actinin-M + 50 kPa hydrogel | 43 | 1 |
| Actinin-M + 4 kPa hydrogel | 47 | 1 |
| Actinin-M + 0.2 kPa hydrogel | 58 | 1 |

***Table II |*** *FRET index values of actinin sensors grown on substrates of different stiffness.*

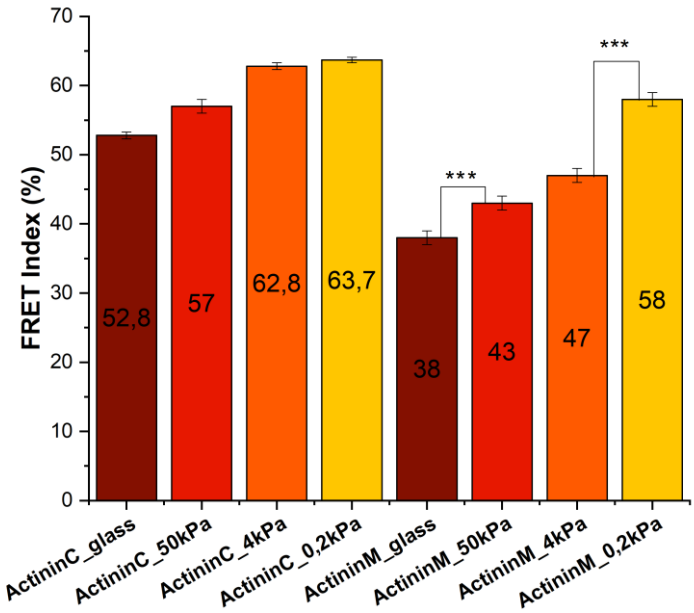


*Figure 4.5|* ***| FRET index values of alpha-actinin sensors grown on substrates of different stiffness.*** *FRET indexes of Actinin-C-cpstFRET and Actinin-M-cpstFRET in HEK cells grown on glass slides (dark red), 50.0 kPa hydrogels (red), 4.0 kPa hydrogels (orange), and 0.2 kPa (yellow). All the force-free Actinin-C-cpstFRET sensors have significantly higher indexes compared to the Actinin-M-cpstFRET sensors, even though they show a significant difference with each other which was not expected. Data on Actinin-M-cpstFRET sensors were confronted for each stiffness, showing that there is not a significant statistical difference (p = 0.10) between cells on 4.0 kPa hydrogels (N = 74) and cells on 50.0 kPa hydrogels (N = 76), whereas between the other rigidities there is always a relevant statistical difference: p = $1x10^{84}$ between cells on 0.2 kPa hydrogels (N = 79) and cells on 4.0 kPa hydrogels (N = 74); p = $3x10^{-4}$ between cells on 50.0 kPa hydrogels (N = 76) and cells on bare glass (N = 140).*

## 4.2 The role of forces on the actin cytoskeleton during differentiation of hiPS cells into cardiomyocytes

As we mentioned in the first chapter, mechanotransduction has a fundamental role in biological systems and is at the basis of many processes which are of great importance for cell's development, reprogramming and differentiation, for their correct behaviour and for the development of pathologies [83]. A study performed by Guo et al. [72] showed that stemness was associated with increased force in actin. They reprogrammed HEK-293 cells into stem-like cells by softening the substrate, and then replated them on glass, which led to redifferentiation and reduced force in actin, measured through FRET on the same sensor we used (AcpA).

We investigated the relationship between the cellular differentiation state and the tension on the actin cytoskeleton through an experiment in which we used the same sensor for actin that we used for HEK cells measurements (Par. 4.1.1-4.1.2), but different cells: human induced pluripotent stem cells (hiPSCs). These cells are artificially generated from a cell that is terminally differentiated, through a reprogramming protocol of de-differentiation. These cells represent a powerful tool for scientific research, since they allow us to study the cellular development and the differentiation mechanisms, avoiding ethic discussion linked to the usage of embryonic stem cells. Moreover, hiPSC cells can be used to generate cells to study human pathologies, simply by reprogramming adult cells, generally coming from patients with genetic diseases [84].

This project was conducted in collaboration with the Experimental and Clinical Medicine Department of the University of Florence with the research group of Dr. Corrado Poggesi. They managed to generate hiPSC-derived cardiomyocytes (hiPSC-CMs) from hiPS cells that were in turn collected from either urine [85] or skin fibroblast, using directed differentiation of high-density monolayers with a combination of activin A and BMP4. After 15-20 days post-differentiation, hiPSC-derived cardiomyocytes (hiPSC-CMs) were replated at low density onto fibronectin-coated nanopatterned surfaces with specific characteristics. This resulted in cells that were elongated and of dimensions similar to those found for cultured adult cardiomyocytes (Fig. 4.6) [86].

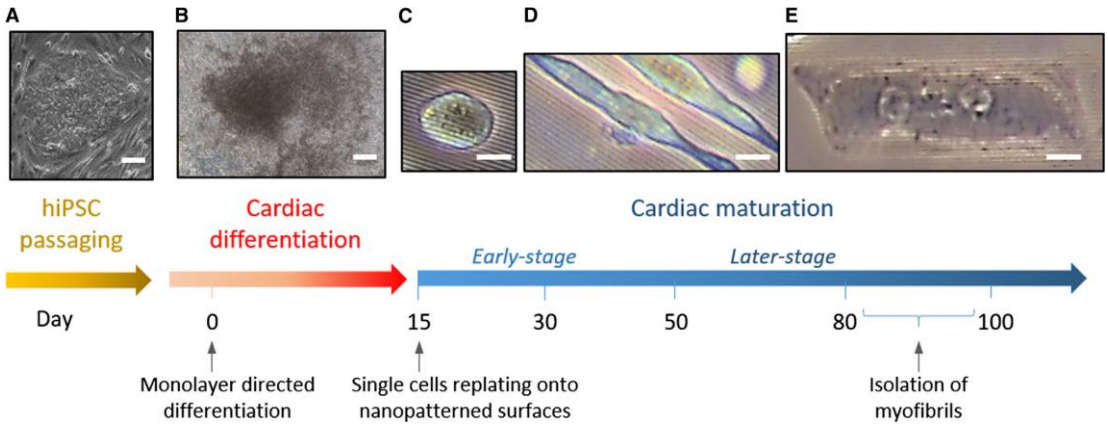


***Figure 4.6| Protocol for Cardiac Maturation of Human Pluripotent Stem Cells on Nanopatterned Surfaces in Long-Term Cultures. (A-E)*** *hiPSCs at different stages of differentiation and cardiac maturation.* ***(A)*** *hiPSCs passaging before differentiation.* ***(B)*** *At day 0, hiPSCs were differentiated into cardiomyocytes with a monolayer-differentiation protocol.* ***(C)*** *At day 15, single hiPSC-derived cardiomyocytes (hiPSC-CMs) were replated onto nanopatterned surfaces until day 80-100 in low density for cardiac maturation.* ***(D)*** *After replating, hiPSC-CMs showed early progressive elongation.* ***(E)*** *Later-stage hiPSC-CMs were rod-shaped. Image retrieved by* [86].

We wanted to test whether there was a measurable difference in FRET index values of hiPSCs in their initial stem state with respect to their index after differentiation into hiPSC-derived cardiomyocytes. The sensor we used is AcpA, and its zero-force control, cpA (Par. 3.4.1). We optimized a protocol to transfect hiPSCs and hiPSC-CMs with the actin FRET sensors (AcpA and cpA). The handling of the samples and the experimental parameters used are described in Appendix 6.2.2 (hiPSCs) and 6.2.3 (hiPSC-CMs), whereas their transfection protocols are reported in Appendix 6.3 (hiPSCs) and 6.4 (hiPSC-CMs).

Results are reported in Fig. 4.7 and in Tab. III: as shown, we found that there is a statistically significant difference between the zero-force control sensors and the sensors subject to forces for both kind of cells. Moreover, the zero-force control sensor cpA in hiPSCs presented a FRET index value which is not significantly different from the value of the same control sensor in hiPSC-CMs, as expected. The most important result we observed is, however, that a relevant difference between the FRET index values of the sensor subject to force (AcpA) between staminal and differentiated cells, is present. AcpA sensor in hiPSCs in the staminal state presented a FRET index value of $(36 \pm 2)\%$, whereas the same sensor in differentiated hiPSC-derived cardiomyocytes showed a FRET index of $(42.2 \pm 0.4)\%$.

hiPSC cells in the initial staminal state showed lower FRET index, and thus higher actin tensions, compared to cells in the differentiated state (hiPSC-CMs), indicating that an increased mechanical tension may be fundamental in hiPSCs' reprogramming

and initial differentiation. This result is in accordance with the findings of Guo et al. [72], which showed a similar trend between HEK293 and mechanically reprogrammed stem-like HEK293 cells.

| Sensor + Cell type | FRET index value (%) | Standard Error (%) |
|---|---|---|
| cpA + hiPSCs | 49 | 2 |
| AcpA + hiPSCs | 36 | 2 |
| cpA + hiPSC-CMs | 46 | 1 |
| AcpA + hiPSC-CMs | 42.2 | 0.4 |

***Table III |*** *FRET index values of actin sensors in staminal hiPSC cells and in differentiated hiPSC-derived cardiomyocytes.*

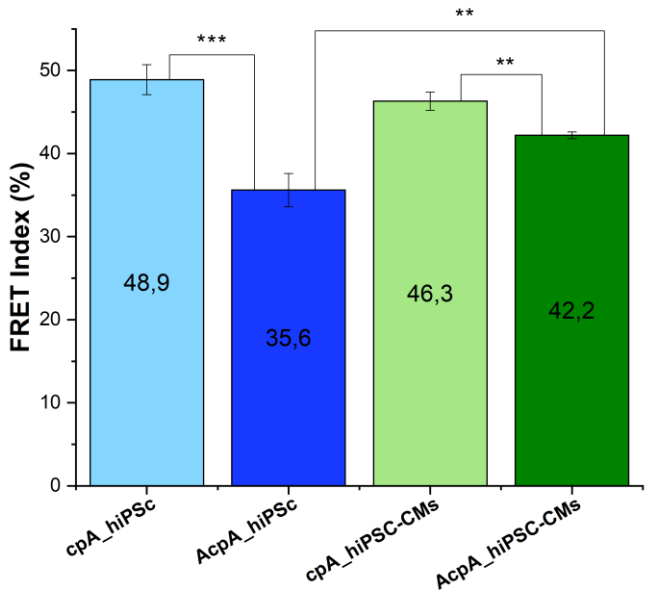


***Figure 4.7| FRET in hiPSCs and hiPSC-CMs transfected with the actin FRET sensor.*** *FRET index values for hiPSC cells in their initial stem state (blue scale) and for hiPSC-derived cardiomyocytes, which are fully differentiated (green scale). Both kind of cells were transfected with the actin FRET sensor (AcpA) and the zero-force control (cpA). The FRET index of the zero-force control sensor for hiPSCs (light blue, N = 14) did not show, as expected, a statistical relevant difference with respect to the zero-force control sensor for hiPSC-CMs (light green, N = 11), with a p-value measured through a two-sample t-test equal to* $(p = 0{,}24)$*. At the 0.05 level, there are also relevant differences between the zero-force sensor and the sensor subjected to forces in both types of cells:* $p = 2 \times 10^{-5}$ *between cpA (N = 14, light blue) and AcpA (N = 28, blue) in hiPSCs;* $p = 0{,}0049$ *between cpA (N = 11, light green) and AcpA (N = 34, green) in hiPSC-CMs. The most important result is that we found that there is also a relevant statistical difference* $(p = 0{,}004)$ *between the sensors subjected to forces of the two different kinds of cells (blue and green columns), which reflects the fact that the actin cytoskeleton is subjected to higher tension in the staminal state, suggesting that force has a fundamental role during the initial stages of cell's differentiation.*

## 4.3 The role of MLL4 protein in defining tension on nesprin in mesenchymal cells

As mentioned in Par. 1.1, mechanotransduction is fundamental for many biological and biochemical processes of cell life, development, and homeostasis. Mechano-sensors are not only acting at the interface with the plasma membrane of the cell: the LINC complex, which is located at the nuclear membrane level and consists of a chain of interacting proteins, is supposed to mechanically couple the nucleus to the cell cytoskeleton and, from there, to distant parts of the cell (Par. 1.1.2).

It is known that the genetic elements required to regulate gene expression are partitioned into active and repressive nuclear condensates: chromatin compartments include transcriptional clusters whose functioning depend on multivalent interactions occurring among transcription factors, cofactors, and transcriptional machinery. However, how chromatin contributes to the assembly of transcriptional condensates is poorly understood [87]. A study conducted by Fasciani et al. [88] demonstrated that mixed lineage leukemia 4 (MLL4) contributes to the assembly of transcriptional condensates through liquid-liquid phase separation: MLL4 loss of function impaired Polycomb-dependent chromatin compartmentalization, altering the nuclear architecture. By releasing the mechanical stress through inhibition of the mechanosensor ATR, they re-established the mechano-signalling of mesenchymal stem cells and their commitment towards chondrocytes.

Since the physical properties of chromatin shape the nucleus, which is mechanically coupled with the cytoskeleton through the LINC complex and the nuclear lamina [89], we tested our FRET sensor for nesprin, which belongs to the LINC complex, to test if there was a difference in mechanical tension sensed by nesprin in the case of wild type mesenchymal cells with MLL4 and mesenchymal cells where a haploinsufficiency of KMT2D (which encodes MLL4) is present. Fasciani et al. [88] showed that MLL4 loss of function (LoF) affects chromatin compartmentalization and results in nuclear mechanical stress and impaired mesenchymal stem cell (MSC) lineage commitment. Thus, our goal was to test if these differences in chromatin compartmentalization resulted also in a different mechanical tension transmitted from the nucleus to the nuclear membrane, and specifically to the LINC complex protein nesprin.

This part of the project was made in collaboration with the research group of Prof. Alessio Zippo of the University of Trento, which provided us of two mesenchymal cell lines: wild type-1 MSCs, with normal MLL4 function ($MLL4^{WT}$), and c6-MSCs, with MLL4 impairment ($MLL4^{Q4092X}$), resulting in MLL4 LoF. We received these cells in

frozen stocks and we cultured and prepared them according to the procedures described in Appendix 6.2.4. We optimized a transcription protocol for MSCs lines to transfect them with the nesprin sensor, which is described in detail in Par. 3.4.3. The transcription protocol of NesprinTS and NesprinHL into MSCs is described in Appendix 6.5. The experimental parameters used are specified in Appendix 6.2.4 and an example of a cell transfected with the nesprin sensor is displayed in Fig. 4.8, whereas results are shown in Fig. 4.9 and Tab. IV.

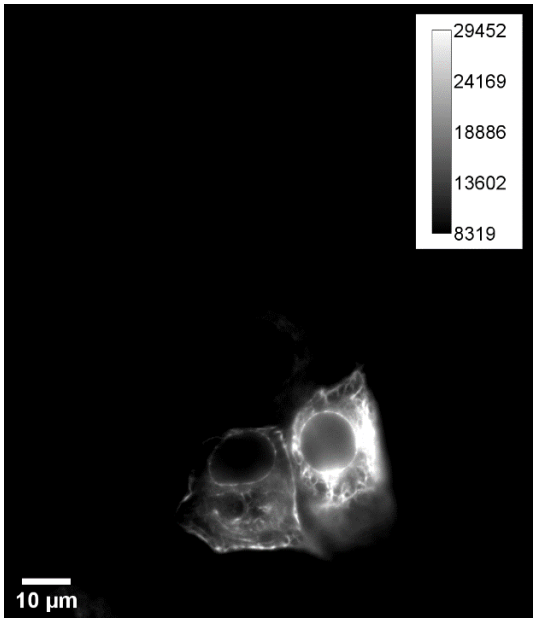


***Figure 4.8| Example of a fluorescence image of MSCs transfected with the nesprin FRET sensor.*** *This image was acquired in the acceptor channel upon excitation with the 445 nm-wavelength laser and represents a mutant mesenchymal cell (C6-MSC) transfected with the nesprin FRET sensor (NesprinTS). As you can see, the image is different with respect to the ones took with actin and alpha-actinin sensors, which are proteins of the cytoskeleton localizing in the hole cell. Here, in fact, fluorescence is concentrated at the nuclear membrane, and thus it forms a luminous ring surrounding the dark circle of the nucleus.*

| Cell type + Sensor | FRET index value (%) | Standard Error (%) |
|---|---|---|
| WT1 MSCs + NesprinHL | 24 | 2 |
| WT1 MSCs + NesprinTS | 8 | 1 |
| C6 MSCs + NesprinHL | 31 | 2 |
| C6 MSCs + NesprinTS | 20 | 1 |

***Table IV*** *| FRET index values of nesprin sensors in wild type (WT1) mesenchymal cells and in mutated (C6) mesenchymal cells*

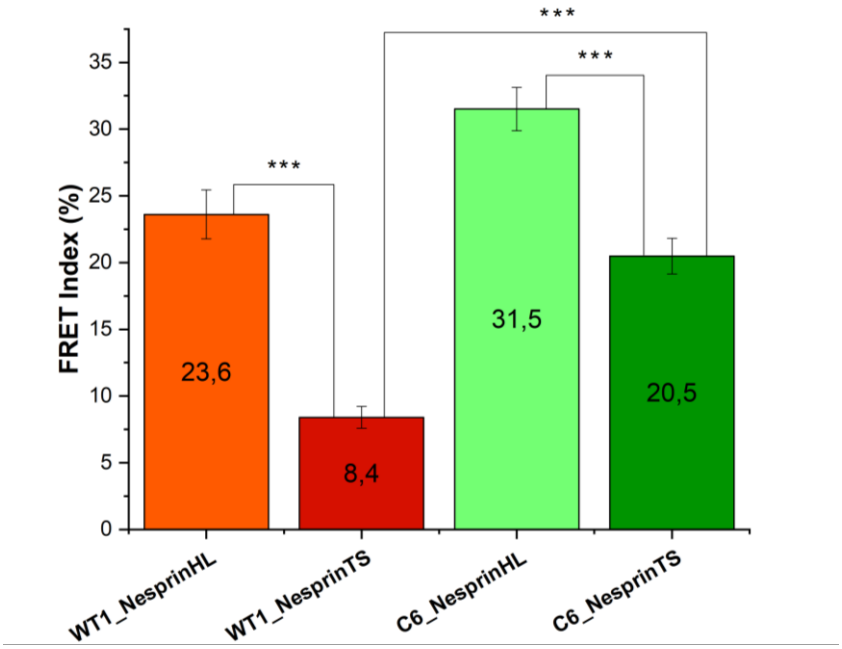


***Figure 4.9|FRET in WT1-MSCs and C6-MSCs transfected with the nesprin FRET sensor.*** *FRET index values for mesenchymal cells in their wild type form (WT1, red scale) and for mutant mesenchymal cells, which have a mutation in MLL4 that causes MLL4 LoF (C6, green scale). Both kind of cells were transfected with the nesprin FRET sensor (NesprinTS) and the zero-force control (NesprinHL). At the 0.05 level, there are relevant differences between the zero-force sensor and the sensor subjected to forces in both types of cells:* $p = 7 \times 10^{-8}$ *between NesprinHL (N = 23, orange) and NesprinTS (N = 4, red) in WT1-MSCs;* $p = 9 \times 10^{-6}$ *between NesprinHL (N = 29, light green) and NesprinTS (N = 10, dark green) in c6-MSCs. The most important result is that we found that there is also a relevant statistical difference (*$p = 5 \times 10^{-6}$*) between the sensors subjected to forces of the two different kinds of cells (red and green columns), showing that MLL4 correct functionality also results in higher transmission of mechanical tensions to the LINC complex.*

We found that there is a statistically significant difference between the zero-force control sensors and the sensors subject to force for both kinds of cells, as expected. The most relevant result we obtained is, however, that we found a significative difference in the FRET index values of the sensors subject to forces (NesprinTS), between wild type and mutant cells. NesprinTS sensor in WT1-MSCs showed a FRET index value of $(8 \pm 2)\%$, whereas the same sensor in mutant c6-MSCs presented a FRET index of $(20 \pm 1)\%$.

These results seem to be in contrast with the findings of Fasciani et al. [88]. In fact, in their work they measured through Brillouin microscopy that c6-MSCs show increased chromatin compaction and nuclear stiffness, validating the hypothesis that MLL4 LoF has an impact on nuclear architecture. In our measurements, we observe

lower tension on nesprin in c6-MSCs with respect to WT-MSCs. However, these findings are not necessarily in discordance: in fact, the two kinds of measurements are performed with different techniques and do not have the same focus. They performed an overall measurement on the entire nucleus, whereas we concentrated only on a force measurement on nesprin. Therefore, this study requires further insights to unravel the relationship between the stiffness of the nucleus, the compartmentation of chromatin, and the mechanical force which is transmitted to the LINC complex. What seems clear from both experiments, however, is that mechanical tension plays a key role in chromatin compartmentation and gene regulation.

# 5 Conclusions and future perspectives

## 5.1 Construction and characterization of a novel setup for the investigation of mechanotransduction processes

The study of mechanotransduction in living cells requires the measurement of forces in different locations of the cell with molecular specificity, as well as the simultaneous imaging of biochemical and genetic signals occurring in the biological system of interest. Several techniques are available to exert and measure force on cells, but the measurement of the mechanical properties of cells is usually disentangled from the study of what happens inside, due to the restricted accessibility of intracellular structures. The complexity of simultaneous measurement of forces and mechanically activated signals in living cells demands for the development of advanced setups combining multiple techniques.

During my Ph.D. work, I implemented an all-optical setup which combines optical tweezers, FRET-based molecular tension microscopy and fluorescence imaging with single-molecule sensitivity, with the capability to mechanically stimulate cells and simultaneously image the propagation of mechanical and biochemical signals inside the cell. In chapter 2 I showed the details of the optical setup and its potential application for mechanobiology studies, together with the procedures for the calibration and test of the different components.

As I mentioned at the end of Par. 2.1.1, we recently expanded the setup capabilities by adding polarizing beam-splitters and a tunable lens, to enable experiments in a dual-trap configuration, and to achieve 3D displacement of the traps fully disentangled from microscope imaging [77]. Moreover, we added a microscope-incubator system (Okolab H301 chamber with UNO-T-H-$CO_2$ all-in-one controller) that allows measurements on time scales comparable to cell's lifetime, by keeping the ideal environmental conditions and allowing experiments lasting for few days.

The development of this setup and the related methodologies explored in this thesis will form the basis for further studies on the transmission of mechanical forces from the external part of the cell to the cell's cytoskeleton and nucleus and on how cells respond and adapt to these mechanical stimuli, hopefully opening to new discoveries about the molecular mechanisms of mechanotransduction in living systems.

## 5.2 The stiffness of the substrate determines tension on the cell's cytoskeleton

After the implementation of the setup, I focussed on the characterization of FRET sensors for the measurements of force in cytoskeletal proteins: F-actin and alpha-actinin.

My research was focussed on understanding whether cells grown on substrates with different rigidities adapted to the different mechanical environment. In particular, a main question was whether the change in rigidity of the substrate was reflected by a change in tension on the actin cytoskeleton. It is already established that the stiffness of the substrate has an influence on cell's shape and morphology, as well as on cell's motility and growth and, importantly, in cell rigidity. This latter result, together with the observation of increased focal adhesion density and cell area with the substrate stiffness, indicate that a rearrangement of the cell cytoskeleton with substrate rigidity should occur. However, to my knowledge, a direct observation of how tension on actin and on actin-binding proteins changes with substrate rigidity was missing. The actin and alpha-actinin FRET sensors used in this work allowed us to fill this gap in knowledge.

We obtained very interesting results for both sensors (actin and alpha-actinin), which showed that there was a relevant difference between the sensors (AcpA and Actinin-M-cpstFRET) grown on different rigidity substrates. We observed that the FRET index value of the force FRET sensors decreased as the stiffness of the substrate increased, showing that a stiffer substrate reflected in higher forces on the cytoskeletal proteins. From a biophysical perspective, this result indicates that the increased cell rigidity, adhesion and flattening of the cell on the substrate when the substrate stiffness increases, derives from an increased tension exerted by myosin motors on the actin cytoskeleton, a result that was expected, but not directly observed. It will be interesting in future studies to inhibit myosin activity and see how the tension on actin change with substrate stiffness.

As future perspectives, we would like to couple these force measurements with structural studies on the cytoskeleton of cells grown on the same hydrogels, to test whether this difference in actin and alpha-actinin force transmission is linked to possible structural changes or re-arrangements of the cell's cytoskeleton. In particular, the single molecule capabilities of the setup open to the possibility of using localization-based super resolution methods such as PALM (Photo-Activated Localization Microscopy) or STORM (Stochastic Optical Resolution Microscopy) to investigate actin ultrastructure with nanometre resolution.

Moreover, we would like to perform the same measurements on FRET sensors designed for other proteins which are located at different key points in the cell mechanotransduction machinery. This will lead to a better understanding of the mechanical routes that are followed by mechanical signals from the external environment to cell's adhesion, the cytoskeleton, and down to the cell nucleus.

## 5.3 Mechanical tension plays a fundamental role in cell's differentiation and development

Mechanotransduction is also crucial for cell differentiation and development. For this reason, we have used FRET force sensors to explore how tension on the actin cytoskeleton changes during cell differentiation. In collaboration with the Experimental and Clinical Medicine Department of the University of Florence, we performed measurements on human induced Pluripotent Stem Cells (hiPSCs) at their staminal state, and then after they completely differentiated into cardiomyocytes (hiPSC-CMs). Both hiPSCs and hiPSC-CMs were transfected with the actin FRET force sensors (AcpA and cpA).

We found a statistically significant difference between the zero-force control sensors and the sensors subjected to forces for both kinds of cells, thus validating the correct functioning and transfection of the actin sensors in hiPSCs and hiPSC-CMs. Moreover, the zero-force control sensors of the two cell types did not show a significant FRET index difference.

The result which is worthy of attention is, however, the observation of a relevant difference in the FRET index values of the sensors subject to forces between staminal and differentiated cells. Our data show that the actin cytoskeleton in staminal cells is under higher force than in differentiated cells. This result suggests that an increased mechanical tension in the actin cytoskeleton of the cell may be fundamental in hiPSCs' reprogramming and stem state, and, intriguingly, that abnormal forces on actin might possibly affect the correct differentiation of the cell, and thus its development and fate.

As a future application of this study, we would like to study force in the actin cytoskeleton by using the same sensor transfected in cells derived from patients that suffer from genetic cardiomyopathies, and, in particular, from Duchenne's syndrome. Such study could help us to understand if the insurgence of the cardiomyopathy could

associate with decreased or abnormal mechanical forces in the actin cytoskeleton, at different stages of cell's differentiation. The potential implications of this study go beyond the aim, still very important, of understanding basic mechanisms: it could help to understand how changes in the mechanical response are correlated with the development of certain pathologies and could offer new insights in regenerative medicine.

## 5.4 Chromatin compartmentation tunes mechanical tension at the nucleus-cytoskeleton interface

The contribution of chromatin condensates to the transcriptional machinery has not been fully understood. It is known that a key role belongs to the MLL4-complex of proteins, which could be relevant for its activity in regulating the chromatin state and gene expression. To make a further step in the elucidation of MLL4 role, we performed experiments in collaboration with the group of Prof. Zippo of the University of Trento, and we tested a FRET-force sensor for nesprin, a protein involved in the LINC complex, in MSCs cells with wild-type and a mutant MLL4 protein associated with Kabuki syndrome, a congenital disorder of genetic origin. This mutation is associated with impaired formation of chromatin condensates, which has been linked to changes in cell shape and nuclei stiffness, measured by Brillouin microscopy [88]. We had interested in understanding if such change in chromatin organization impact on the mechanical properties of cells and, in particular, on the transmission of forces from the nucleus to the cytoskeleton.

We transfected both wild-type and mutant cells with the nesprin FRET sensors (NesprinTS and NesprinHL) and acquired FRET images to test if the force exerted on the LINC complex was affected by the ability of chromatin to create condensates.

We observed a statistically significant difference between the zero-force control sensors, which is not subject to mechanical tensions, and the sensors subject to forces for both kinds of cells.

The relevant result we want to emphasise here is, however, that a significative difference in the FRET index values of the sensors subject to forces (NesprinTS) between wild type and mutant cells was observed. NesprinTS sensor WT1-MSCs showed a lower FRET index value with respect to the FRET index value of the same sensor in mutant c6-MSCs.

This result indicates that chromatin compartmentation, which is hindered in the case of cells with mutated MLL4, has an influence on the transmission of force to the nuclear membrane, as demonstrated by the fact that a lower mechanical stress on the LINC complex is measured through the nesprin FRET-force sensor. These results also suggests that mechanical tension at the nuclear membrane might play a key role in chromatin compartmentation and gene regulation.

In the context of this study, as a future application we will directly measure the nucleus stiffness by internalizing microbeads into the cell and measure the measure the elastic response by using optical tweezers. Moreover, by using cell lines with fluorescent MLL4, we will test if application of force on the nucleus might directly impinge on chromatin compartmentation.

# 6 Appendixes

## 6.1 Creation of a PDMS chamber for experiments on hydrogels

When performing experiment on different stiffnesses hydrogels, we had to build a new imaging chamber different from the classical one we used for experiments on glass coverslips. In fact, the thickness of the hydrogel did not allow us to reach the cells of the sample with the objected working distance. Moreover, the thickness of the hydrogel drove to a strong loss of power due to light scattering in the gel. The advantage of using Easy Coat™ Softslip hydrogels from Matrigen is that they can be detached from the 12-well plates. I decided to use this fact to reverse the sample upside-down on a rectangular coverslip, in order to have the cells near to its surface and thus, reachable by the objective's working distance. I projected a new chamber, which I called Easy Inject, that allowed to do this by using a glass coverslip, a microscope slide, and a polymer called polydimethylsiloxane (PDMS). PDMS is the most widely used silicon-based organic polymer, it is optically clear, and its applications range from contact lenses and medical devices to elastomers. PDMS has a high affinity for glass and for PDMS itself. A schematic of the new chamber I implemented is illustrated in Fig. 6.1.

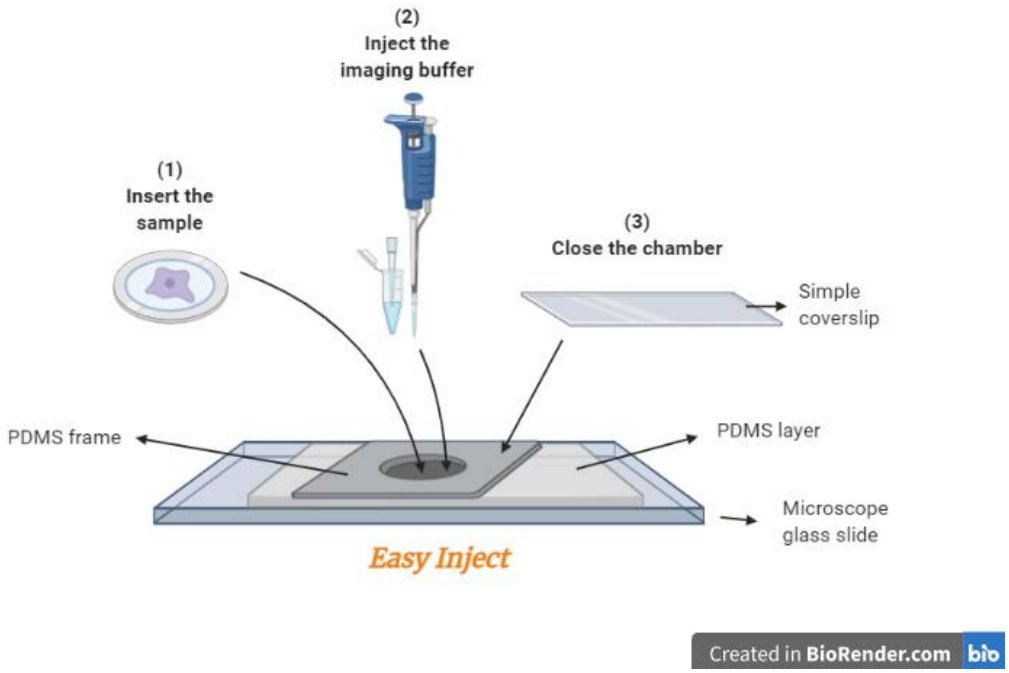


***Figure 6.1| PDMS chamber.*** *A microscope glass slide is covered with a thin PDMS layer. A PDMS frame, which can be made with different heights, is attached on the PDMS layer. The sample is then inserted in the frame and free space is filled with the imaging buffer. The chamber is closed simply by covering the frame with a glass coverslip.*

The chamber (Fig. 6.1) was made by taking a microscope glass slide and, after submitting it to a plasma surface treatment, pouring it with a thin layer of PDMS. A squared PDMS frame, large enough to contain the 18 mm- coverslip with hydrogel and with adjustable height according to the thickness of the hydrogel, is cut from a layer of PDMS and is then superimposed on the microscope glass slide covered with the PDMS layer. This construct is then heated at $\sim 60°C$ in an oven: this is done to make the binding between the PDMS layer and the PDMS frame stronger. In fact, after heating, this structure becomes permanent and the chamber itself can be used many times.

When we want to perform experiments, we can simply insert the sample, which is composed by a glass coverslip (18 mm diameter), a hydrogel layer, and cells, into the frame. It is suggested to use a drop of nail polish to stronger attach the glass coverslip to the PDMS layer. After nail polish has dried, we fill the empty space in the frame with the imaging buffer required, and we close the chamber with a rectangular glass coverslip (Fig. 6.1). In this way, we can mount this chamber on the microscope stage in an "upside-down" manner and illuminate it from below (from the cells' side), without having to go through the hydrogel thickness.

## 6.2 Preparation of samples and measurement parameters

In this paragraph the preparations of different samples and the measurement parameters used in the various experiments are shown.

### 6.2.1 HEK cell lines

In this section I describe the handling of the mammalian cell lines used in the FRET microscopy experiments performed to measure tension in F-actin and alpha-actinin. The cells used are HEK (Human Embryonic Kidney) cells that stably express the actin or alpha-actinin force sensors. We received frozen vials (-80°C) from Kerafast Inc. and we prepared them for measurements as described below.

- Under a sterile laminar flow hood, a frozen stock aliquot (approximately 1 ml) of the cell line of choice (AcpA, cpA, or Actinin-C/M-cpstFRET) is thawed by immersing it into 4 ml of the appropriate culture medium, previously warmed at 37°C.

- After the frozen stock has completely dissolved, the cell suspension is centrifuged for 3 minutes at 200 x g to separate the cells from the DMSO-containing storage medium.
- The supernatant is removed, and the cells are resuspended in 5 ml of fresh culture medium. The cell suspension is plated in a 60 mm cell culture dish and placed in a $CO_2$ incubator for growth.
- The cells are cultured and should be passaged at least twice before being used for imaging.
- The cells are plated at around 10% confluency on top of 18 mm glass coverslips placed in a 12-well culture plate for experiments on glass substrates.
- The cells are plated at around 15% confluency on top of Easy Coat™ Softslip hydrogels from Matrigen. The hydrogel is transparent, of defined stiffness, and is bound to the surface of 18 mm glass coverslips in 12 well plates (coverslips are removable). Easy Coat™ hydrogels are chemically activated to bind to the matrix protein of choice (optional: the hydrogel can be previously coated with fibronectin to improve the adhesion of cells).
- After 16-24 hours, the samples are washed in PBS before being mounted in an imaging chamber (Fig. 6.2) and immersed in 1 ml imaging buffer (Leibovitz's medium). For hydrogels samples the imaging chamber was created with PDMS, as described in Appendix 6.1.

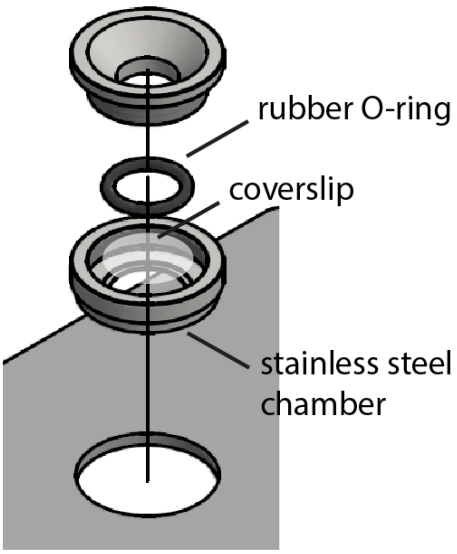


***Figure 6.2|Imaging chamber schematics.*** *Schematic illustration of the chamber used for experiments with samples of cells grown on simple glass coverslips of 18 mm. The coverslip is inserted into the stainless-steel chamber and placed on the microscope on an appropriate and compatible support.*

At this point, the biological preparation of samples is complete, and we can place the imaging chamber on the microscope to perform measurements. For FRET experiments, the acquisition procedure and the imaging parameters are described below.

- A sample with HEK cells without FRET sensors is placed on the microscope and illuminated both with the 445 nm- and the 514 nm-wavelength lasers to correct for possible autofluorescence of the cells.
- The sample of interest with HEK cells containing the actin or alpha-actinin FRET sensor is placed on the microscope, and the ideal focal plane is chosen.
- A specific field of view is chosen in brightfield: areas with single and separated cells are preferred.
- All the samples (both glass and hydrogels) were illuminated in TIRF or wide-field configuration.
- The sample was illuminated with the 445 nm- wavelength laser for 50 ms with a power on the sample plane of 2,5 mW in the case of TIRF configuration, and of 8 mW in the case of wide-field configuration.
- Image of the Donor and FRET channels are acquired with a 50 ms integration time.
- The sample is subsequently illuminated with the 514 nm-wavelength laser for 50 ms with a power on the sample plane of 2,5 mW (TIRF configuration) or 8 mW (wide-field configuration).
- Image of the Acceptor channel is acquired with a 50 ms integration time.
- Bright-field image of the area of interest is also acquired.
- The three images are saved in the same folder to be later processed through the MATLAB and ImageJ plugins previously described (Par. 3.1 and 3.2).

### *6.2.2 Human Induced Pluripotent Stem cells*

In this section I describe the handling of the human induced Pluripotent Stem Cells (hiPSCs) samples used in the FRET microscopy experiments performed to measure tension in F-actin. These samples were prepared in collaboration with the Experimental and Clinical Medicine Department of the University of Florence to investigate on the propagation of forces in the actin cytoskeleton during cardiomyocytes differentiation. hiPSCs are cells derived from adult cells and then brought back to an initial stem state through specific reprogramming protocols, which can be then differentiate again to become cardiomyocytes. Studying the transmission of forces during differentiation is of great importance since it has been

observed that dysfunctionality in this transmission can lead to the insurgence of different pathologies [90].

We optimized a protocol to transfect hiPSCs derived from adult urine with actin cpstFRET sensors (AcpA and cpA), hiPSCs were transfected and stably expressed the actin sensors both at their initial stem state and after different phases of differentiation towards cardiomyocytes (Par.6.2.3).

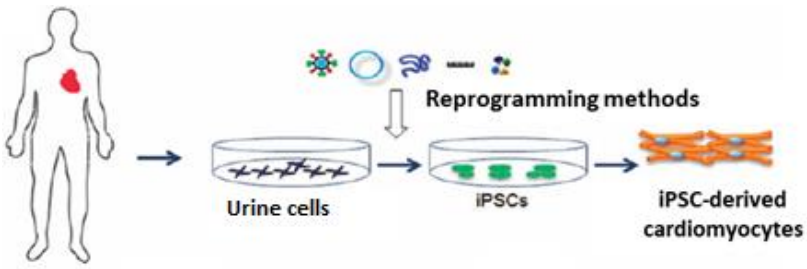


***Figure 6.3| hiPSC-derived cardiomyocytes.*** *Schematic of the mechanisms through which cardiomyocytes are derived from adult human urine. Urine-derived cells from a healthy male donor were reprogrammed into hiPSC lines through reprogramming methods and were then differentiated again towards cardiomyocytes by growing them on substrates.*

- Cells were a kind gift from the lab of Prof. Corrado Poggesi of the Experimental and Clinical Medicine Department of the University of Florence. Cells were grown on 18 mm glass coverslip coated with fibronectin at different differentiation stages.
- Cells were ready to be transfected with actin sensors through the FuGENE® HD transfecting kit. FuGENE® is the transfecting agent that can form lipidic micelles that fuse with the cytoplasmatic membrane, where they release the plasmid. The transfection protocol is described in Appendix 6.3.
- It takes 24 hours for the cells to be efficiently transfected with both AcpA and cpA sensors and thus to be ready for microscopy experiments.
- After 24 hours, the samples are washed in PBS before being mounted in an imaging chamber (Fig. 6.2) and immersed in 1 ml imaging buffer (Leibovitz's medium).

At this point, samples are ready, and the imaging chamber can be positioned on the microscope to perform measurements. For FRET experiments, the acquisition procedure and the imaging parameters are described below.

- A sample with hiPS cells without FRET sensors is placed on the microscope and illuminated both with the 445 nm- and the 514 nm-wavelength lasers to correct for possible autofluorescence of the cells.

- The sample of interest with hiPS cells containing the actin FRET sensors is placed on the microscope, and the ideal focal plane is chosen.
- A specific field of view is chosen in brightfield: areas with single and separated cells are preferred.
- All the samples were illuminated in wide-field configuration.
- The sample was illuminated with the 445 nm- wavelength laser for 50 ms with a power on the sample plane of 8 mW.
- Image of the Donor and FRET channels are acquired with a 50 ms integration time.
- The sample is subsequently illuminated with the 514 nm-wavelength laser for 50 ms with a power on the sample plane of 8 mW.
- Image of the Acceptor channel is acquired with a 50 ms integration time.
- Bright-field image of the area of interest is also acquired.
- The three images are saved in the same folder to be later processed through the MATLAB and ImageJ plugins previously described (Par. 3.1 and 3.2).

### *6.2.3 hiPSCs - derived cardiomyocytes*

As explained in Par. 6.2.2, human induced pluripotent stem cells can be differentiated to become cardiomyocytes. This process was driven by the Experimental Medicine Department as well, which furnished us with hiPSC-derived cardyomyocytes in order to perform the same FRET microscopy experiments we did on cells at their initial stem state, after a complete differentiation into cardiomyocytes. We optimized a protocol to transfect cardiomyocytes with the AcpA and cpA sensors, to investigate on how the transmission of mechanical forces may varies during differentiation of cells in the actin cytoskeleton.

- Cells were a kind gift from the Experimental and Clinical Medicine Department of the University of Florence. Cells were plated on 18 mm glass coverslip coated with fibronectin (1 mg/mL) with a seeding density of $5\times 10^4$.
- Cells which were used for measurements were given us respectively after 48, 49 and 51 days of differentiation.
- Cells were ready to be transfected with actin sensors through the FuGENE® HD transfecting kit. The transfection protocol is described in Appendix 6.4.
- It takes 24 hours for the cells to be efficiently transfected with both AcpA and cpA sensors and thus to be ready for microscopy experiments.

- After 24 hours, the samples are washed in PBS before being mounted in an imaging chamber (Fig. 6.2) and immersed in 1 ml imaging buffer (Leibovitz's medium).

At this point, samples are ready, and the imaging chamber can be positioned on the microscope to perform measurements. For FRET experiments, the acquisition procedure and the imaging parameters are described below.

- A sample with cardiomyocytes without FRET sensors is placed on the microscope and illuminated both with the 445 nm- and the 514 nm-wavelength lasers to correct for possible autofluorescence of the cells.
- The sample of interest with cardiomyocytes containing the actin FRET sensors is placed on the microscope, and the ideal focal plane is chosen.
- A specific field of view is chosen in brightfield: it is necessary to choose a field of view where a single layer of cardiac cells is present, to avoid fluorescence light coming from planes different from the chosen layer.
- All the samples were illuminated in wide-field configuration.
- The sample was illuminated with the 445 nm- wavelength laser for 50 ms with a power on the sample plane of 8 mW.
- Image of the Donor and FRET channels are acquired with a 50 ms integration time.
- The sample is subsequently illuminated with the 514 nm-wavelength laser for 50 ms with a power on the sample plane of 8 mW.
- Image of the Acceptor channel is acquired with a 50 ms integration time.
- Bright-field image of the area of interest is also acquired.
- The three images are saved in the same folder to be later processed through the MATLAB and ImageJ plugins previously described (Par. 3.1 and 3.2).

### *6.2.4 Mesenchymal cells for measurement on nesprin*

In this section I describe the handling of the mesenchymal cell lines used in the FRET microscopy experiments performed to measure tension in nesprin. The cells used were a kind gift from the lab of Prof. Alessio Zippo of the University of Trento. Cells were transfected and stably expressed the nesprin sensors (NesprinTS and NesprinHL) through the FuGENE® HD transfection kit (Appendix 6.5) in order to study the transmission of mechanical forces at the nuclear membrane level (Par. 1.1.2). We received frozen vials (-80°C) of mesenchymal cells from their laboratory and we prepared them for measurements as described below.

- Under a sterile laminar flow hood, a frozen stock aliquot (approximately 1 ml) of mesenchymal cells is thawed by immersing it into 9 ml of the appropriate culture medium, previously warmed at 37°C.
- After the frozen stock has completely dissolved, the cell suspension is centrifuged for 5 minutes at 200-250 x g to separate the cells from the DMSO-containing storage medium.
- The supernatant is removed, and the cells are resuspended in 5 ml of fresh culture medium. The cell suspension is plated in a 60 mm cell culture dish and placed in a $CO_2$ incubator for growth.
- The cells are cultured and should be passaged at least twice before being used for imaging.
- The cells are plated at around 10% confluency on top of 18 mm glass coverslips covered with poly-L-lysine placed in a 12-well culture plate.
- After 48 hours, the samples are ready for the transfection process through FuGENE® HD kit (Appendix 6.5).
- After 24 hours cells are washed in PBS before being mounted in an imaging chamber (Fig. 6.2) and immersed in 1 ml imaging buffer (Leibovitz's medium).

At this point, samples are ready, and the imaging chamber can be positioned on the microscope to perform measurements. For FRET experiments, the acquisition procedure and the imaging parameters are the same as for HEK cells (Par. 6.2.1) and the illumination is performed in TIRF microscopy configuration. As in the case of hiPSCs (Par. 6.2.2), it is very difficult to find single cells separated one from the other, as mesenchymal cells are elongated and tend to aggregate. So, it is necessary to select an area of interest where there is a monolayer of cells to avoid out-of-focus fluorescence collection coming from upper or lower layers. Images of mesenchymal cells without FRET sensors have been taken to correct FRET fluorescence for the autofluorescence emission coming from adipose agglomerates, which emit in the same emission range of the donor molecule, which could lead to false positive FRET signals. Images obtained from measurements are saved and processed through the MATLAB and ImageJ plugins described previously (Par. 3.1 and 3.2).

## 6.3 FuGENE® transfection protocol for hiPSCs

- FRET-actin plasmids have been taken from Addgene (Actin-cpstFRET-Actin was a gift from Fred Sachs, Addgene plasmid #80643, http://n2t.net/addgene:80643, RRID:Addgene_80643 ; cpstFRET-Actin was a gift from Fred Sachs, Addgene plasmid #80644, http://n2t.net/addgene:80644, RRID:Addgene_80644).
- Plasmids arrived in glycerol bacterial stabs, which were grown on a LB agar plate overnight in a 37°C heated incubator with 1X Kanamycin antibiotic.
- The following day a single bacterial colony was selected and grown overnight in 50 mL of LB medium at 37°C, 200 rpm.
- The day after plasmids have been purified using a QlAprep spin Miniprep kit (Qiagen).
- hiPS cells were plated with a seeding density of $6 \times 10^4$, transfected after 24 hours and observed the following day.
- Cells have been transfected and cultured in pluriSTEM cell medium (Sigma), with 10% FBS and 1% penicillin and streptomycin.
- Cells have been transfected with the FuGENE® HD Transfection Reagent (Promega). The transfecting agent was incubated with the actin plasmid at a final concentration of 1 µg/mL with a 2:1 ratio in a total volume of 100 µL of pluriSTEM cell medium, and after 15 minutes it was added to the wells.

## 6.4 FuGENE® transfection protocol for cardiomyocytes

- FRET-actin plasmids have been taken from Addgene (Actin-cpstFRET-Actin was a gift from Fred Sachs, Addgene plasmid #80643, http://n2t.net/addgene:80643, RRID:Addgene_80643; cpstFRET-Actin was a gift from Fred Sachs, Addgene plasmid #80644, http://n2t.net/addgene:80644, RRID:Addgene_80644).
- Plasmids arrived in glycerol bacterial stabs, which were grown on a LB agar plate overnight in a 37°C heated incubator with 1X Kanamycin antibiotic.
- The following day a single bacterial colony was selected and grown overnight in 50 mL of LB medium at 37°C, 200 rpm.
- The day after plasmids have been purified using a QlAprep spin Miniprep kit (Qiagen).
- Cardiomyocytes were plated with a seeding density of $5 \times 10^4$, transfected after 24 hours and observed the following day.

- Cells have been transfected and cultured in PSC cardiomyocytes maintenance medium (Thermofisher), with 10% FBS and 1% penicillin and streptomycin.
- Cells have been transfected with the FuGENE® HD Transfection Reagent (Promega). The transfecting agent was incubated with the actin plasmid at a final concentration of 1 µg/mL with a 2:1 ratio in a total volume of 100 µL of pluriSTEM cell medium, and after 15 minutes it was added to the wells.

## 6.5 FuGENE® transfection protocol for MSCs

- FRET-nesprin sensors have been taken from Addgene (pcdna nesprinTS was a gift from Daniel Conway, Addgene plasmid #68127, http://n2t.net/addgene:68127, RRID:Addgene_68127; pcdna nesprinHL was a gift from Daniel Conway, Addgene plasmid #68128, http://n2t.net/addgene:68128, RRID:Addgene_68128).
- Plasmids arrived in glycerol bacterial stabs, which were grown on a LB agar plate overnight in a 37°C heated incubator with 1X ampicillin antibiotic.
- The following day a single bacterial colony was selected and grown overnight in 50 mL of LB medium at 37°C, 200 rpm.
- The day after plasmids have been purified using a QlAprep spin Miniprep kit (Qiagen).
- MSCs have been plated on fibronectin-treated coverslips (1 mg/mL) with a seeding density of $1 \times 10^5$, transfected after 24 hours and observed the following day.
- Cells have been transfected and cultured in DMEM medium, high glucose (Thermofisher #11965092) with 10% FBS and 1% penicillin and streptomycin.
- Cells have been transfected with the FuGENE® HD Transfection Reagent (Promega). The transfecting agent was incubated with the nesprin plasmid at a final concentration of 1 µg/mL with a 2:1 ratio in a total volume of 100 µL of pluriSTEM cell medium, and after 15 minutes it was added to the wells.

# 7 References

[1] N. Wang, J. D. Tytell, and D. E. Ingber, “Focus on Mechanotransduction Perspectives,” *Nat. Rev. Mol. Cell Biol.*, vol. 10, no. January, pp. 75–82, 2009.

[2] K. C. Neuman and A. Nagy, “Single-molecule force spectroscopy: optical tweezers, magnetic tweezers and atomic force microscopy,” *Nat Methods*, vol. 5, no. 6, pp. 491–505, 2008.

[3] C. Jurchenko and K. S. Salaita, “Lighting Up the Force: Investigating Mechanisms of Mechanotransduction Using Fluorescent Tension Probes,” *Mol. Cell. Biol.*, vol. 35, no. 15, pp. 2570–2582, 2015.

[4] C. Gayrard and N. Borghi, “FRET-based Molecular Tension Microscopy,” *Methods*, vol. 94, pp. 33–42, 2016.

[5] M. Sergides, L. Perego, T. Galgani, C. Arbore, F. S. Pavone, and M. Capitanio, “Probing mechanotransduction in living cells by optical tweezers and FRET-based molecular force microscopy,” *Eur. Phys. J. Plus*, vol. 136, no. 3, 2021.

[6] B. D. Hoffman, C. Grashoff, and M. A. Schwartz, “Dynamic molecular processes mediate cellular mechanotransduction,” *Nature*, vol. 475, no. 7356, pp. 316–323, 2011.

[7] G. R. Fedorchak, A. Kaminski, and J. Lammerding, “Cellular mechanosensing: Getting to the nucleus of it all,” *Prog. Biophys. Mol. Biol.*, vol. 115, no. 2–3, pp. 76–92, 2014.

[8] C. Wu, “Focal adhesion: a focal point in current cell biology and molecular medicine.,” *Cell Adh. Migr.*, vol. 1, no. 1, pp. 13–18, 2007.

[9] M. A. Wozniak, K. Modzelewska, L. Kwong, and P. J. Keely, “Focal adhesion regulation of cell behavior,” *Biochim. Biophys. Acta - Mol. Cell Res.*, vol. 1692, no. 2–3, pp. 103–119, 2004.

[10] R. O. Hynes, “Integrins: Versatility, modulation, and signaling in cell adhesion,” *Cell*. 1992.

[11] I. Monteiro A., T. Kollmetz, and J. Malmström, “Engineered systems to study the synergistic signaling between integrin-mediated mechanotransduction and growth factors (Review),” *Biointerphases*, vol. 13, no. 6, p. 06D302, 2018.

[12] F. Cailliez and R. Lavery, “Cadherin mechanics and complexation: The importance of calcium binding,” *Biophys. J.*, vol. 89, no. 6, pp. 3895–3903, 2005.

[13] B. Ladoux, W. J. Nelson, J. Yan, and R. M. Mège, “The mechanotransduction machinery at work at adherens junctions,” *Integr. Biol. (United Kingdom)*, vol. 7, no. 10, pp. 1109–1119, 2015.

[14] H. Aberle *et al.*, “Cadherin-catenin complex: Protein interactions and their implications for cadherin function,” *Nat. Rev. Mol. Cell Biol.*, vol. 11, no. 4, pp. 502–514, 1996.

[15] S. Dufour, R. M. Mège, and J. P. Thiery, “α-catenin, vinculin, and F-actin in strengthening E-cadherin cell-cell adhesions and mechanosensing,” *Cell Adhes. Migr.*, vol. 7, no. 4, pp. 345–350, 2013.

[16] J. Iwasa and W. Marshall, “Karp’s Cell and Molecular Biology: Concepts and Experiments,” *MRCOG Part One*, 2016.

[17] M. Hieda, “Signal Transduction across the Nuclear Envelope: Role of the LINC Complex in Bidirectional Signaling,” *Cells*, vol. 8, no. 2, p. 124, 2019.

[18] A. J. Maniotis, C. S. Chen, and D. E. Ingber, “Demonstration of mechanical connections between integrins, cytoskeletal filaments, and nucleoplasm that stabilize nuclear structure,” *Proc. Natl. Acad. Sci. U. S. A.*, vol. 94, no. 3, pp. 849–854, 1997.

[19] M. J. Stroud, “Linker of nucleoskeleton and cytoskeleton complex proteins in cardiomyopathy,” *Biophys. Rev.*, vol. 10, no. 4, pp. 1033–1051, 2018.

[20] W. Chang, H. J. Worman, and G. G. Gundersen, “Accessorizing and anchoring the LINC complex for multifunctionality,” *J. Cell Biol.*, vol. 208, no. 1, pp. 11–22, 2015.

[21] P. T. Arsenovic *et al.*, “Nesprin-2G, a Component of the Nuclear LINC Complex, Is Subject to Myosin-Dependent Tension,” *Biophys. J.*, vol. 110, no. 1, pp. 34–43, 2016.

[22] W. Chang, S. Antoku, C. Östlund, H. J. Worman, and G. G. Gundersen, “Linker of nucleoskeleton and cytoskeleton (Linc) complex-mediated actin-dependent nuclear positioning orients centrosomes in migrating myoblasts,” *Nucleus*, vol. 6, no. 1, pp. 77–88, 2015.

[23] R. Koszul, K. P. Kim, M. Prentiss, N. Kleckner, and S. Kameoka, “Meiotic Chromosomes Move by Linkage to Dynamic Actin Cables with Transduction of Force through the Nuclear Envelope,” *Cell*, vol. 133, no. 7, pp. 1188–1201, 2008.

[24] D. T. Warren *et al.*, “Nesprin-2-dependent ERK1/2 compartmentalisation regulates the DNA damage response in vascular smooth muscle cell ageing,” *Cell Death Differ.*, vol. 22, no. 9, pp. 1540–1550, 2015.

[25] K. Lei *et al.*, “Inner nuclear envelope proteins SUN1 and SUN2 play a prominent role in the DNA damage response,” *Curr. Biol.*, vol. 22, no. 17, pp. 1609–1615, 2012.

[26] R. N. Rashmi *et al.*, “The nuclear envelope protein Nesprin-2 has rolesin cell

proliferation and differentiation during wound healingce . Do not distribute . © 2012 Landes Bioscience . Do not distribute .," *Nucleus*, vol. 3, no. 2, pp. 172–186, 2012.

[27] T. Bouzid *et al.*, "The LINC complex, mechanotransduction, and mesenchymal stem cell function and fate," *J. Biol. Eng.*, vol. 13, no. 1, pp. 1–12, 2019.

[28] A. R. Harris, P. Jreij, and D. A. Fletcher, "Mechanotransduction by the Actin Cytoskeleton: Converting Mechanical Stimuli into Biochemical Signals," *Annu. Rev. Biophys.*, vol. 47, pp. 617–631, 2018.

[29] L. Blanchoin, R. Boujemaa-Paterski, C. Sykes, and J. Plastino, "Actin dynamics, architecture, and mechanics in cell motility," *Physiol. Rev.*, vol. 94, no. 1, pp. 235–263, 2014.

[30] T. Fujii, A. H. Iwane, T. Yanagida, and K. Namba, "Direct visualization of secondary structures of F-actin by electron cryomicroscopy," *Nature*, vol. 467, no. 7316, pp. 724–728, 2010.

[31] K. Hayakawa, H. Tatsumi, and M. Sokabe, "Actin filaments function as a tension sensor by tension-dependent binding of cofilin to the filament," *J. Cell Biol.*, vol. 195, no. 5, pp. 721–727, 2011.

[32] T. Q. P. Uyeda, Y. Iwadate, N. Umeki, A. Nagasaki, and S. Yumura, "Stretching actin filaments within cells enhances their affinity for the myosin ii motor domain," *PLoS One*, vol. 6, no. 10, 2011.

[33] A. Del Rio, R. Perez-Jimenez, R. Liu, P. Roca-Cusachs, J. M. Fernandez, and M. P. Sheetz, "Stretching single talin rod molecules activates vinculin binding," *Science (80-. ).*, vol. 323, no. 5914, pp. 638–641, 2009.

[34] C. Arbore, L. Perego, M. Sergides, and M. Capitanio, "Probing force in living cells with optical tweezers: from single-molecule mechanics to cell mechanotransduction," *Biophys. Rev.*, vol. 11, no. 5, pp. 765–782, 2019.

[35] H. Zhang *et al.*, "Optical tweezers for single cells.," *J. R. Soc. Interface*, vol. 5, no. 24, pp. 671–90, Jul. 2008.

[36] E. L. Botvinick and Y. Wang, "Laser Tweezers in the Study of Mechanobiology in Live Cells," 2007, pp. 497–523.

[37] G. T. Charras and M. A. Horton, "Single cell mechanotransduction and its modulation analyzed by atomic force microscope indentation," *Biophys. J.*, vol. 82, no. 6, pp. 2970–2981, 2002.

[38] S. Na and N. Wang, "Application of fluorescence resonance energy transfer and magnetic twisting cytometry to quantify mechanochemical signaling activities in a

living cell," *Sci. Signal.*, vol. 1, no. 34, pp. 1–10, 2008.

[39] A. Ashkin, K. Schütze, J. M. Dziedzic, U. Euteneuer, and M. Schliwa, "Force generation of organelle transport measured in vivo by an infrared laser trap," *Nature*, vol. 348, no. 6299, pp. 346–348, Nov. 1990.

[40] A. Ashkin and J. M. Dziedzic, "Internal cell manipulation using infrared laser traps.," *Proc. Natl. Acad. Sci. U. S. A.*, vol. 86, no. 20, pp. 7914–8, Oct. 1989.

[41] M. Capitanio, "Optical tweezers," in *An Introduction to Single Molecule Biophysics*, 2017.

[42] K. C. Neuman and S. M. Block, "Optical trapping," *Rev. Sci. Instrum.*, vol. 75, no. 9, pp. 2787–2809, 2004.

[43] Y. Harada and T. Asakura, "Radiation forces on a dielectric sphere in the Rayleigh scattering regime," *Opt. Commun.*, vol. 124, no. 5–6, pp. 529–541, 1996.

[44] A. Ashkin, J. M. Dziedzic, J. E. Bjorkholm, and S. Chu, "Observation of a single-beam gradient force optical trap for dielectric particles," *Opt. Lett.*, vol. 11, no. 5, p. 288, 1986.

[45] M. Capitanio *et al.*, "Calibration of optical tweezers with differential interference contrast signals," *Rev. Sci. Instrum.*, vol. 73, no. 4, p. 1687, 2002.

[46] G. K. Batchelor, "An Introduction to Fluid Dynamics," *Book*. p. 631, 1967.

[47] J. Howard, "Mechanics of motor proteins and the cytoskeleton," *Phys. Today*, vol. 55, no. 3, p. 63, 2002.

[48] M. Fischer and K. Berg-Sorensen, "Calibration of trapping force and response function of optical tweezers in viscoelastic media," *J. Opt. a-Pure Appl. Opt.*, vol. 9, no. 8, pp. S239–S250, 2007.

[49] Y. Jun, S. K. Tripathy, B. R. J. Narayanareddy, M. K. Mattson-Hoss, and S. P. Gross, "Calibration of optical tweezers for in vivo force measurements: how do different approaches compare?," *Biophys. J.*, vol. 107, no. 6, pp. 1474–84, Sep. 2014.

[50] M. Capitanio, R. Cicchi, and F. S. Pavone, "Position control and optical manipulation for nanotechnology applications," *Eur. Phys. J. B*, vol. 46, no. 1, pp. 1–8, 2005.

[51] L. P. Ghislain, N. A. Switz, and W. W. Webb, "Measurement of small forces using an optical trap," *Rev. Sci. Instrum.*, vol. 65, no. 9, pp. 2762–2768, 1994.

[52] D. E. Discher, "Tissue Cells Feel and Respon to the Stiffness of Their Substrate," *Science (80-. ).*, vol. 310, no. 5751, pp. 1139–1143, 2005.

[53] C. F. Guimarães, L. Gasperini, A. P. Marques, and R. L. Reis, “The stiffness of living tissues and its implications for tissue engineering,” *Nat. Rev. Mater.*, vol. 5, no. 5, pp. 351–370, 2020.

[54] J. W. Lichtman and J. A. Conchello, “Fluorescence microscopy,” *Nat. Methods*, vol. 2, no. 12, pp. 910–919, 2005.

[55] T. Latychevskaia, “Lateral and axial resolution criteria in incoherent and coherent optics and holography, near- and far-field regimes,” *Appl. Opt.*, vol. 58, no. 13, p. 3597, 2019.

[56] E. W. M. Born, “Principles of Optics.” Pergamon Press, 1993.

[57] A. Miyawaki, A. Sawano, and T. Kogure, “Lighting up cells: labelling proteins with fluorophores.,” *Nat. Cell Biol.*, vol. Suppl, no. 1, pp. S1-7, 2003.

[58] O. SHIMOMURA, F. H. JOHNSON, and Y. SAIGA, “Extraction, purification and properties of aequorin, a bioluminescent,” *J. Cell. Comp. Physiol.*, vol. 59, no. 165, pp. 223–239, 1962.

[59] A. A. Abdul-Jalil, S. N. Khalaf, and S. S. Dawod, “Modification of the green fluorescent protein properties using the site direct mutagenesis effects by replacing Y66W,” *Biochem. Cell. Arch.*, vol. 18, no. 2, pp. 1671–1678, 2018.

[60] M. Ulrich, “Konfokale laserscanmikroskopie,” *Hautarzt*, vol. 66, no. 7, pp. 504–510, 2015.

[61] T. Ng, “Imaging Protein Kinase C Activation in Cells,” *Science (80-. ).*, vol. 283, no. 5410, pp. 2085–2089, 1999.

[62] P. J. Verveer, F. S. Wouters, and A. R. Reynolds, “Signal Propagation in the Plasma Membrane Quantitative Imaging of Lateral ErbB1 Receptor Signal Propagation in the Plasma Membrane,” *Society*, vol. 1567, no. 2000, pp. 1–5, 2009.

[63] J. K. Jaiswal, H. Mattoussi, J. M. Mauro, and S. M. Simon, “Long-term multiple color imaging of live cells using quantum dot bioconjugates,” *Nat. Biotechnol.*, vol. 21, no. 1, pp. 47–51, 2003.

[64] D. Chhabra and C. G. dos Remedios, “Fluorescence Resonance Energy Transfer,” *Encycl. Life Sci.*, pp. 1–9, 2005.

[65] S. V. Koushik, H. Chen, C. Thaler, H. L. Puhl, and S. S. Vogel, “Cerulean, venus, and venusY67C FRET reference standards,” *Biophys. J.*, vol. 91, no. 12, pp. L99–L101, 2006.

[66] F. Meng, T. M. Suchyna, and F. Sachs, “A fluorescence energy transfer-based mechanical stress sensor for specific proteins in situ,” *FEBS J.*, vol. 275, no. 12, pp.

3072–3087, 2008.

[67] F. Meng and F. Sachs, “Visualizing dynamic cytoplasmic forces with a compliance-matched FRET sensor,” *J. Cell Sci.*, vol. 124, no. 2, pp. 261–269, 2011.

[68] C. Grashoff *et al.*, “Measuring mechanical tension across vinculin reveals regulation of focal adhesion dynamics,” *Nature*, vol. 466, no. 7303, pp. 263–266, 2010.

[69] Y. Wang, F. Meng, F. Sachs, Y. Wang, F. Meng, and F. Sachs, “Genetically encoded force sensors for measuring mechanical forces in proteins Genetically encoded force sensors for measuring mechanical forces in proteins,” vol. 0889, 2011.

[70] C. Grashoff *et al.*, “Measuring mechanical tension across vinculin reveals regulation of focal adhesion dynamics,” *Nature*, vol. 466, no. 7303, pp. 263–266, 2010.

[71] K. Austen *et al.*, “Extracellular rigidity sensing by talin isoform-specific mechanical linkages,” *Nat. Cell Biol.*, vol. 17, no. 12, pp. 1597–1606, 2015.

[72] J. Guo, Y. Wang, F. Sachs, and F. Meng, “Actin stress in cell reprogramming,” *Proc. Natl. Acad. Sci.*, vol. 111, no. 49, pp. E5252–E5261, 2014.

[73] F. Meng and F. Sachs, “Orientation-based FRET sensor for real-time imaging of cellular forces,” *J. Cell Sci.*, vol. 125, no. 3, pp. 743–750, 2012.

[74] D. E. Conway, M. T. Breckenridge, E. Hinde, E. Gratton, C. S. Chen, and M. A. Schwartz, “Fluid shear stress on endothelial cells modulates mechanical tension across VE-cadherin and PECAM-1,” *Curr. Biol.*, vol. 23, no. 11, pp. 1024–1030, 2013.

[75] K. C. Neuman, E. H. Chadd, G. F. Liou, K. Bergman, and S. M. Block, “Characterization of photodamage to Escherichia coli in optical traps,” *Biophys. J.*, vol. 77, no. 5, pp. 2856–2863, 1999.

[76] F. Gittes and C. F. Schmidt, “Interference model for back-focal-plane displacement detection in optical tweezers,” *Opt. Lett.*, vol. 23, pp. 7–9, 1998.

[77] F. Falleroni, V. Torre, and D. Cojoc, “Cell Mechanotransduction With Piconewton Forces Applied by Optical Tweezers,” *Front. Cell. Neurosci.*, vol. 12, p. 130, May 2018.

[78] R. E. Thompson, D. R. Larson, and W. W. Webb, “Precise nanometer localization analysis for individual fluorescent probes,” *Biophys. J.*, vol. 82, no. 5, pp. 2775–2783, 2002.

[79] K. N. Fish, “Total internal reflection fluorescence (TIRF) microscopy,” *Current*

*Protocols in Cytometry*. 2009.

[80] J. N. Feige, D. Sage, W. Wahli, B. Desvergne, and L. Gelman, "PixFRET, an ImageJ plug-in for FRET calculation that can accommodate variations in spectral bleed-throughs," *Microsc. Res. Tech.*, vol. 68, no. 1, pp. 51–58, 2005.

[81] B. R. Acharya *et al.*, "Mammalian Diaphanous 1 Mediates a Pathway for E-cadherin to Stabilize Epithelial Barriers through Junctional Contractility," *Cell Rep.*, vol. 18, no. 12, pp. 2854–2867, 2017.

[82] K. Austen *et al.*, "Extracellular rigidity sensing by talin isoform-specific mechanical linkages," *Nat. Cell Biol.*, vol. 17, no. 12, pp. 1597–1606, 2015.

[83] K. H. Vining and D. J. Mooney, "Mechanical forces direct stem cell regeneration," *Nat. Publ. Gr.*, 2017.

[84] X. Yang, L. Pabon, and C. E. Murry, "Engineering adolescence: Maturation of human pluripotent stem cell-derived cardiomyocytes," *Circ. Res.*, vol. 114, no. 3, pp. 511–523, 2014.

[85] X. Guan *et al.*, "Dystrophin-deficient cardiomyocytes derived from human urine: New biologic reagents for drug discovery," *Stem Cell Res.*, vol. 12, no. 2, pp. 467–480, 2014.

[86] J. M. Pioner *et al.*, "Isolation and mechanical measurements of myofibrils from human induced pluripotent stem cell-derived cardiomyocytes," *Stem Cell Reports*, vol. 6, no. 6, pp. 885–896, 2016.

[87] B. van Steensel and E. E. M. Furlong, "The role of transcription in shaping the spatial organization of the genome," *Nat. Rev. Mol. Cell Biol.*, vol. 20, no. 6, pp. 327–337, 2019.

[88] A. Fasciani *et al.*, "MLL4-associated condensates counterbalance Polycomb-mediated nuclear mechanical stress in Kabuki syndrome," *Nat. Genet.*, vol. 52, no. 12, pp. 1397–1411, 2020.

[89] C. Uhler and G. V. Shivashankar, "Regulation of genome organization and gene expression by nuclear mechanotransduction," *Nat. Rev. Mol. Cell Biol.*, vol. 18, no. 12, pp. 717–727, 2017.

[90] J. M. Pioner *et al.*, "Absence of full-length dystrophin impairs normal maturation and contraction of cardiomyocytes derived from human-induced pluripotent stem cells," *Cardiovasc. Res.*, vol. 116, no. 2, pp. 368–382, 2020.

# 8 Acknowledgements

I would like to express my gratitude to Prof. Marco Capitanio for giving me the opportunity to belong to the Single Molecule Biophysics group, a research group which has been a challenging environment that allowed me to constantly grow as a scientist and as a person. I also want to say how grateful I am for his patience when I was taking my first steps into the lab and when I was writing this thesis.

I want to say thanks to the whole Single Molecule family, including old and new members, which accompanied and supported me through these 3 years. Marios and Lucia, which gave me the biggest support and technical help; Martino, which never made me have lunch alone; Tiziano, Claudia and Claudia, which introduced me to biology; Giulio, my music and experiment mate; Chiara, my chocolate-deliver when I used to be upset; and Anatolii, my computer-problem solver.

I also want to thank the entire, old and new, “Pollaio” office: even though I sometimes hated you for being loud and rowdy, I also loved you and you will always be a part of this wonderful experience.

I will never be grateful enough to my parents Marco and Nicoletta. I think I still cannot understand at all how much they sacrificed just to see me getting to this finish line. This achievement is dedicated to you.

A big thank to my messy siblings: Lorenzo, Lavinia, Luca and Lucia. I know I’ve been unbearable sometimes, but you have always been happier than me for my results. I also want to thank Elena, Giorgio and Andrea for constantly bringing joy in my life.
More generally, I want to thank all the people of the extended family.

I want to say thank you also to all of my friends, around Italy and the world. Each of you brought me to get here, in so many different but fundamental ways.

A big thank also to all the “water polo world”, first of all to my team, which was patient and comprehensive when I was late for practices, and which has been quite a second family to me. Then, to all of my athletes of the “Imperfect Team”, you taught me to overcome limits, without saying a single word.

I would like to be able to say thanks to my grandpa Momi, which taught me to never surrender and always inspired me to do more. I guess that even this achievement is not enough for you ;)

Luca, Fabri, Bizzo, I’d like to have you here, but I’m sure you are glad for me, and you will always look upon on me. Thank you all.

Yours,

Laura